INVESTIGATING HEPATIC MICROVASCULAR DYNAMICS THROUGH FUNCTIONAL ULTRASOUND IMAGING

Tesi di Laurea di:

Giulia Realini, 854386

Marco Rivolta, 858437

"Everyone wants to live on top of the mountain,
but all the happiness and growth occurs while you're climbing it."

Contents

List of Figures

List of Tables

Summary

Introduction

The primary role of microcirculation is the carriage of nutrients and oxygen and the removal of metabolic waste products from the tissue. The microvascular bed, composed by an arteriole, a venule and capillaries, constitutes the functional unit. In particular, capillaries are mainly responsible for exchange of substances. They are characterized by a diameter ranging between 50 and 80 nm.

Comprehending mechanisms which regulate microcirculation is gaining an increasing importance because the well-being of tissues depends on the circulatory transport process, which is explained by many microhaemodynamic functional parameters, such as blood flow, blood volume, intravascular and extravascular pressures as well as capillary permeability. Indeed, microvasculature is the site of control of tissue perfusion, blood-tissue exchanges and tissue blood volume [1].

The amount of nutrients delivered to a specific tissue depends primarily on blood flow and specific metabolic demand. This system is finely regulated through very complex mechanisms which encompass both general control performed by central nervous system (acting on vascular tone) and local control, performed primarily by capillary endothelial cells.

The pivotal role of microcirculation in several disease is well established ([2], [3], [4]). With the constant improvement of diagnostic tools, scientists and physicians realized that many problems affecting patients may arise from microcirculatory disfunctions.

Novel techniques have made possible a direct observation of microvascular haemodynamics at the patient bedside ([5], [6]). Nowadays, research using these new techniques is focusing on the central role of the microcirculation in critical diseases. In studies conducted on humans, microcirculation has most extensively been investigated in generalized inflammation and sepsis ([4], [7]).

The current study concerns mainly the hepatic microcirculation and, in a minor part, the

intestinal one.

Liver microcirculation guarantees supply of the parecnhyma with oxygen and nutrients, representing the gate for leukocytes entrance during hepatic inflammation and it is responsible for clearance of toxicants and foreign bodies from blood stream [8]. Literature studies ([4],[9]) show that microcirculatory dysfunctions are highly correlated with the occurrence of different disease states. Thus, the study of hepatic microcirculation could be valuable not only for a deeper knowledge of diseases, but also for the development of better therapeutic procedures.

State of the Art

Imaging techniques generally used to investigate microvasculature are Near-Infrared spectroscopy (NIRS) [10], Orthogonal Polarization Spectroscopy (OPS) ([11], [12]) and Sidestream Dark Field Imaging (SDF) ([13],[14]). Even if good image quality and microcirculation visualization are achieved, especially with SDF imaging, these methods present some drawbacks which make them unsuitable for *in vivo* analysis of microvascular bed. They have a low penetration depth which allows analysis only on epidermis and upperdermis and their field of view (FOV) is small (around 1 mm). For these reasons, the current techniques do not allow measurement of aforementioned microcirculatory parameters, except for particular easy-to-reach regions, such as the sublingual area. Studies on the microvascular bed of other sites of the human body (e.g., the liver) can not be successfully perfomed.

Therefore, a new imaging technique based on ultrasounds is being developed at Esposti Lab. at the San Raffaele Research Institute of Milan, with the aim of obtaining an imaging system suitable for clinical environment: functional ultrasound imaging (fUS).

The main characteristic of fUS system is its high frame rate, which results in a better sensitivity to very slow fluxes, making possible to analyze the microhemodynamics of various organs *in vivo* [15]. Frame rate has been increased by using a method called "Compound imaging" [16]. Instead of using focused wave as conventional Doppler methods do, compound imaging system generates plane wave through which object is scanned at different angles: all the obtained images are then coherently summed to form the final image. The use of plane waves lead to a dramatic decrease in the acquisition time, which is reflected in a frame rate increase. Consequently, given a fixed acquisition time, the number of images collected with fUS is much higher than the one with conventional Doppler method, resulting in a better SNR and sensitivity of images [15].

Therefore, fUS could represents a precious diagnostic tool, because of its characteristics:

- spatial resolution under 100 μm;

- penetration depth up to 20 cm;

- Field of view higher than 1 cm^2;

- sensitivity to blood speed of the order of 10 mm/s.

These improvements make fUS the principal candidate for future clinical applications of microvasculature diagnostic and monitoring.

Aim of this thesis work is to generate the first set of signal processing techniques and procedures to extract relevant information from functional ultrasound recordings.

Materials

fUS recordings analysed in the current work have been acquired by a team of researchers of the Esposti Lab. Acquistions has been performed *in vivo*. The ultrasound probe used has the following characteristics: sampling frequency of 1.25 Hz, emitted ultrasound waves frequency of 11 MHz; the spatial resolution of the images is 80 μm, detectable blood velocity is 7 mm/s (bottom limit) and the FOV is around 1 cm^2

A dataset consists of a sequence of images from liver or jejunum from living rat. Organs have been observed either in physiologic state or in altered condition, for example during the administration of drugs such Dobutamine (DB) and Nitroglycerine (NG).

Datasets are characterized by different temporal duration: the acquisition time ranges from 4 to 15 minutes, determining the number of frames (i.e., of images) of each sequence.

All the sequences are transcutaneous, positioning the probe over the organ surface. Intestinal sequences are divided into two main categories depending on the anatomical section considered: transversal or longitudinal.

Results

In this thesis, results are organized in the following way: first part regards the implementation of a procedure to clean images from noise, while the second part encompasses a set of signal processing techniques which have been used to analyse fUS recordings with the aim of extracting useful biological information.

Pre-Processing Procedure Implementation   This part of the study describes the development of a signal processing procedure in order to successively analyse the information content of the recordings.

Acquired raw data are contaminated by noise, superimposed on all the images of the sequence. Noise is generated mainly by organ movements and it is well visible in each pixel time series as fast oscillations which endure throughout the entire sequence. Part of these artefacts consists in external interventions, such moment in which injection occurs that causes a sudden movement of the whole organ, or movements due to human interactions: these types of interferences can be easily attenuated, while artefacts due to intrinsic organ motion are more problematic when dealing with living organs. Another critical factor to be considered is the following: in addition to physiological organ movements, organs could shrink, swell or generally warp. If structures of interest inside the field of view change significantly, any form of temporal analysis becomes worthless, because of the non correspondence between pixel and anatomical point along frames. These aspects reduce strongly the usability of available datasets, underlining how important and mandatory it is an accurate signal pre-processing. Datasets suitable for further analyses have been obtained taking advantage of several processing methods, regarding both noise removal and structures of interest visualization enhancement.

For a correct and optimal visualization of vessels, the following procedure should be considered:

1. application of Kalman Filter to remove high frequency noise. In addition, if this filter is not sufficient, moving average filter can be applied too;

2. registration process: this step is required for the sequences on which temporal analysis is performed. The registration includes calculation of a set of transformation matrices (one matrix for each frame) and the application of them to the dataset;

3. contrast enhancement operations: contrast in the image is increased thanks to the application of an implemented homomorphic filter and then with the automatic histogram adjustment. Together, these operations cancel unwanted effects due to variable brightness values on image plane, compress image dynamics and increase contrast, allowing a good visualization also of the smallest vessels.

Processing   After the application of the right pre-processing procedure on images, the second part of the project is focused on extrapolating relevant biological information.

In order to provide an informative tool to physicians, one of the main goals of fUS imaging is to allow clinical evaluations through some standard parameters which can be extracted from image sequences. Such parameters could strongly help in decision-making process, leading to better and more effective patient care.

The parameters considered herein are perfusion map and vessels diameter automatised extraction. The first parameter generates a map in which it is possible to detect whether areas of interest (e.g., a precise zone of parenchyma) dynamically modify their perfusion profiles. The second parameter instead provides a measurement of diameters of all the vessels within the image along time.

Particular attention has been paid on the analysis of images gathered during the administration of the aforementioned vasoactive drugs: Dobutamine and Nitroglycerine.

To investigate their effect on hepatic microvascular dynamics, *Variation Images* have been computed. These images are generated from original dataset as relative variation with respect to a baseline (i.e., frames before the injection). In this way, consequences of drug administration on vessels dynamics are more visible because each pixel videointensity represents the percentage change with respect to baseline: even if a pixel has a low videointesity in the original dataset, the new images set do not depend on such gray-level.

After an accurate analysis on both cases, the most credited hypothesis is that DB mainly causes extravasation, while NG is responsible for vasodilation.

Information extracted through this technology can be useful as a new tool for both basic and translational research. Gathered data can help to better comprehend complex mechanisms which regulate microcirculation. In particular, clustering has been applied as method to identify sub-areas of the studied organ behaving according to similar temporal patterns. The purpose of this analysis is to define the correspondence between points of the image and specific anatomical structures (e.g., hepatic artery, portal vein, hepatic vein, parenchyma).

Clustering has been achieved using k-means algorithm on original datasets and on relative variation images, which, as previously said, are of particular interest for recordings gathered during vasoactive drug administration.

Clustering has allowed the grouping of pixels based both on the magnitude and the shape of

each signal (when using original time series) and just on the temporal shape (if normalized signals are used), allowing a first blind clustering of basic anatomical structures. Further analysis will be required to deep further the found correspondences.

Also intestine recordings have been studied, even if with a shorter effort dedicated to them. Analysis on these recordings underlines that the microhemodynamics of the villi (i.e., microvascular branches of intestine) is characterized by oscillations along time which are slightly variable depending on the organ area. Frequency analysis has been performed in physiological state and during intraluminal perfusion with a nutrient glucose, to investigate the value of the main frequency of these areas and if it is constant in time. Results show that nutrient administration leads to modifications in the amplitude, but not in the frequency of haemodynamic oscillations, pointing at a dynamic modulation of microvascular resistance during nutrient absorption in the gut.

Conclusions

In this work we introduced a starter set of image and signal processing tools and procedures for the analysis of fUS liver images. This represents a challenging issue because analysed organs are deformable objects which can pulsate periodically or change their shape. Indeed, fUS technique is highly sensitive to movements, then a correct noise removal (or at least noise attenuation) is required and this will constitute the basis for future optimization of a tool for the real time analysis of functional ultrasound recordings, to be used at the patient's bedside by almost-naive users.

Because of the groundbreaking nature of the images gathered by functional ultrasonography, fUS could be a key element both in clinical and research applications. Physicians could benefit from it, having at their disposal a tool which provides information on microvascular parameters to better comprehend organ state, allowing proper and timely interventions (both in monitoring and during surgical interventions). Furthermore, fUS allows to deepen knowledge of organs microcirculation and this could open to new horizons in medicine.

Clustering represents a preliminary method of analysis, especially in observing how organs react to specific drugs, with the aim of suggesting which drug is the most appropriate in each different clinical situation. For example, Dobutamine and Nitroglycerin effects have been studied on liver microvascular dynamics: DB seems to cause extravasation, while NG causes vessels dilatation.

fUS is a ductile technique and it is suitable for several other organs imaging (e.g., intestine, kidney, brain, genitals). In the current work, shorter time was dedicated to the optimization of intestinal functional ultrasound and this will most probably constitute the next step in this effort to make the best of this new and promising biomedical imaging technique.

Sommario

Introduzione

Il ruolo primario della microcircolazione è il trasporto di ossigeno e nutrienti e la rimozione di prodotti metabolici di scarto dal tessuto. Il letto microvascolare, composto da arteriola, venula e capillari, ne costituisce l'unità funzionale. In particolare, i capillari sono i responsabili principali dello scambio di sostanze. Sono caratterizzati da un diametro compreso tra 50 e 80 nm.

La comprensione dei meccanismi che regolano la microcircolazione sta diventando sempre più importante perchè il funzionamento dei tessuti dipende dal processo di trasporto circolatorio che è governato principalmente da diversi parametri funzionali microemodinamici, come il flusso e il volume sanguigno, la pressione intravascolare ed extravascolare, la permeabilità dei capillari. Infatti, la microvascolatura è il sito di controllo della perfusione tissutale, dello scambio di sangue tra tessuti e del volume sanguigno del tessuto [1].

La quantità di nutrienti forniti ad un determinato tessuto dipende principalmente dal flusso sanguigno e dalla domanda metabolica. Questo sistema è finemente regolato da meccanismi molto complessi che comprendono sia il controllo eseguito dal sistema nervoso centrale (che agisce sul tono vascolare) sia il controllo locale, eseguito principalmente da cellule endoteliali capillari.

Il ruolo fondamentale della microcircolazione in diverse patologie è ben noto ([2], [3], [4]). Con il costante miglioramento degli strumenti diagnostici, ricercatori e medici si sono resi conto che molti problemi clinici possono sorgere da disturbi microcircolatori.

Diverse tecniche innovative hanno reso possibile l'osservazione dell'emodinamica microvascolare direttamente dal lettino del paziente ([5], [6]). Oggi la ricerca che utilizza queste nuove tecniche si concentra sul ruolo centrale della microcircolazione nelle patologie più gravi. In studi condotti su umani, la microcircolazione è stata studiata maggiormente per casi di infiammazione generalizzata e sepsi ([4], [7]).

Il seguente studio riguarda principalmente la microcircolazione epatica e, in minor parte, quella intestinale.

La microcircolazione del fegato garantisce l'approvvigionamento al parenchima di ossigeno e nutrienti, rappresenta il cancello di ingresso ai leucociti durante l'infiammazione epatica ed è responsabile della pulizia del flusso sanguigno da sostanze tossiche e corpi estranei [8]. La letteratura ([4],[9]) mostra che le disfunzioni microcircolatorie sono altamente correlate con la comparsa di diverse malattie. Quindi, lo studio della microcircolazione epatica potrebbe essere prezioso non solo per una conoscenza più approfondita delle malattie, ma anche per lo sviluppo di migliori procedure terapeutiche.

Stato dell'Arte

Le tecniche di imaging generalmente impiegate per investigare la microvascolatura sono Near-Infrared spectroscopy (NIRS) [10], Orthogonal Polarization Spectroscopy (OPS) ([11], [12]) e Sidestream Dark Field Imaging (SDF) ([13],[14]). Nonostante si ottenga una buona qualità dell'immagine e la visualizzazione della microcircolazione, soprattutto con l'imaging SDF, questi metodi hanno diversi svantaggi che li rendono non adatti per un'analisi *in vivo* del letto microvascolare. Infatti hanno una profondità di penetrazione troppo bassa che permette solo analisi di derma superficiale ed epidermide e il loro campo visivo (FOV) è piccolo (circa 1 mm). Per questi motivi, le attuali tecniche di imaging non consentono una misurazione dei parametri microcircolatori sopra citati, fatta eccezione per particolari regioni facili da raggiungere, come l'area sublinguale. Studi sulla microvascolatura di altri siti del corpo umano (e.g., il fegato) non possono però essere eseguiti con successo.

Pertanto, una nuova tecnica di imaging basata sugli ultrasuoni è sotto sviluppo all'Esposti Lab. all'Istituto di Ricerca San Raffaele di Milano, con lo scopo di ottenere un sistema di imaging adatto all'ambiente clinico: functional ultrasound imaging (fUS).

La caratteristica principale del sistema fUS è il suo alto frame rate, che si riflette in una sensisitivà migliore per i flussi sanguigni molto lenti, rendendo possibile l'analisi della microemodinamica di vari organi *in vivo* [15]. Il frame rate è stato incrementato grazie all'utilizzo di un metodo chiamato "Compound imaging" [16]. Invece che usare onde focalizzate come i metodi Doppler convenzionali fanno, la tecnica Compound imaging genera onde piane emesse a diversi angoli attraverso le quali l'oggetto è scansionato: tutte le immagini ottenute sono poi sommate coerentemente per formare l'immagine finale. L'uso di onde piane porta a un marcato decremento nel tempo di acquisizione, che si riflette così in un più alto frame rate.

Di conseguenza, dato un tempo di acquisizione fissato, il numero di immagini acquisite con il metodo fUS è molto più alto di quello ottenuto con i metodi Doppler convenzionali, con il risultato finale di un miglior SNR e di una migliore sensitività [15].

Di conseguenza, il metodo fUS potrebbe rappresentare un prezioso strumento diagnostico, grazie alle sue caratteristiche:

- risoluzione spaziale minore di 100 μm;

- profondità di penetrazione fino a 20 cm;

- campo visivo superiore a 1 cm^2;

- sensitività a velocità sanguigne dell'ordine di 10 mm/s.

Questi miglioramenti rendono il metodo fUS il principale candidato per future applicazioni cliniche relative alla diagnostica e al monitoraggio della microvascolatura.

Lo scopo di questa tesi è la generazione di un primo set di tecniche e procedure di elaborazione di immagini e segnali atte all'estrazione di informazioni rilevanti da immagini di ultrasonografia funzionale.

Materiali

I dati fUS analizzati nel lavoro corrente sono stati acquisiti da un team di ricercatori dell'Esposti Lab. Le acquisizioni sono state fatte *in vivo*. La sonda ultrasonica usata ha le seguenti caratteristiche: frequenza di sampling di 1.25 Hz, frequenza degli ultrasuoni emessi pari a 11 MHz; la risoluzione spaziale delle immagini è di 80 μm, la minima velocità rilevabile è 7 mm/s e il campo visivo è circa 1 cm^2.

Un dataset è formato da una sequenza di immagini ottenute da fegato o intestino di ratti vivi. Gli organi sono osservati sia in stato fisiologico sia in condizioni alterate, per esempio durante la somministrazione di farmaci quali Dobutamina (DB) e Nitroglicerina (NG).

I dataset sono caratterizzati da diverse durate temporali: il tempo di acquisizione varia da 4 a 15 minuti, determinando così il numero di frame (i.e., di immagini) di ogni sequenza.

Tutte le sequenze sono acquisite transcutaneamente, posizionando la sonda sulla superficie dell'organo. Le sequenze relative all'intestino sono divise in due tipologie, a seconda della sezione anatomica considerata: trasversale o longitudinale.

Risultati

In questa tesi, i risultati sono organizzati nel seguente modo: la prima parte riguarda

l'implementazione di una procedura per la pulizia delle immagini dal rumore, mentre la seconda parte comprende una serie di tecniche di elaborazione di segnali che sono state utilizzate per analizzare le registrazioni fUS allo scopo di estrarre informazioni biologiche utili.

Procedura di Pre-Processing Implementata Questa prima parte del lavoro svolto riguarda lo sviluppo di una procedura di elaborazione di segnali al fine di potere poi analizzare il contenuto informativo delle registrazioni.

I dati grezzi acquisiti sono contaminati da rumore, sovrapposto a tutte le immagini della sequenza. Il rumore è generato principalmente da movimenti dell'organo ed è ben visibile in tutte le serie temporali dei pixel come rapide oscillazioni presenti lungo tutto la sequenza temporale. Parte di questi artefatti è dovuta sia a interventi esterni, come l'iniezione del farmaco che causa una reazione (i.e., un movimento) dell'organo, sia a movimenti dovuti all'interazione umana: questi tipi di interferenza possono essere attenuati facilmente, mentre gli artefatti dovuti al movimento intrinseco dell'organo sono più problematici, soprattutto quando si studiano organi vivi. Un'altro fattore critico da considerare è il seguente: oltre ai movimenti fisiologici dell'organo, quest'ultimo potrebbe restringersi, gonfiarsi, o in generale deformarsi. Se le strutture di interesse contenute nel campo visivo cambiano significatamente, qualsiasi tipo di analisi temporale diventa inutile, dal momento che viene a mancare la corrispondenza tra un pixel e il preciso punto anatomico lungo tutta la sequenza. Questi aspetti riducono fortemente l'usabilità dei datasets, sottolineando quanto sia importante e necessaria un'accurata pre-elaborazione dei segnali.

I dataset idonei ad analisi successive sono stati ottenuti sfruttando diversi metodi di elaborazione, relativi sia alla rimozione del rumore sia al miglioramente della visualizzazione delle strutture di interesse.

Per una visualizzazione corretta e ottimale dei vasi, si consiglia di seguire la seguente procedura:

1. applicazione del filtro Kalman per rimuovere il rumore ad alta frequenza. Inoltre, se questo non è sufficiente, può essere applicato anche il filtro a media mobile;

2. processo di registrazione: questa fase è necessaria per le sequenze su cui viene poi eseguita l'analisi temporale. La registrazione include il calcolo di un set di matrici di trasformazione (una matrice per ogni frame) e la loro applicazione al dataset;

3. operazioni di miglioramento del contrasto: il contrasto nell'immagine è aumentato

grazie all'applicazione di un filtro omomorfo appositamente implementato e poi con l'aggiustamento automatico dell'istogramma. Insieme, queste due operazioni annullano effetti indesiderati dovuti a valori variabili di luminosità sul piano dell'immagine, comprimono la dinamica dell'immagine e aumentano il contrasto, consentendo così una buona visualizzazione anche dei vasi più piccoli.

Processing   Dopo un'adeguata procedura di pre-processing delle immagini, la seconda parte del progetto è incentrata sull'estrapolazione di informazioni biologiche rilevanti.

Uno degli obiettivi principali dell'imaging fUS è quello di permettere una valutazione clinica attraverso parametri standard che possono essere estratti dalle sequenze di immagini, con lo scopo di fornire un utile strumento ai medici. Tali parametri potrebbero essere di grande aiuto nel processo di decision-making, generando di conseguenza una migliore e più efficace cura per il paziente.

I parametri qùi considerati sono le mappe di perfusione e l'estrazione automatica del diametro dei vasi. Il primo parametro genera una mappa all'interno della quale è possibile distinguere quali aree di interesse (e.g., una zona precisa del parenchima) modificano a livello dinamico il loro profilo di perfusione. Il secondo invece fornisce una misura del diametro di tutti i vasi contenuti nell'immagine.

Particolare attenzione è stata posta all'analisi delle immagini acquisite durante la somministrazione dei sopracitati farmaci: Dobutamina e Nitroglicerina.

Per indagare quale sia la loro azione sulla dinamica microvascolare epatica, sono state calcolate le *Variation Images*. Queste immagini sono calcolate a partire dal dataset originale come variazione relativa rispetto ad una baseline (i.e., i frame prima dell'iniezione del farmaco). In questo modo, le conseguenze della somministrazione del farmaco sulla dinamica dei vasi sono maggiormente visibili perchè ogni valore di videointensità del pixel rappresenta la variazione percentuale rispetto alla baseline: anche se un pixel ha una videointensità bassa nel dataset originale, il nuovo set di immagini non dipende da tale livello di grigio.

Dopo un'accurata analisi su entrambi i casi, l'ipotesi più accreditata è che la DB causi principalmente extravasazione, mentre la NG sia responsabile della vasodilatazione.

Le informazioni estratte con questa metodologia possono essere utili come nuovo strumento per la ricerca, sia di base che più sofisticata. Infatti i dati raccolti possono aiutare a capire

meglio i complessi meccanismi che regolano la microcircolazione. In particolare, è stato applicato il clustering in quanto metodo adatto ad identificare nell'organo studiato delle sotto-aree caratterizzate da comportamento simile (i.e., con andamento temporale simile). Lo scopo di questa analisi è la definizione di una corrispondenza tra punti dell'immagine e specifiche strutture anatomiche (e.g., l'arteria epatica, la vena porta, la vena epatica, il parenchima). Tra i vari tipi di clustering, si è scelto di applicare l'algoritmo delle k-medie sui dataset originali e sulle immagini di variazione che, come detto precedentemente, sono di particolare interesse per i set di immagini acquisiti durante somministrazione di farmaco vaso-attivante. Il clustering ha permesso il raggruppamento di pixel sia in base alla loro ampiezza e forma del segnale (quando applicato alle serie temporali originali), sia in base solamente al loro andamento temporale (quando invece sono stati analizzate le serie temporali normalizzate): in entrambi i modi si è ottenuto un primo clustering non supervisionato delle principali strutture anatomiche. Sono però necessarie delle analisi ulteriori al fine di approfondire le corrispondenze trovate.

In parte, anche i dataset relativi a immagini di intestino sono stati studiati. Prime analisi su queste registrazioni hanno evidenziato che la microemodinamica dei villi intestinali (i.e., segmenti microvascolari dell'intestino) è caratterizzata da oscillazioni lungo il tempo, leggermente variabili a seconda della zona dell'organo. È stata fatta un'analisi in frequenza sia in condizioni fisiologiche sia durante perfusione intraluminale con glucosio, con l'obiettivo di scoprire la frequenza portante di queste aree e se questa è costante nel tempo. I risultati mostrano che la somministrazione del nutriente (i.e., glucosio) va a modificare l'ampiezza, ma non la frequenza delle oscillazioni emodinamiche, evidenziando una modulazione dinamica della resistenza microvascolare durante l'assorbimento del nutriente nell'intestino.

Conclusioni

In questo lavoro è stato introdotto un primo set di tecniche e procedure di elaborazione di immagini e segnali per l'analisi di immagini fUS epatiche. Questa fase rappresenta una sfida impegnativa perchè gli organi analizzati sono oggetti deformabili che possono pulsare periodicamente o cambiare forma. Infatti, la tecnica fUS è altamente sensibile ai movimenti, quindi una corretta rimozione del rumore (o almeno una sua attenuazione) è necessaria; questo strumento costituisce la base per una futura ottimizzazione di un tool per analisi real-time di registrazioni di ultrasonografia funzionale, da usare direttamente dal lettino del

paziente da utenti non esperti nel campo dell'elaborazione di immagini.

Date le potenzialità delle immagini raccolte dall'ultrasonografia funzionale, questa tecnica potrebbe rappresentare un elemento chiave sia in applicazioni cliniche che di ricerca. I medici potrebbero disporre di uno strumento che fornisce parametri utili a comprendere lo stato di salute dell'organo, procedendo quindi a interventi più appropriati e tempestivi (sia in fase di monitoraggio che durante interventi chirurgici). Inoltre, la fUS consente di approfondire la conoscenza del funzionamento microcircolatorio di diversi organi, aprendo a nuovi orizzonti nel campo della medicina.

Il clustering rappresenta un metodo preliminare di analisi, utile in particolar modo a valutare come i diversi organi rispondano in seguito alla somministrazione di diversi farmaci. Lo scopo di questi studi è capire, considerando differenti situazioni cliniche, quale sia il farmaco più adatto per ogni caso. Per esempio, gli effetti della Dobutamina e della Nitroglicerina sono stati studiati sulla dinamica microvascolare del fegato: la Dobutamina sembra essere causa di extravasazione, mentre la Nitroglicerina causerebbe vasodilatazione.

L'utilità della fUS non è limitata solamente al fegato. Grazie alla sua duttilità, essa rappresenta uno strumento adatto all'imaging di organi come l'intestino, il cervello, i reni, gli organi genitali e altri ancora. All'ottimizzazione delle ultrasonografie funzionali intestinali è stato dedicato minor tempo; perciò, questo costituisce probabilmente il prossimo step per trarre il meglio da questa nuova e promettente tecnica di imaging biomedico.

Chapter 1

Introduction

1.1 Principles of Ultrasounds

Ultrasounds (US) are mechanical sound wave characterized by frequencies higher than 20 KHz, above the frequency range of human hearing ([17], [18])

Since they are sound waves, a medium is required for their propagation, in order to transmit mechanical energy to the particles of the medium they are passing through; consequently, they cannot propagate in vacuum.

The velocity of propagation c of the wave in each specific medium can be expressed with more than one equation, highlighting its dependence on various factors.

Firstly, material properties are crucial for propagation of the ultrasounds:

$$c = \sqrt{\frac{K}{\rho}} \tag{1.1}$$

where ρ is the medium density and K its stiffness coefficient. The more rigid the tissue, the higher is K and therefore the velocity of the wave within that tissue. Furthermore, the velocity can be expressed as a function of ultrasound wavelength λ and frequency f:

$$c = \lambda f \tag{1.2}$$

Given a fixed frequency, the propagation speed determines the wavelength. Therefore, a change in speed of the wave leaving one tissue and entering another one, with different physical properties, causes a change in wavelength proportional to the frequency.

In biological tissues, velocity of ultrasound waves is considered constant, equal to 1540 m/s [19], except for bones which are characterized by an higher velocity (around 4000 m/s). A

list of main tissues of human body and the related speed of ultrasound is shown in Table 1.1:

Tissue	Speed [m/s]	Acoustic Impedance ($\times 10^5$) [g/cm^{-2}s^{-1}]
Blood	1550	1.61
Bone	3500	7.8
Brain	1540	1.58
Liver	1570	1.65
Kidney	1560	1.62
Muscle	1580	1.7

Table 1.1: Speed of propagation of ultrasound waves in several tissues of human body and relative tissue density (table taken from [17]).

In the field of biomedical imaging, ultrasounds are mainly used in gynecology, in cardiology and in many other studies of human organs, in order to perform non-invasive anatomical investigations and to detect blood flow and its velocity. The large number of applications of medical ultrasounds is directly related to the advantages of this imaging technique, which include:

- high temporal resolution: characterized by a frame rate around 30 Hz, with US is possible to analyze fast movements of an organ, e.g. of the heart;

- no ionizing radiations involved: differently from other imaging techniques, such as X-rays or PET, US do not generate ionizing radiation within the tissue of interest, therefore there is no risk of biological damages for the patient;

- good spatial resolution, especially at high frequencies: to an increase in the US frequency corresponds an improvement of the axial resolution;

- no need of special rooms to perform the exam on patient.

1.1.1   Ultrasounds Production

US are generated by piezoelectric effect. This effect can be seen in several crystals and it consists in production of pressure waves due to particle motions in the crystal when a voltage difference is applied across it.

At the same time, if a force which causes deformation is applied to the crystal, it generates voltage difference due to specific charge distribution (Figure 1.1).
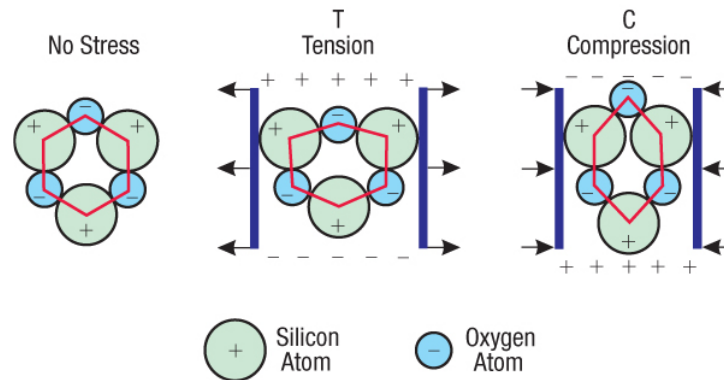
Figure 1.1: Piezoelectric effect in quartz (silicon dioxide): when there is no force acting on the crystal, the voltage difference between the two surfaces is null. When a force is applied - compression, expansion or shear stress - a deformation happens and the charge distribution inside the crystal generates potential difference.

1.1.2   Ultrasounds Propagation

During the travel of a wave in a medium, physical phenomena as refraction, reflection and absorption are likely to happen.

At the boundary surface between two different tissues, part of the energy carried by the wave is reflected and the other part is transmitted in the following medium.

Snell's law is used to describe this event:

$$\frac{c_1}{c_2} = \frac{\sin \theta_i}{\sin \theta_t} \tag{1.3}$$

where c_1 and c_2 are the speeds of the incident wave in the two medium, while θ_i and θ_t are the incident and the transmitted wave angles. A schematic view is given in Figure 1.2.

This event is noticeable anytime the wavefront passes from a tissue to another with a different value of acoustic characteristic impedance Z, defined as the product between the
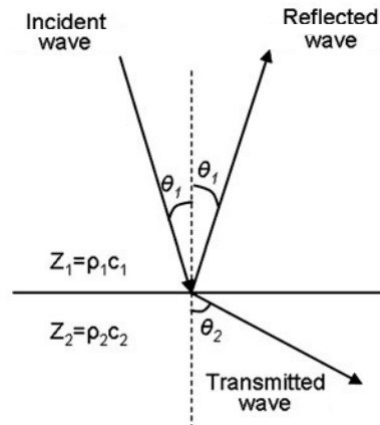
Figure 1.2: Snell's law: reflection and refraction wave due to the change in the characteristic impedance.

density of the medium and the velocity of the ultrasound wave:

$$Z = \rho c \tag{1.4}$$

This parameter is strongly dependent on the material properties: by substituting in the last formula the expression (1.1), a new formula for the characteristic impedance is obtained:

$$Z = \sqrt{\rho K} \tag{1.5}$$

which points out even more the dependence of Z on the medium of interest.

As the wavefront propagates, its intensity I decreases exponentially with the distance d:

$$I(d) = I_0 \exp(-\alpha d) \tag{1.6}$$

where α is the attenuation coefficient of the medium, usually expressed in $dB \times cm^{-1}$. Its value depends on the frequency of the ultrasound wave - an increase in frequency leads to an increse in the attenuation - and on the type of tissue.

1.2   Medical Ultrasounds

1.2.1   Instrumentation

The piezoelectric transducer is the principal component of the ultrasonic probe: transducers are used both as source and receiver of US.

The single-crystal transducer is mainly made of piezoelectric material, to which the electrodes of the alternating voltage are attached, a matching layer and a backing layer - all these elements are contained inside an acoustic insulator.

The role of these two layers are the following:

- Matching layer: due to the large difference between the acoustic characteristic impedance of the transducer substrate and the human body, a layer with a specified characteristic impedance is chosen and put after the transducer, in order to obtain 100% of transmission;

- Backing layer: it is an acoustic attenuating layer, positioned on the back face of the transducer. It serves as mechanical support for the crystal and it attenuates the energy transmitted back to it derived from undesired spurious signals generated inside the transducer housing.
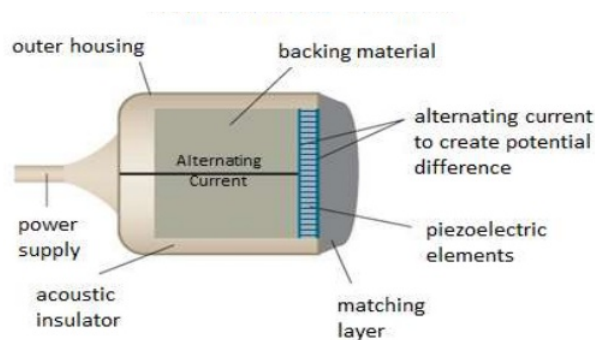
Figure 1.3: Schematic view of a single-crystal transducer.

Nowadays the single-crystal transducer is no more used for ultrasonic imaging, because of the many disadvantages linked to it, such as the need for manual or mechanical steering of the beam in order to produce the image.

A better solution is to use an array of transducers: there are several options - not discussed

here in details -, for instance linear phased arrays or linear sequential arrays.

In addition to the piezoelectric element, typical ultrasound imaging system is composed by the electronic switching circuit and detection electronics, computer processing and display system. The detection electronics includes circuits for time-gain compensation and beam forming.

1.2.2 Imaging Modes with Ultrasounds

1.2.2.1 A-Mode

A-Mode simply records signals backscattered from tissue boundaries and plots their amplitudes with respect to time (Figure 1.4).

It is the oldest ultrasonic technique and it also allows to compute the distance d of the tissue interfaces using the following relationship:

$$t = \frac{2d}{c} \tag{1.7}$$

where t is the time of signal receiving and c the speed of the wave in the medium.
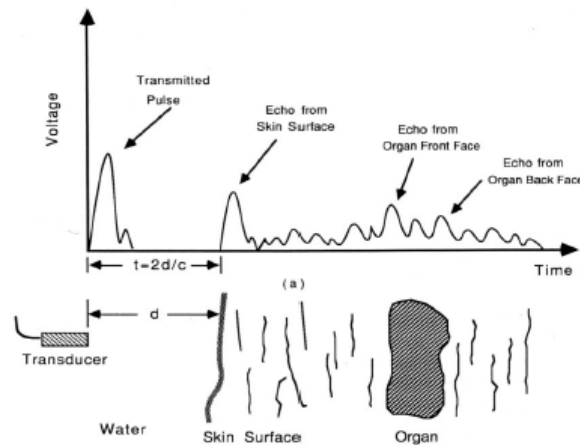
Figure 1.4: Example of time - amplitude plot obtained by scanning a body region with US in A-mode: different amplitudes are registered depending on the distance the wave have traveled inside the body.

1.2.2.2 M-Mode

M-Mode provides information about organ motion. The transducer is fixed in a certain position and the echoes coming from the analysed tissue are recorded: in this way variations

in signal amplitude represent tissue motion. M-mode can be seen as a series of A-mode lines, used for example to study heart valves movement.

1.2.2.3 B-Mode

B-Mode produces a two dimensional image - typically a cross section of the tissue - where the echo amplitude is color coded in the final image: the higher the amplitude of the signal, the brighter the value of the grayscale associated to the corresponding pixel.
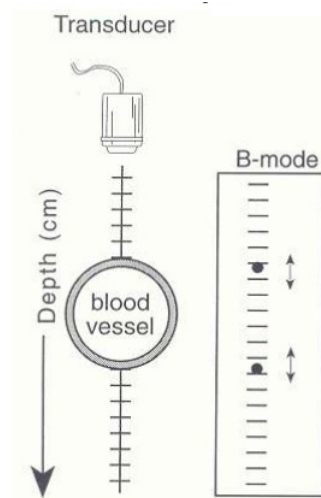
Figure 1.5: B-mode US imaging: each pixel in the image is represented by a value of brightness which is directly proportional to the strength of the echo. The tissue is scanned with lines, the final image is made of the sum of all the scan lines (in the current figure it is shown a single line, a dot corresponds to a returning echo).

1.2.3 Doppler Ultrasound Imaging

Ultrasound imaging also allows to study blood flow inside vessels by taking advantage of Doppler effect, physical phenomenon which consists in a shift of frequency (from its original value) perceived by an observer who is moving with respect to the sound source - and vice versa. (Figure 1.6).

In the specific case of ultrasound medical imaging, source and detector of US consist of the same object, while the moving object is represented by the blood within the vessels. Therefore, the signal received shows an ultrasound frequency shift which can be expressed
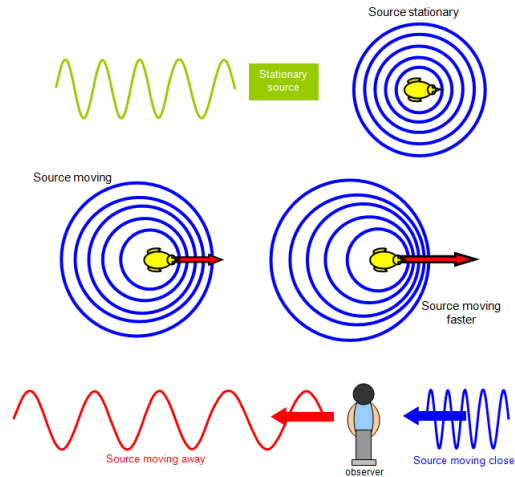
Figure 1.6: Doppler effect: the frequency of the detected sound wave shifts to an higher value when the wave is moving toward the stationary observer, while it decreases if the wave is moving away from the observer.

by the following formula (steps to obtain it are avoided):

$$\Delta f = 2 f_0 \left(\frac{v}{c}\right) \cos\theta \tag{1.8}$$

where f_0 is the frequency of the emitted US wave, v is the red blood cells (RBCs) velocity, c the ultrasound velocity in the tissue and θ is the angle between the detector and the direction of the flowing blood - knowledge of this last parameter is essential to calculate the right velocity of the blood.

There are two main configurations of the US Doppler systems: the Continuous Wave (CW) Doppler uses a transducer as emitter of US and another transducer as receiver of US, while the Pulse Wave (PW) Doppler uses the same transducer element both for transmitting and receiving the acoustic energy.

To define accurately the velocity of RBCs in the anatomical structures, the Color Doppler is used: it is made of a B-mode image of the region of interest on which the velocity information is added in a color coded way, calculated as the mean frequency shift of each line of the B-mode image.

The last imaging technique which is now described is the Power Doppler Imaging. This type of imaging is obtained by summing up all the frequency shifts of the B-mode lines, instead of doing the mean of them: Power Doppler can be seen as the integral of the values of the frequency shifts along a B-line. The main advantage of this method is the better visualization of small vessels inside tissues which correspond to very low blood flow: the final signal is the

sum of all the Doppler shifts and therefore also the smallest vessels, which have a signal (i.e. the mean of the frequency shifts) too low in the Color Doppler, can be detected.

Power Doppler imaging has a huge importance for the aim of the current project, which is the study and analysis of microcirculation signals.

1.3 Microcirculation

The primary function of the cardiovascular system is to maintain a suitable environment for tissues. Human body is characterized by a wide variety of different tissues and each one of them has different metabolic and functional needs: hence a diverse microcirculation structure and regulatory mechanisms cope with different necessities. Capillaries are the elements of circulatory system responsible for exchange of gases, water, nutrients and waste products. Microcirculation encompasses blood vessels from arterioles to venules (Figure 1.7). Both arterioles and venules have vascular smooth-muscle cells (VSMCs), while pre-capillary sphincters control the access of blood to particular segments of the network.
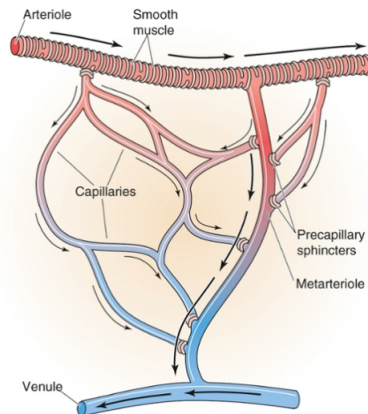
Figure 1.7: Microcirculatory unit (figure taken from [8]).

Arterioles are characterized by an inner radius ranging from 5 to 25 μm [8] and they are similar to arteries, but with only a single continuous layer of innervated VSMCs.

Capillaries have an inner radius included between 2 to 5 μm.

They are composed by a single layer of endothelial cells surrounded by a basement membrane and a fine network of reticular collagen fibers. Some endothelial cells are characterized by gaps with variable size, called fenestrations, which link the capillary lumen to the interstitial space. Their diameter varies between 50 and 80 nm [8]. Indeed, the scope of fenestrations is to allow fluxes of fluid and solutes across capillary walls.

Capillaries are categorized basing on their degree of leakiness (Figure 1.8):

1. Continuous capillaries are the most common form: they present inter-endothelial junctions from 10 to 115 nm wide. Skeletal muscle capillaries are an example;

2. Fenestrated capillaries distinguish themselves by endothelial cells which are thin and perforated with fenestrations. These capillaries most often surround epithelia, like in

small intestine and exocrine glands;

3. Discontinuous capillaries, in addition to fenestrae, have large gaps. Thus, discontinuous capillaries are found for example in liver capillaries, called sinusoids, in which a large exchange of substances takes place.
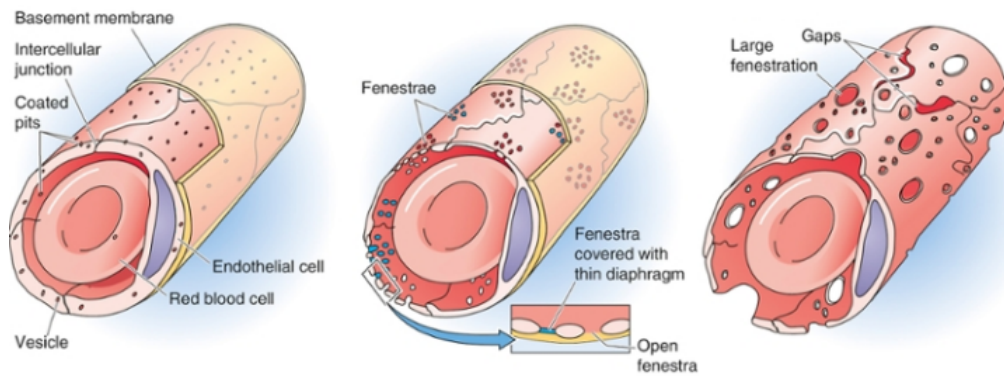
Figure 1.8: Continuous capillary (left), fenestrated capillary (center) and discontinuous capillary (right) (figure taken from [8]).

As mentioned above, microcirculation presents great diversity according to the perfused tissue: in intestinal capillaries a thin diaphragm closes the perforations of the fenestrae, several organs - liver, bone marrow, spleen - have capillaries with very large fenestrations (100 -1000 nm wide [8]) between adjacent cells. At their distal ends, capillaries merge into venules, characterized by an inner radius between 5 and 25 μm [8]. Venules carry blood back into low-pressure veins that return blood to the heart. Venules, as arterioles, can control local blood flow thanks to their VSMCs. They differ from arterioles because muscle cells layer is discontinuous. Furthermore, they may also exchange solutes across their walls.

1.3.1   Exchange of Solutes

As blood traverses a systemic capillary, O_2 diffuses across the capillary wall and into the tissue: there are many factors regulating exchange of O_2 and CO_2 across capillaries. One of them is the diffusional property of the perfused tissue: it regulates the O2 consumption by tissue and the radial diffusion coefficient (which governs O2 diffusion out of the capillary lumen). Another key factor is O_2 blood content, comprehending both free O_2 in arterial blood (proportional to the partial pressure of O_2 in the arterioles) and O_2 bounded with hemoglobin in red blood cells (which represent around the 98% of total O_2 in arterial blood flow [8]). Arterial blood is therefore characterized by a relatively high O_2 level.

The third and final element is the capillary structure and characteristics: blood flow, capillary radius, axial distance along the capillary and mean inter-capillary distance (which is given by capillary density and it varies depending of tissue oxygen consumption).

For a substance like O_2, which exits the capillaries, through extraction ratio it is possible to express the amount removed by tissues in a simple way:

$$E_{O_2} = \frac{[O_2]_a - [O_2]_v}{[O_2]_a} \qquad (1.9)$$

This parameter is the arteriovenous difference (i.e., the difference in concentration of a substance in the arterial inflow and venous outflow, for example of an organ), normalized to the arterial content of the substance.

The two most important factors, influencing both extraction ratio and exchange of solutes, are capillary flow and specific metabolic demand. The O_2 extraction ratio decreases with increased flow: a higher flow supplies more O_2 in the same time window, therefore tissue needs a smaller fraction of the incoming O_2 to satisfy its needs. On the contrary, considering O_2 consumption requires that tissue extract more O2 from bloodstream. Nonetheless, capillary density is important, but it has to be considered that not all the capillaries may be active at the same time in a tissue. For example, only 20% of capillaries in skeletal muscles are perfused at rest [8], while during a physical effort O_2 demand increases (blood flow and density of perfused capillaries increase significantly due to vasodilation). Vessel perfusion rate describes this phenomenon.

1.3.2 Regulation of Microcirculation

As said before, capillary blood flow is one of the crucial parameters which regulates the exchange of substances in microvasculature. VSCMs can actively contract, regulating pre-capillary and post-capillary resistance to blood flow, depending on the tone of arterioles and venules respectively. The resistance upstream of the capillary bed is also known as the afferent or pre-capillary resistance (R_{pre}). The overall resistance of a microcirculatory bed is the sum of R_{pre}, the resistance of the capillary bed itself (R_{cap}) and the efferent or post-capillary resistance (R_{post}). Blood flow (F_{cap}) is inversely proportional to these resistances:

$$F_{cap} = \frac{\Delta P}{R_{tot}} \qquad (1.10)$$

with

$$R_{tot} = R_{pre} + R_{cap} + R_{post} \qquad (1.11)$$

Due to the fact the aggregate R_{cap} is small, and R_{post}/R_{pre} is usually 0.3, R_{pre} is usually much greater than $R_{cap} + R_{cap}$ [8]. Because R_{pre} is the principal determinant of total resistance, capillary flow is roughly inversely proportional to R_{pre}. Thus, modulating the contractility of VSMCs in precapillary vessels is the main mechanism for adjusting perfusion.

Regulation of VSMCs tone is controlled by two separate mechanisms: a systemic and a local one. The first is the neural control that provides excitatory and inhibitory inputs that alter vascular tone through chemical synapses. The second is represented by humoral control given by circulating diffusible factors in the bloodstream. Similarly to skeletal muscles, increase in $[Ca_2{}^+]$ is the principal trigger of contraction and it can be driven also by humoral agents. Indeed, various membrane proteins are involved in controlling VSMCs contraction (i.e., vasoconstriction) and relaxation (i.e., vasodilation). Therefore, blood that flows into a specific vascular bed can be modulated independently of the systemic control by mean of tissue metabolites.

Regulation of local blood flow is also determined by intravascular content. There is an increasing evidence that red blood cells not only carry oxygen to tissues [20], but they are also able to locally sense and regulate oxygen delivery in the microcirculation, releasing substances like nitric oxide and adenosine triphosphate that act as strong vasodilators.

Looking further into the local control mechanism, the endothelium of capillary beds represents the source of several vasoactive compounds, including nitric oxide (NO) and endothelin (ET).

NO acts as potent vasodilator and it controls several mechanisms regarding platelets (aggregation, disaggregation, adhesion). Bradykinin and acetylcholine are two neurotransmitters which are able to stimulate the enzymes responsible for NO secretion (NOS III) present in endothelial cells. NOS can also be stimulated through an increased shear stress produced by blood flow on endothelial cells.

Once NO has been secreted, it diffuses locally and it enters VSMCs. By different and complex mechanisms - not treated herein - the NO released by endothelial cells relaxes VSMCs, producing vasodilation.

NO-mediated cascade is one of the most important mechanisms for vasodilation in the entire circulatory system. Physicians have used exogenous organic nitrates (e.g., nitroglycerin) for decades to dilate peripheral vessels for relief of the pain of angina pectoris [8]. Nitroglycerin breaks down in the blood stream releasing NO near VSMCs and therefore producing strong vasodilation.

The other key actor is the ET, a substance produced by endothelial cells able to cause potent and persistent vasoconstriction in VSMCs.

As final outcome, the autoregulation stabilizes blood flow despite large fluctuations in systemic arterial pressure.

In normal condition, an increase in pressure leads to dilation that decreases resistance causing a relationship between pressure and blood flow like the one depicted in Figure 1.9 with a red line. The autoregulatory capability of microvascular bed makes possible a relationship similar to the one described with the purple line in the same figure. Despite large changes in the systemic arterial pressure, they maintain local blood flow within a narrow range. These vascular beds behave more or less like rigid tubes at very low and at very high perfusion pressures. However, in the physiological pressure range over which autoregulation occurs, changes in perfusion pressure have little effect on flow. Instead, increases in pressure lead to increases in resistance that keep blood flow within a carefully controlled range.
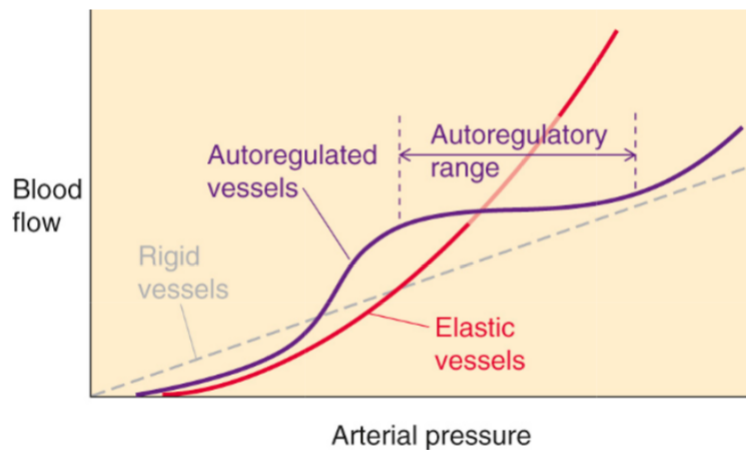
Figure 1.9: Microvasculature autoregulation: relationship between arterial pressure and blood flow.

The autoregulatory mechanism is an active process, therefore it is not immediate: vessel behaves as a rigid tube after a sudden increase in perfusion pressure. Then, arteriolar tone is adjusted and controlled values of flow are obtained.

Autoregulation is useful for at least two reasons. First, with an increase in perfusion pressure, it avoids a waste of perfusion in organs in which the flow is already sufficient. Second, with a decrease in perfusion pressure, autoregulation maintains capillary flow and capillary pressure. Therefore, it is crucial for organs that are very sensitive to ischemia or hypoxia (particularly the heart, brain, and kidneys) and for organs whose job it is to filter the blood (again, the kidney) [8].

1.4 Hepatic Microcirculation

Hepatic microvasculature is of extreme interest in pathophysiology because, given the parenchymatous nature of the liver tissue, microcirculation is the pivotal functional element of the several and vital hepatic functions.

Functionalities of liver microcirculation are several [21]:

1. correct parenchyma supply with oxygen and nutrients;

2. entrance gate for the leukocyte in hepatic inflammation;

3. clearance of toxicants and foreign elements from blood stream.

In clinical practice, acute liver dysfunction and failure represent life-threatening conditions, which require immediate intervention. Main causes of liver function deterioration are warm and cold ischemia and reperfusion (I/R) during liver resection and transplantation, generalized inflammation and sepsis. Microcirculatory dysfunctions have been shown to be determinants for the manifestation of these disease states [4]. Mechanisms of activation and dysfunction are of pivotal interest, not only for the understanding of the disease, but also for the development of novel therapeutic strategies.

Microvasculature undergoes complex phenomena, such interaction with cellular activation and mediator response. The cellular response includes the accumulation and activation of leukocytes, platelets, and Kupffer cells (KC), while the mediator response consists of pro-inflammatory cascades with release of chemical and reactive oxygen species. Microcirculatory deteriorations are characterized by vasoconstriction, interruption of sinusoidal circulation and parenchyma hypoxia, leading to organ failure.

1.4.1 Dual Blood Perfusion of the Liver

Liver receives 25% of the cardiac output via two inflows: the portal vein and the hepatic artery. Both vessels enter the liver at its hilus. Portal vein is a valveless afferent vessel which drains blood from the capillary system of the intestine, spleen, pancreas, and gallbladder: it contributes to liver blood supply with 75 - 80% of its total inflow. The remaining 20 - 25% is delivered by the hepatic artery. Total hepatic perfusion amounts to around 1 $ml \times min^{-1} \times g^{-1}$. In contrast to the well-oxygenated hepatic arterial blood, the portal vein carries nutrient-rich de-oxygenated blood. Nevertheless, more than 50% of the hepatic oxygen requirement is provided by the portal venous to its high flow rate. Furthermore, the efferent system is given

by hepatic veins.

The hepatic artery is a vessel of resistance, whereas the portal and hepatic veins are vessels of capacitance. Thus, the liver is interposed in an arterial high-pressure and a venous low-pressure system. There is an particular relationship between the two vascular systems, called "hepatic arterial buffer response" (HABR), representing the ability of the hepatic artery to produce compensatory flow changes in response to changes in portal venous flow [22]. In addition to the intrinsic mechanism of classical arterial autoregulation (i.e. the myogenic constrictive response of the hepatic artery if arterial pressure rises) it exists a second intrinsic mechanism: the hepatic artery dilates if portal flow decreases; viceversa, the hepatic artery constricts if portal flow increases. Hereby, the hepatic artery is not regulated by the metabolic demand of the liver.

Hepatic arterial flow regulates nutrients level and hormones by maintaining blood flow and hepatic clearance as steady as possible. Due to the fact that portal vein can not control its blood flow, given by the sum of outflows of the extra-hepatic splanchnic organs, there is no reciprocity of the HABR (i.e., alterations of the hepatic arterial perfusion do not induce compensatory changes of the portal vascular flow or resistance) [22].

1.4.2 Anatomy of the Hepatic Microvascular Bed

In the portal tracts, several components travel parallel to each other through liver parenchyma: branches of the hepatic artery, the hepatic portal vein, the main bile duct and the main lymphatic vessels. After repeated branching, terminal hepatic arterioles and terminal portal venules - diameter of 15 - 35 μm, length of 50 - 70 μm [21] - supply hepatic sinusoids with blood. In the parenchyma, they lose their basement membrane, becoming fenestrated: these are the sinusoids.

Hepatic sinusoids are the capillary bed of the liver and they represent microcirculation segments in which supply of nutrients and removal of metabolic products takes place. Main sinusoids run straight between the liver cell cords over a length of 250 μm and communicate with each other through shorter interconnecting sinusoids running across the liver cell cords. Sinusoidal diameters range from 7 to 15 μm [23]. Sinusoids are characterized by a unique type of lining consisting of endothelial cells with flattened processes perforated by small fenestrae. Fenestrae form groups of 10 - 50 pores, called "sieve plates", which occupy around 8% of the endothelial surface, not uniformly in size and distribution throughout sinusoids [21] (Figure 1.10).
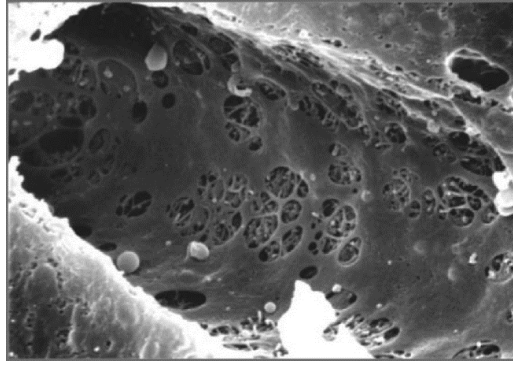
Figure 1.10: Lumen of the hepatic sinusoid: fenestrae grouped together form the sieve plates (figure taken from [21]).

Fenestrae are dynamic structures: they respond to alterations in sinusoidal blood flow and perfusion pressure by contracting and dilating. Furthermore, they act as a selective sieving barrier to control the extensive exchange of material between blood and liver cells [24] and, viceversa, contributing to the homoeostatic control of the hepatic microcirculation. In addition, they clear blood from many molecular waste products. Furthermore, the unique morphology of the liver sinusoidal-endothelial cells (SEC) permits interactions between lymphocytes and hepatocytes.

A unique cellular component of the hepatic sinusoids are particular cells, called "stellate" cells. They are located in the space between the basal microvilli-rich surfaces of hepatocytes and the sinusoidal lining cells - space of Disse. Stellate cells are supposed to play a central role in the regulation of blood flow through sinusoids [25].

In addition to the peri-sinusoidal stellate cells, hepatic sinusoids cellular component is made also of KCs. In contrast to stellate cells, which are distributed almost homogeneously on the different liver lobule zones, majority of KCs is found in peri-portal regions: these KCs are larger and with a greater phagocytic activity than KCs located in the peri-lobularregion. KC represent a flow hindrance and are considered as contractile cells contributing to blood flow regulation through sinusoids.

Thus, hepatic microcirculatory unit is made of the two terminal afferent vessels, the network of sinusoids and the efferent terminal hepatic venule [21].

17
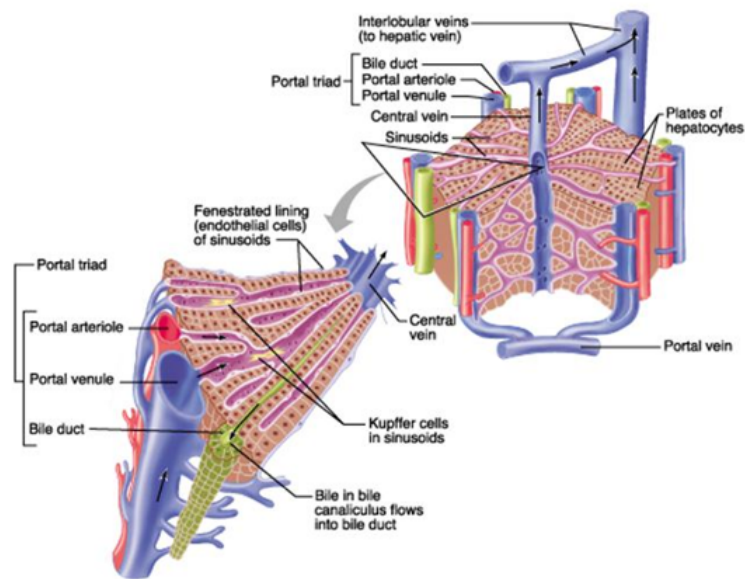
Figure 1.11: Schema of the hepatic lobule and of the portal triad composed by portal arterioles, portal venules and bile duct.

1.4.3   Regulation of the Hepatic Microvascular Blood Flow

All the aforementioned vascular segments represent potential sites of regulation of blood flow. In addition to the presence of smooth muscle cells in the afferent and efferent vessels, sinusoids contain contractile cells (e.g., stellate cells, KCs), involved in the blood flow regulation process.

According to direct blood pressure measurements - micropuncture of hepatic microvessels - the blood pressure in the terminal hepatic arteriole is at least $300-400$ mmH$_2$O, while in the terminal portal venule is 50 mmH$_2$O; sinusoidal pressure is estimated to be $10-20$ mmH$_2$O [21].

There is a large body of evidence that hepatic microvascular blood flow is regulated and redistributed at the level of the microcirculation [23], basing of the fact that both stellate cells and endothelial cells actively control some microvasculature functions. The major site of blood flow regulation through sinusoids is recognized to reside in the sinusoids themselves, where the most pronounced blood pressure drop occurs in the liver.

The interaction of cellular components and mediator systems is extraordinary complex.

Endothelial mediators which control vascular tone under both physiological and pathological conditions are: nitric oxide, which is endothelium derived relaxing factor, endothelins - en-

dothelium constricting factors - and gaseous molecules which act as vasodilators ([26],[27]). Hepatic cellular sources of ETs are SECs, stellate cells, and KCs. Main action of ET is the narrowing of sinusoidal lumen, even if the ET-dependent action strongly depends on the temporal and spatial distribution of ET receptor expression. Based on a critical balance between vasoconstrictor and vasodilator agents, ET is counteracted by the vasodilating mediators NO and CO.

NO is mainly synthesized by enzyme Endothelial NOS. In arteriolar resistance vessels, NO diffuses into smooth muscle cells and it activates a cell-signaling pathway, which results in smooth muscle relaxation. Under basal conditions, NO regulates the vascular tone of the hepatic circulation [28]. NO seems to serve as a potent vasodilator in the hepatic arterial circulation, but it exerts a minor vasodilator effect in the portal venous bed [22].

CO is thought to be an endogenous modulator of hepatic sinusoidal perfusion through a relaxing mechanism involving stellate cells [27]. Furthermore, CO maintains portal venous vascular tone in a relaxed state [21], instead in hepatic artery there is no intrinsic CO-mediated vasodilation.

1.5   Small Intestine Microcirculation

Another district whose microcirculation has recently attracted much attention in clinical and physiological literature is gastrointestinal circulation.

The splanchnic bed receives 25 - 30% of the cardiac output under resting conditions, and increases of 30 - 130% are observed in the postprandial period. In human, basal blood flow in small intestine ranges between 30 and 70 $ml \times min^{-1} \times 100g^{-1}$ [29].

Mesenteric arteries deliver blood to small and large intestine. Into the organ, the flow is mainly received by the mucosa. Then, portal venous system drains nutrient-rich blood to liver.

1.5.1   Anatomy of Intestine Microvasculature

Anatomy of small intestine is schematically represented in Figure 1.12, which shows in detail the structure of blood vessels and mucosa. Each single villus is traversed by a central arterial vessel from which starts a dense network of capillaries, that lies close to the epithelial layer, ending into a venous vessel that flows into portal venous system. Furthermore, a single lymphatic vessel, called lacteal, lies in the center of the villus, approximately 50 μm from the epithelial layer.
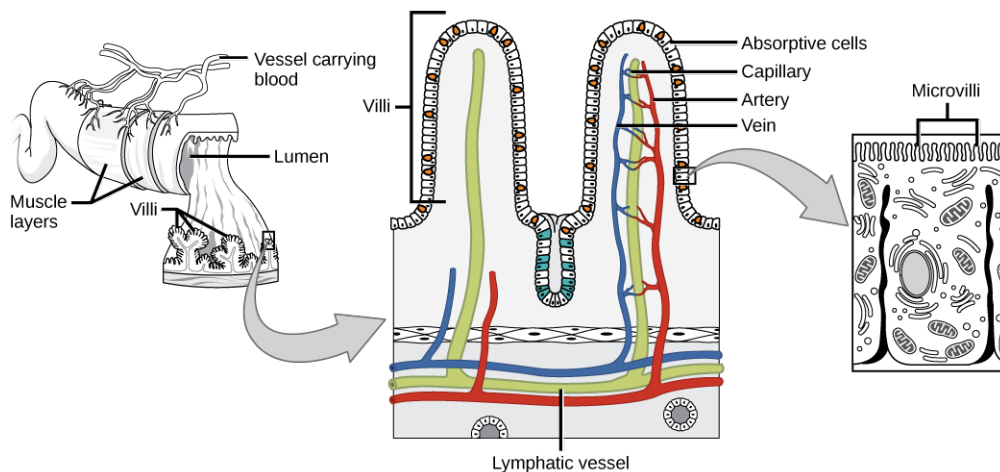
Figure 1.12: Schematic representation of intestinal villi.

1.5.2 Physiology of Intestine Microcirculation

Microcirculation is the functional microstructure which makes absorption of nutritive substances from the intestinal lumen possible. This function is regulated by the tone of arteriolar VSMCs, which allow to control flux of both nutrients and oxygen. Beyond that, precapillary sphincters are able to modulate density of perfused capillaries.

Several mechanisms allow transfer of water and solutes through capillary wall. Fenestrae account for most of the exchanged substances. They can be open or diaphragmed, having radii respectively of 20 - 30 nm and less than 10 - 15 nm. About 10% of total capillary hydraulic conductivity is given by pores with radius of 0.4 - 1 nm that creates channels for very small water-soluble substances. Finally, intercellular junctions allow crossing to molecules smaller than 1 nm [29].

Lymphatic vessels differ with respect to capillaries because they have a fragmentary basement membrane. This makes easier for solutes and large lipoprotein particles to access the lymphatic lumen.

Starling equation describes the fine balance between hydrostatic and oncotic forces (i.e., osmotic pressure exerted by proteins), which rules fluid flux across the capillary wall. The equation is expressed as:

$$J_L = J_{V,C} = K_{f,c}[(P_c - P_t) - \sigma_d(\pi_c - \pi_t)] \tag{1.12}$$

where J_L is the lymph flow and $J_{V,C}$ the rate of capillary filtration or absorption (respectively characterized by a positive or negative value). $K_{f,c}$ is the capillary filtration coefficient, Pc and Pt are the hydrostatic pressures of the capillary blood and tissue fluid and π_c and π_t the corresponding oncotic pressures. σ_d is the osmotic reflection coefficient, which expresses the relative permeability of the particular capillary bed to proteins. For example, liver sinusoidal wall, due to its high permeability, is characterized by a σ_d close to zero, while in high impermeable capillaries it approaches unity. The σ_d for intestine equal to 0.92: this value expresses a strong restrictive property of the intestinal microcirculation to wards protein.

Schema in Figure 1.13 shows elements and variables involved, considering the rest state. In this case, forces involved favour a slight filtration. This example shows the fine regulation of blood and lymphatic microcirculation in intestinal physiology, through which homoeostasis of the interstitium is maintained.
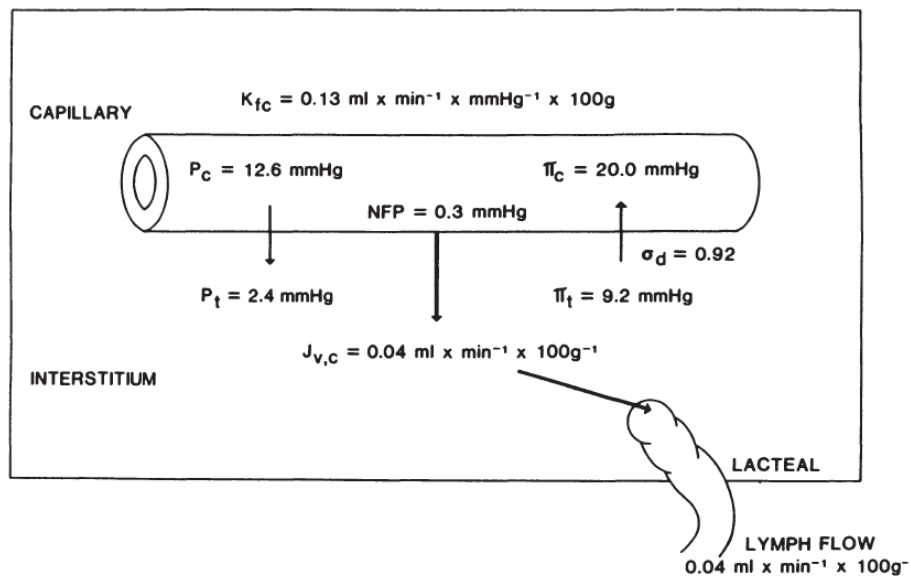
Figure 1.13: Example of balance between hydrostatic and oncotic forces in the intestine microvasculature.

Chapter 2

State of the art

2.1 Microcirculation Imaging Techniques

Given the importance of the assessment of microcirculation functionality, different imaging methods have been developed in the last decades to directly visualize it at the bedside in a non-invasive way.

In the current section, the following techniques are described, highlighting their advantages and their drawbacks:

- Near-Infrared Spectroscopy (NIRS)

- Orthogonal Polarization Spectroscopy (OPS)

- Sidestream Dark Field imaging (SDF)

Before their introduction, the only imaging system available to analyse microcirculation was Intravital Microscopy (IVM), which is a light microscopy-based technique. IVM has never been used for clinical applications because of the required use of fluorescent labels for contrast enhancement ([11], [30], [31], [32]), which can cause phototoxic effects in biological tissues: therefore, IVM can not be used on patients.

Furthermore, another disadvantage is the large size of the intravital microscope equipment, which limits its use ([11], [30]).

2.1.1 Near-Infrared Spectroscopy

Near-Infrared Spectroscopy (NIRS) is a non invasive imaging modality which allows low cost measurements of tissue oxigenation (SatO$_2$) [33].

It is a special type of spectroscopy, characterized by the use of electromagnetic waves with wavelength belonging to the near-infrared (NIR) region: usually, in NIRS wavelength λ is in the range $780 \div 2520$ nm [33].

The light crossing the tissue could undergo scattering and it could be totally absorbed, avoiding any light to reach the detector: NIR wavelength is used because of its intrinsic deeper penetration capability, that is required for the correct image formation. Indeed, it has been shown that NIR radiation has the most efficient penetration capability [10] - in general, longer wavelength penetrate deeper -, even higher than the one of visible light, in which wavelength range absorption by water and lipids becomes dominant (Figure 2.1).
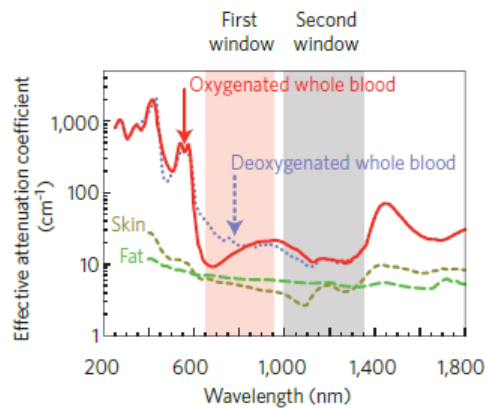
Figure 2.1: *Attenuation coefficient for different types of tissue (particularly for oxygenated and de-oxygenated blood): in the NIR wavelength region, the coefficient has its lowest value (figure taken from [10]).*

The detector system is made of optic fibres and it can be put on the other side with respect to the radiation source - transmission spectroscopy - or on the same side of it - reflectance spectroscopy. The type of imaging modality is mainly chosen based on optical properties of the sample (i.e., if the sample is highly transparent, transmission spectroscopy is more suitable).

Vessels with different oxygen saturation can be distinguished because of the different spectra absorption of de-oxygenated haemoglobin (Hb) vs. oxygenated haemoglobin (HbO$_2$) at NIR frequencies.

Instrumentation of NIR spectroscope is the typical instrumentation of spectroscopy system (Figure 2.2). It is composed of light source, monochromator to convert polychromatic light to NIR light, sample to be analysed, detector.

There are several types of radiation sources (i.e., tungsten halogen lamp) and of detectors:

the most used are the Silicon ones because of their fast response and high sensitivity in NIR range [10].
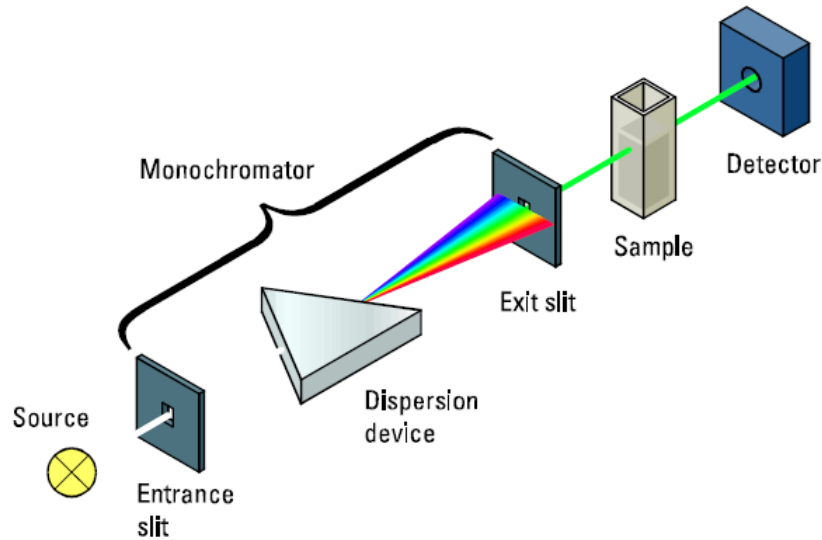
Figure 2.2: Instrumentation of spectrophotometer: the white light is split into monochromatic light and the desired wavelength is sent to the sample; the light exits the sample and it reaches the detector where it is processed.

The NIR imaging system is composed by the spectrometer instrumentation combined with a digital image processing system. This part is made of spectral encoder and focal plane array (FPA): data are collected and the result is a three-dimensional dataset, with the spatial information on the $x - y$ plane and the spectral information of the z axis.

Thanks to NIRS, it is possible to visualize the spatial distribution of chemical species, determining the heterogeneity of the sample. Furthermore, this imaging technique enables the possibility to obtain quantitative information from spectral components that are directly available from the imaging system.

Unfortunately, the main drawbacks which must be taken into account is the too low penetration depth which can be achieved by light, limiting NIR imaging use for internal regions of body.

2.1.2 Orthogonal Polarization Spectroscopy

The use of fluorescent dyes in IVM and the impossibility to observe deep structures with NIRS make the application of these imaging techniques inappropriate for human microcirculation.

Due to the lack of a clinical tool able to provide diagnostic information regarding microcirculation and given the importance of its assessment in pathological cases ([4], [3]), Orthogonal Polarization Spectroscopy (OPS) has been developed.

In OPS imaging the target tissue is illuminated with polarized light. Polarization is preserved in reflection if no scattering events - or few events - happen: consequently light reflected from the surface tissue to the detector does not contribute to the image. On the other hand, depolarization is obtained by several scattering events and light travelling under the surface undergoes many scattering events.

Therefore, the image is composed only by light reflected from deeper depth than tissue surface. As in NIRS, the contrast is obtained by the different light absorption of medium and haemoglobin-carrying structures appear in negative contrast.

The wavelength of radiation corresponds to the isosbestic point of haemoglobin (i.e., extinction coefficients of Hb and HbO_2 are the same): oxigenated and de-oxygenated haemoglobin are not distinguishable with OPS.

A schema of the probe of OPS imaging system is shown in Figure 2.3. The site most used for the direct visualization of microcirculation is sublingual area ([34], [12]), because it is easibly accessible and it is considered as a possible surrogate measure for slpanchnic blood flow [35].
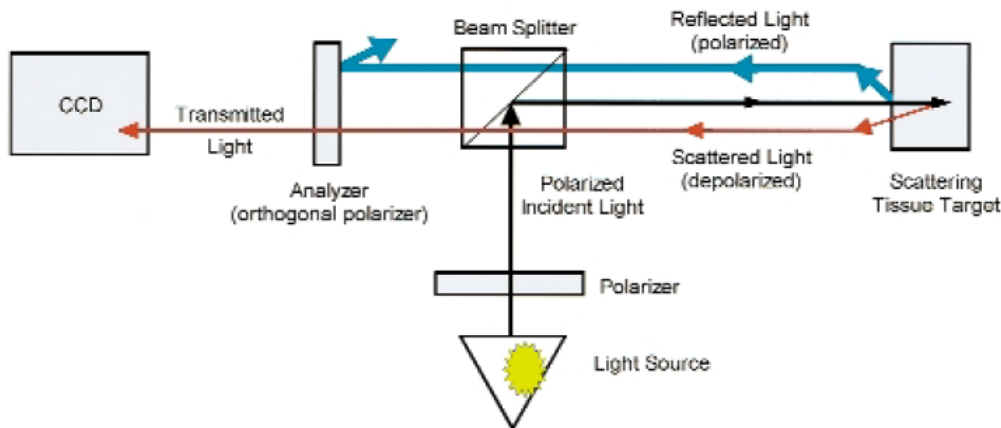
Figure 2.3: OPS probe: the tissue is illuminated with polatrized light; the remitted light from the target tissue is analysed through a polarizer oriented orthogonal with respect to the incident polarization and it is collected on a CCD videocamera (figure taken from [12]).

Thanks to the high contrast images, with OPS it is possible a quantitative determination of vessels diameter, RBCs velocity, perfusion rate. Through calculation of these parameters,

OPS imaging has been validated with respect to standard IVM technique: between them comparable results have been found ([11], [30], [12]), enabling the use of OPS as tool for direct measurement of parameters both in physiological and pathological conditions.

Although OPS is a direct, non-invasive and easy-to-handle imaging system, it presents some drawbacks which limit its everyday use in clinical settings:

1. Small field of view (FOV, 1 mm^2) and low penetration depth (lower than 1 mm);

2. structure without haemoglobin (i.e., leukocytes, platelets) are not visible, parameters are calculated only for RBCs-containing structures ([11], [30]);

3. images are blurred due to motion caused by OPS device, tissue and flowing RBCs ([13], [32], [34]), leading to a suboptimal capillary visualization;

4. application of the OPS probe causes disturbances in microcirculation, leading to a more complicated calculation of RBCs velocity [32];

5. strong light source is required, because most of the light is reflected by tissue surface, and consequently adequate power supply is needed, limiting the clinical applicability of OPS [13].

Due to all these disadvantages of OPS, a new imaging system has been designed: Sidestream Dark Field imaging.

2.1.3   Sidestream Dark Field imaging

Sidestream Dark Field imaging (SDF) has been introduced to replace OPS imaging. This new technique works in the following fashion based on OPS technology: a light guide is surrounded by LEDs - light emitting diodes - at isosbestic wavelength of haemoglobin ([34], [13]), which provide sidestream dark field illumination. All the core of the light guide is provided with lens optically isolated from the ring of LEDs, avoiding image to be contaminated by reflections coming from tissue surface (Figure 2.4).

Consequently, better image quality is obtained and in order to further improve it, LEDs provide pulsed illumination in synchrony with the frame rate of CCD camera: stroboscopic imaging is performed and blurring in the final image is limited compared with OPS modality. Also SDF imaging has been validated compared to OPS system: microcirculation parameters calculated with both techniques show very similar values, allowing the use of SDF instead of OPS ([13], [32]).

27
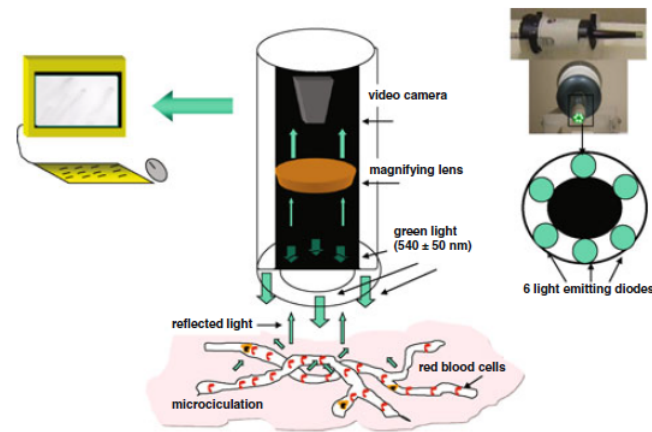
Figure 2.4: SDF imaging technique: the videocamera is put on the center of the core, capturing the reflected light to form the final image (figure taken from [32]).

Advantages compared to OPS are visible in Figure 2.5, especially regarding the higher contrast and the less blurring effect.
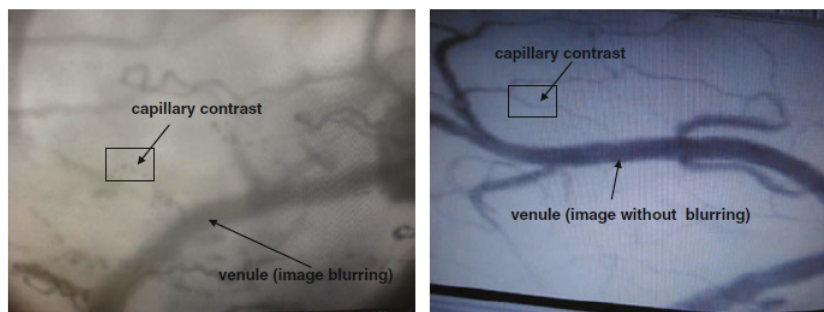
Figure 2.5: Comparison between OPS (left) and SDF imaging (right): the contrast is higher and venules are less blurred in the SDF image (sublingual mucosa image - figure taken from [32]).

Furthermore, another advantage of SDF is that the power required for the system is lower than the one required in OPS and thereby the clinical applicability increases [13]. Unfortunately, some drawbacks are still present:

1. detectable velocity is limited, also due to the low frame rate (typical of 25 frame per second);

2. the application of the probe still induces some modification on the microcirculation (i.e., pressure changes) causing problems in the parameter calculations;

3. different types of white blood cells can not be assessed;

4. the maximum penetration depth is 0.5 mm, allowing studies of microcirculation just on epidermis and upperdermis [32];

5. small field of view, about 1 mm.

For all the cited problems, this high contrast method is more suitable for research purposes. For clinical settings, a new imaging technique based on ultrasounds is under development in the Esposti Lab. where this research study has been performed.

2.2 Microcirculation parameters

Through the aforementioned technologies, it is possible to measure some microcirculation parameters under certain conditions. Different scoring systems are used, making hard an efficient comparison between results from different studies. This is why experts in cardiology and medicine gathered in Amsterdam in 2006 to discuss about a common scoring system describing numerically microvasculature images [36].

From this meeting, participants identified the following parameters:

1. Measurement of vessel density: total and perfused vessel density (PVD)

2. First index of perfusion: proportion of perfused vessels (PPV)

3. Second index of perfusion: microcirculatory flow index (MFI)

4. Heterogeneity index

2.2.1 Total and perfused vessel density

This parameter considers that total vessel density is proportional to the number of vessels crossing arbitrary lines. The index is calculated as the number of vessels crossing the lines divided by the total length of the lines. Regarding the perfused vessel density, perfusion is observed by eye and categorized as present (continuous flow for at least 20 s), absent (no flow for at least 20 s) or intermittent (at least 50% of time with no flow). A 20 μm cut-off is used to separate small vessels, that are mostly capillaries, from large vessels, that are mostly venules (Figure 2.6).
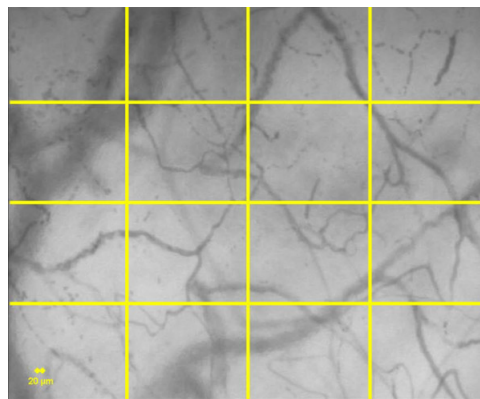
Figure 2.6: Grid for vessel density calculation (figure taken from [36]).

2.2.2 Proportion of perfused vessels

Proportion of perfused vessels is computed in a very simple way:

$$PPV = 100 \times \frac{PVD}{TVD} \tag{2.1}$$

where TVD is the total perfusion density and PVD the perfused vessel density.

2.2.3 Microcirculatory flow index

Boerma et al. [5] created a method for flow score quantification. The image is divided into four quadrants and the predominant type of flow (absent = 0, intermittent = 1, sluggish = 2, and normal = 3) is assessed in each quadrant. The Mean Flow Index (MFI) score represents the averaged values of the four (Figure 2.7).
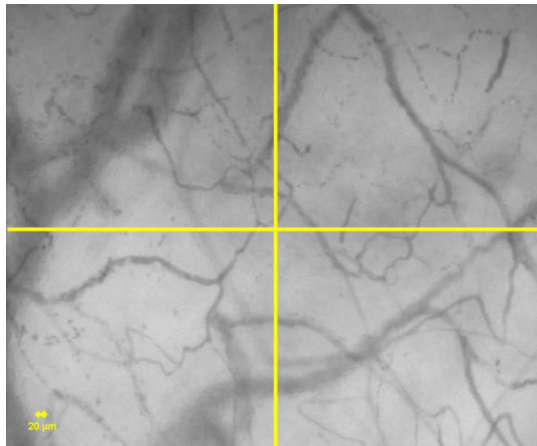
Figure 2.7: Grid for mean flow index calculation (figure taken from [36]).

2.2.4 Heterogeneity index

Trzeciak et al. [9] developed an interesting index to assess flow heterogeneity between the different investigated areas. Heterogeneity index has been calculated as the highest site flow velocity minus the lowest site flow velocity, divided by the mean flow velocity of all sublingual sites.

According to De Backer et al. [36], the usefulness of determining the speed of blood in vessels is uncertain. Indeed, cells are able to regulate oxygen extraction also with variable flow, therefore, in order to obtain functional microvasculature, is much more useful achieving homogeneity of perfusion.

All the proposed parameters have been computed manually, of course the authors stated that an image analysis software could ease the analysis. An overview of these software is provided by Demir at al. in 2012 [37].

CapImage [38], developed initially for intravital microscopy, has been successfully applied to OPS and SDF images. Its algorithm stabilizes video recordings, segments blood vessels, identifies vessels without flow and calculates FCD in a fully automated process. CapiScope and AVA (Automated Vascular Analysis) are the other two main software with different accuracy and level of automation.

Puhl et al. [31] analysed hepatic OPS images by mean of CapImage. The software allows to compute an offline estimation of sinusoidal diameter (D), functional sinusoidal density and red blood cell velocity (RBCV) within the sinusoids. Furthermore, volumetric blood flow (VBF) within the sinusoids can be expressed as:

$$VBF = \frac{\pi}{4}D^2RBVC \tag{2.2}$$

The parameters seen in this section have primary importance in clinical settings because a derangement of these indexes appears to be one of the critical pathogenic events in sepsis [39], which is the most common cause of death in general critical care units, and it has been associated with organ failure [40] and mortality [41].

2.3   Functional Ultrasounds

2.3.1   Ultrafast Compound Doppler Imaging

In order to visualize and consequently analyse vessels with a diameter of few micron, conventional Doppler techniques can not be employed because of their too low sensitivity to detect blood flow in the vessels of interested ([16], [15]).

Another limitation of standard US imaging methods is their frame rate, which varies around few herts, reaching a maximum of few tens of hertz ([16], [42]). The frame rate depends on the number of scanning lines used during the acquisition process: a small number of lines reduces the time of the total acquisition - increase of the frame rate - but it worsens the spatial resolution of the image.

Even if the frame rate can be considered good compared to other imaging modalities (e.g., magnetic resonance), it must be noticed that the goal of the Doppler US imaging is the correct detection of flowing blood. Therefore, it is preferable to have a system which ensures the spatio-temporal continuity: with the current B-mode through which images are acquired with a focused beam on each line, this continuity is lost.

To solve these limits, it has been introduced a new method of image acquisition, based on plane-wave transmission on the entire object of interest ([16], [42]).

This technique, called Ultrafast compound imaging, consists of the insonification of the medium with plane waves, which are transmitted at different angles: there are no more scan lines as in B-mode, at each acquisition all the medium is crossed by ultrasounds (the total number of acquisition is equal to the number of angles, N_{angles}).

After the collection of N_{angles} beamformed images, these are coherently summed in order to form the final compounded image.

The use of plane waves increases the frame rate, which is dependent on the number of chosen angles - a decrease in the angles number causes a higher frame rate, at the expense of image resolution and quality, resulting in a trade-off between them - and largely decreases the time of the acquisition of the entire image (Figure 2.8).

It has been proved [42] that compound imaging has a higher SNR and especially a higher sensitivity compared to the other Doppler techniques: this is due to the fact that summing up an higher number of images taken at different angle leads to delete the effect of random variables, which act as noise in the image. Indeed, for every pixel, the signal $s(x, y)$ is measured

as the mean value of the echo $z(x, y, t_i)$ gathered at each acquisition:

$$s(x, y) = \frac{1}{N} \sum_{i=1}^{N} z(x, y, t_i) \qquad (2.3)$$

where N is the total number of images (i.e., of acquisitions), which is higher in the compound imaging, resulting in a better noise attenuation. Consequently, SNR is increased with respect to the SNR of conventional Doppler method.

The increase in sensitivity makes the ultrafast compound imaging method the ideal candidate for analysis of low blood flow (i.e., microcircualtion).
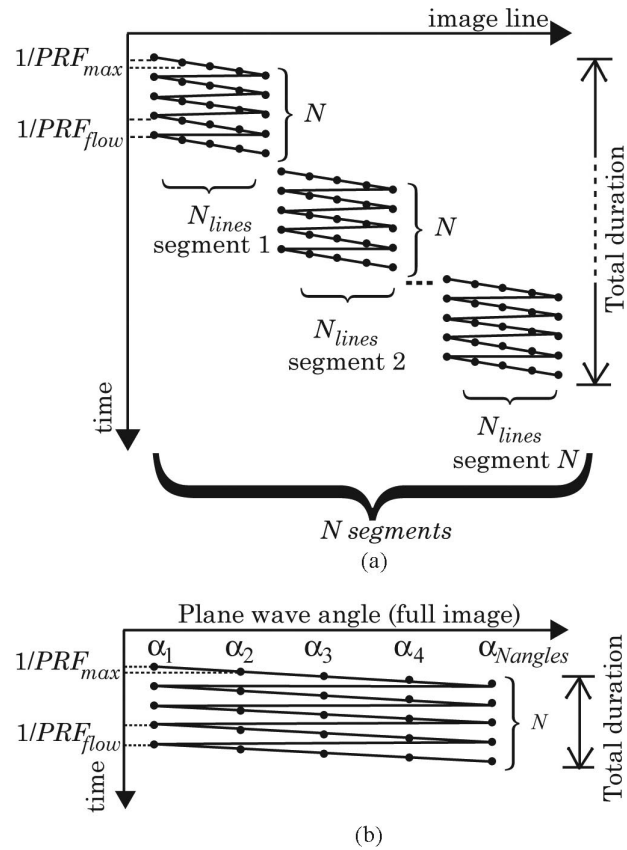
Figure 2.8: Comparison between conventional color Doppler mode (a) and ultrafast compound Doppler (b). In the former method, the image is scanned by lines, while in the latter the wave is sent to all the medium with a certain angle: the duration of the ultrafast compund Doppler is clearly shorter. - PRF_{max} is the maximum Pulse Repetition Frequency achievable by the system at the considered depth, PRF_{flow} is the necessary PRF to detect the desired maximum flow velocity, α_i are the different angles (figure taken from [16]).

2.3.2 Functional Ultrasound Imaging of the brain

A new imaging technique based on coherent compounding method has been developed, in order to analyse blood dynamics in microvasculature [15]: from now on, this kind of US imaging will be called μDoppler imaging.

μDoppler is performed *in vivo* and it is based on Power Doppler imaging.

Usually, power Doppler signal of each pixel undergoes precise steps of processing operations in order to obtain a final image as clean as possible: firstly, signals $z(x, y, t_i)$, where t_i are the temporal consecutive pulse emission, are demodulated - I/Q demodulation, used in medical ultrasound imaging to derive the envelope of the received radio-frequency signal - and successively they are beamformed; then a clutter filter - high pass filter - is applied to every pixel with the goal of removing tissue motion component.

The final pixel signal $z_F(x, y, t_i)$ is made of two main components: the Doppler component $z_D(x, y, t_i)$ and the noise component $z_n(x, y, t_i)$.

With Power Doppler mode, the mean intensity of each pixel is taken into account: this quantity is more suitable for microcirculation analysis [15], because it is more robust and less sensitive to aliasing compared with color Doppler signal. The intensity is calculated with the following expression:

$$I(x, y) = \frac{1}{N} \sum_{i=1}^{N} |z_F(x, y, t_i)|^2 \qquad (2.4)$$

from which it can be easily noticed that the higher the number N of samples acquired, the lower will be the effect of noise on the image and consequently also the sensitivity will increase.

Information related to blood velocity and its direction are not available because of the Power Doppler characteristics, but signal is directly proportional to the blood volume of the single voxel: variations of blood flow rate are still visible.

The μDoppler method has been specifically designed to augment the number of samples mentioned above to obtain images which provide the visualization of the smallest vessels (i.e., of the slowest fluxes).

Study described in [15] has been conducted on rat brain. The chosen acquisition time is 0.32 seconds, through which is possible to generate real-time brain activation map, thanks to the high frame rate of this innovative method.

As described in 2.3.1, the coherent sum of images acquired at several angles allows an increase of the frame rate: μDoppler makes use of this method and, as suggested in [16], the number

of plane waves chosen in [15] is 16, each of them tilted at a different angle (from $-7°$ to $8°$ by steps of 1). Time for building one compounded image is 1 ms, using a PRF (Pulse Repetition Frequency) of 16 kHz.

Images are acquired and then they are coherently added to form the final compound image. At the end of the acquisition time, the total amount of compound image collected is 320: pixel signals now are processed as conventional Doppler image (Figure 2.9).
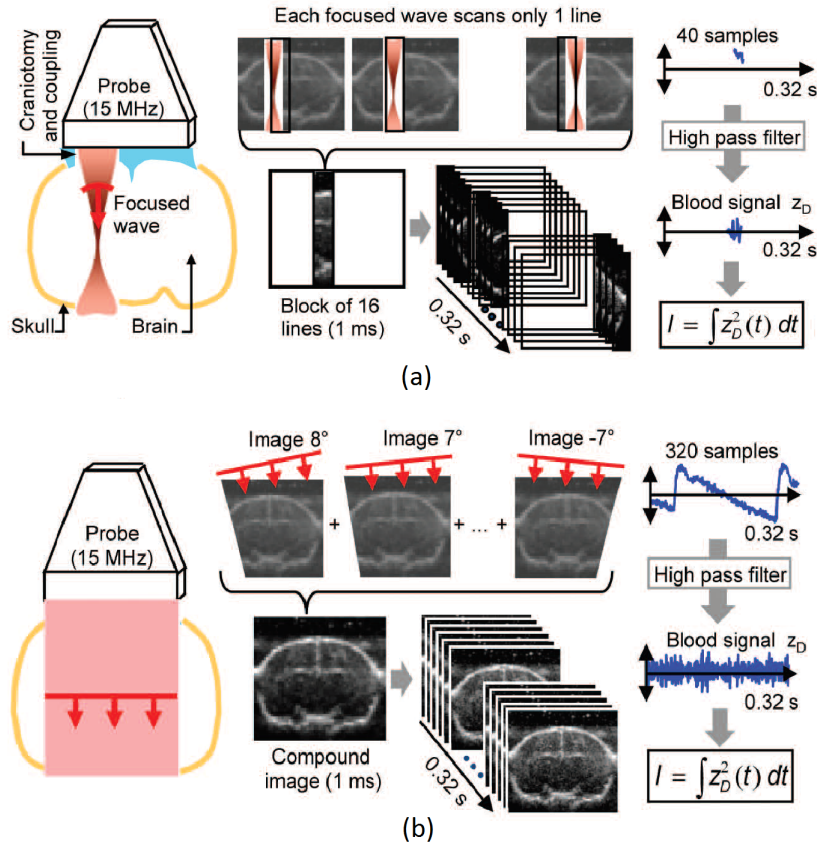
Figure 2.9: (a) Acquisition of US Doppler image with the conventional method: the US wave emitted is focused on a line. (b) Acquisition of US Doppler image with the µDoppler method: plane-waves are used, a set of images obtained at defined angles is summed together to generate the compound image (figure taken from [15]).

Considering a image 2-cm-deep, a comparison can be done between the number of images acquired with the conventional Doppler imaging and the one with µDoppler.

In the first case, the image is divided into blocks (in [15], 8 blocks) and each of them is scanned 40 times at frequency of $1kHz$:

$$N_{images} = \frac{f_{samp}}{N_{blocks}} t_{acquisition} = \frac{1kHz}{8} 0.32s = 40 \qquad (2.5)$$

In the second case, the image is not divided into blocks, resulting in a number of images acquired in the same acquisition time N_{blocks} times higher.

This large difference in the number of acquired frames causes a difference in the quality of the final image: the one obtained with the μDoppler is visibly less sensitive to noise and biological structures are more defined (Figure 2.10).
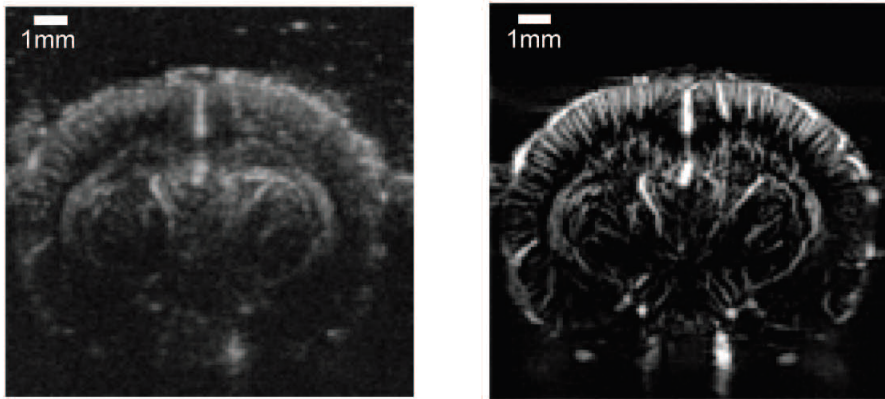
Figure 2.10: Final images generated by the two described methods: left image is obtained by conventional Doppler, while the right one is the μDoppler image (figure taken from [15]).

2.3.2.1 Sensitivity gain

In the field of imaging, sensitivity can be defined as the capability to detect small variations of objects and enable a clear visualization of them.

The huge increase in sensitivity of the μDoppler method is caused by two main factors which are closely connected:

1. increase of the number of samples acquired in a certain acquisition time, which leads to a decrease of noise effect on pixel signals (see equation (2.4));

2. improvement of SNR (signal to noise ratio), directly caused by the higher number of samples; it has been proved [15] that SNR of compound images is always higher than SNR of focused-wave images, except at focal depth where their values are comparable.

Generally speaking, a vessel is visible only if it generates a signal (i.e., Doppler intensity) higher than a certain threshold, which depends on the level of noise superimposed on the image (Figure 2.11).

Therefore, a level of uncertainty can be established, under which the Doppler signal is not detected. The chosen level in [15] is:

$$I_D(x,y) > 3\sigma_I(x,y) \tag{2.6}$$

where $\sigma_I(x,y)$ is the standard deviation of the mean intensity signal. This last quantity is defined as:

$$\sigma_I(x,y) = \frac{(I_D(x,y) + I_\eta)}{\sqrt{n_{eff}}} \tag{2.7}$$

n_{eff} is the number of samples after having filter the signal - the first k samples are rejected because of filter oscillations - while I_D and I_η are the variances of Doppler signal and noise.
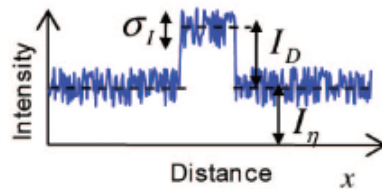
Figure 2.11: Sensitivity problem: the acquired signal is the sum of Doppler signal and noise signal with its fluctuations; Doppler signal is detectable only if it is higher than the level of noise fluctuations (figure taken from [15]).

Combining expression (2.7) with the condition (2.6), we obtain:

$$I_D > \frac{3I_\eta}{\sqrt{n_{eff}} - 3} \tag{2.8}$$

The formula highlights that the threshold to overcome in order to visualize the Doppler signal is directly proportional to the noise level, which is lower in μDoppler technique, and inversely proportional to the number of samples, which, on the contrary, is higher in the μDoppler. Consequently, the sensitivity of the μDoppler imaging system is better than the one of conventional Doppler imaging.

2.3.2.2 Clutter filter

The clutter filter is a high pass filter. It is responsible for rejecting the portion of the Doppler signal due to tissue motion, which originates from stationary reverberations and muscular movements.

This contribution is strong - typically from 40 to 100 dB stronger than blood signal [43] - and it must be deleted, otherwise the detection of blood velocity, especially velocities characterized

by low frequencies (i.e., slow dynamics), will be biased.

The filter used in [15] is a 5-th-order Butterworth filter, the cut-off frequency is set to 75 Hz. As any type of filter, the higher is the number of samples of the signal, the easier it is the filtering operation: with μDoppler imaging there is this advantage, compared to the conventional Doppler approach.

Leaving out frequency components lower than 75 Hz, will automatically cause non-acquisition of echoes produced by blood moving with a velocity which generates a Doppler frequency lower than cut-off frequency.

This inferior limit of velocity detection is 4 mm/s [15], while velocities upper than 10 mm/s are well identified. In the velocity range between lower and upper limit, signal is partially detected because of the slope of the filter (i.e., its transition band).

2.3.2.3   Directional information of blood flow

Another advantage of the μDoppler approach is the possibility to visualize direction of blood flow, by splitting the image into the positive and the negative part, depending on the signal of the main frequency of the flow in the voxel [15].

In order to do that, Fast Fourier Transform (FFT) has to be applied, with a high number of samples required: once again μDoppler is the more appropriate technique.

The mean intensity of the positive and negative part of the spectrum are calculated, resulting in a color-coded directional image (Figure 2.12).
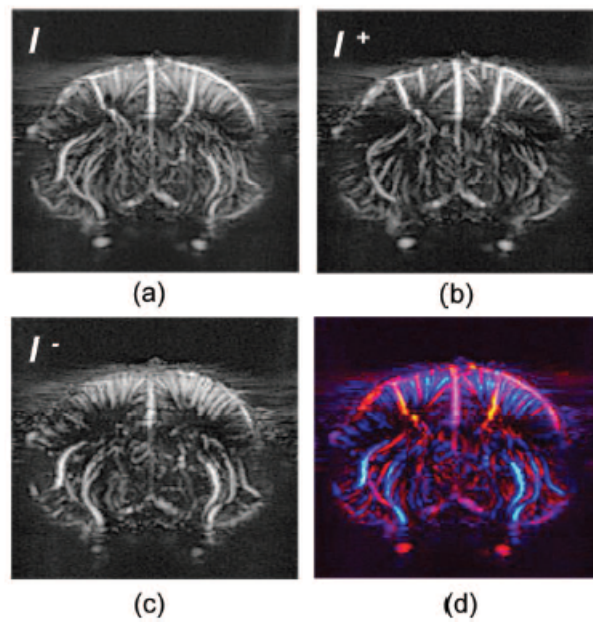
Figure 2.12: In (a) it is shown the original μDoppler image, while in (b) and (c) the mean positive and negative part are calculated. Finally, the directional image is obtained (d), with the venous flow on blue range of intensities and the arterial flow on red range of intensities. (figure taken from [15]).

To conclude, functional ultrasound imaging has great potential because of its characteristics, which are:

- High resolution (lower than 100 μm);

- Large FOV (2 - 4 cm^2);

- Penetration depth up po 20 cm;

The object of the current study is the development of a procedure able to extract useful information from fUS images.

Chapter 3

Materials: fUS Datasets

3.1 Experimental Set-Up

All datasets analysed in the current work have been collected by a team of researchers of the Esposti Lab. The fUS probe used has the following characteristics:

- Resolution: 80 μm;

- FOV: from 1 to 2 cm^2;

- Penetration: scalable, up to 20 cm.

- Frequency of ultrasound wave: 11 MHz

- Sampling Frequency : 1.25 Hz

Images are taken *in vivo* from different rats, anaesthetized with ketamine. Organ of interest (liver or gut) is exposed in the living rat and embedded to grant immobility in agar gel. Once the agar gel is solid, the US probe is placed over the exposed organ. Figure 3.1 and Figure 3.2 depict the experimental set-up from which data are acquired.
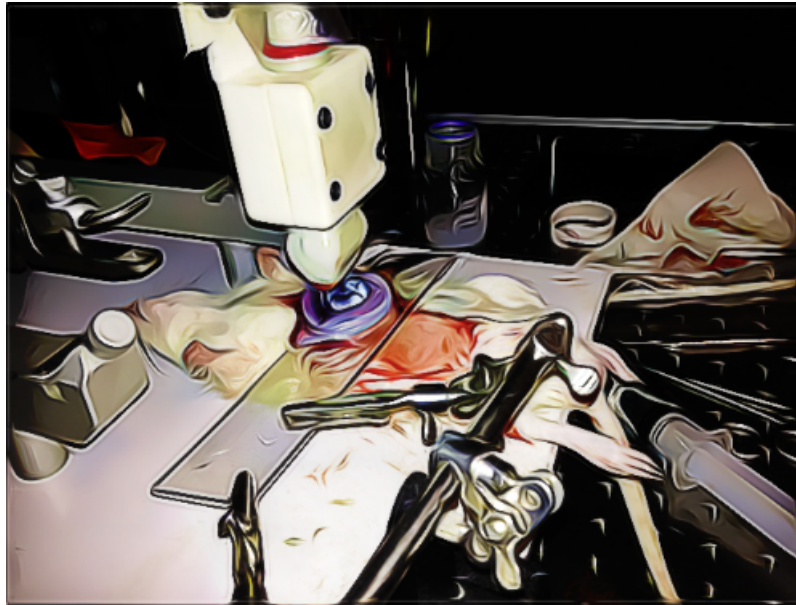
Figure 3.1: Set-up for liver imaging.

Figure 3.2: Set-up for intestine imaging.

3.2 Datasets

All the fUS recordings are transcutaneous, positioning the probe over the organ surface. Intestinal sequences are divided into two main categories depending on the anatomical section considered: transversal or longitudinal.

Liver datasets are listed in Table 3.1, while intestine datasets in Table 3.2.

Table 3.1: Liver Datasets.

Dataset	Acquisition time	Type	Notations
131257	15 min	Transcutaneous	-
171943	4 min	Transcutaneous	Injection in urinary bladder of Nitroglycerin at frame 100
172820	4 min	Transcutaneous	Second consecutive injection of Nitroglycerin at frame 100
182315	10 min	Transcutaneous	Injection of Dobutamine at frame 100
174454	10 min	Transcutaneous	Injection of Nitroglycerin at frame 100
170118	14 mm	Transcutaneous	Dynamic manual spatial scan: 100 slices

Table 3.2: Intestine Datasets.

Dataset	Acquisition time	Type	Notations
153402	3 min 30 sec	Transversal	-
162213	3 min 30 sec	Transversal	-
163144	1 min 46 sec	Transversal	-
165342	3 min 30 sec	Transversal	-
171314	3 min 30 sec	Longitudinal	-
172514	3 min 30 sec	Longitudinal	Stimulation 1mA at frame 100, 5 mA at frame 200 (during 10 frames with 10 ms pulses)
173527	3 min 30 sec	Longitudinal	Stimulation 5 mA at frame 100, 10 mA at frame 200 (during 10 frames with 10 ms pulses)
174212	3 min 30 sec	Longitudinal	Stimulation 1mA at frame 100, 5 mA at frame 200 (during 10 frames with 10 ms pulses)
103259	12 min 30 sec	Transversal	Injection of glucose at frame 300

Chapter 4

Results

The aim of the current work was the development of a set of signal and image processing methods to analyse the information content of fUS recordings.

In order to allow an easier study of data, a graphic user-interface (GUI) has been developed in Matlab, through which different operations on fUS images of the rat liver can be done by the user. Thanks to the creation of the GUI, we automatised the extraction of a number of physiophatological features of the microvasculature of the liver.

All the implemented functions are grouped by operation typology (Figure 4.1) and described by specific buttons - called *Information Buttons* (Figure 4.2).

Images modified by the user can be saved in a defined folder and they can be loaded anytime (with the limit that only one dataset can be visualized and processed at time).
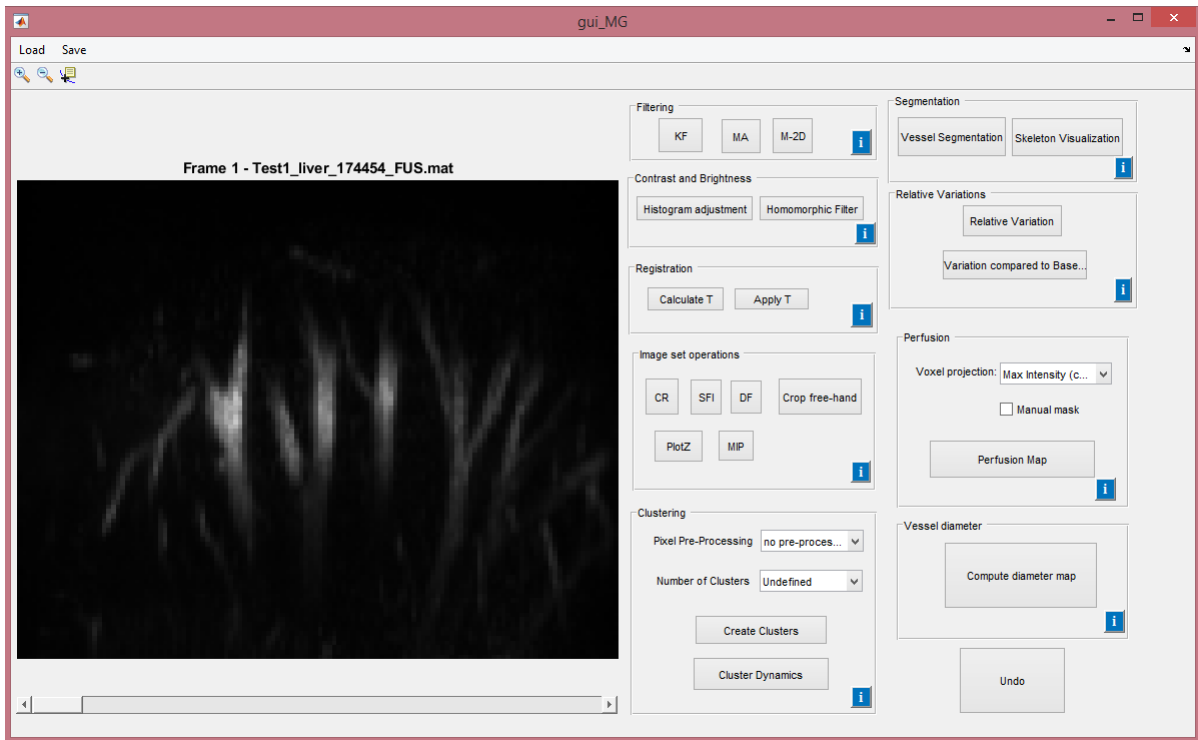
Figure 4.1: Developed GUI: all the frames of the loaded dataset can be visualized and the user can do the desired operation through the corresponding button.
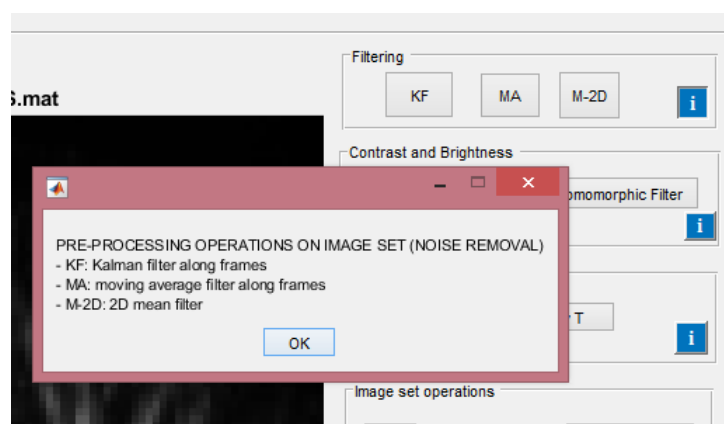
Figure 4.2: GUI detail: for each group of buttons, a Information Button is present in order to explain to the user what is the function of that specific group.

4.1 Pre-processing Procedure Implementation

Ideally, data should be equally spaced in time (i.e., sampling frequency should not change). Each dataset is combined with a vector *time* containing the exact timing of each acquisition and it has been noticed that signals to be analysed are unevenly spaced time series.

The mean time interval between frames is 0.7 seconds for intestine datasets and 0.8 for liver ones, with maximum deviations respectively lower than ±10% and ±5% (Figure 4.3). Interpolation of each pixel signal with sampling time calculated as mean value of difference between consecutive elements of *time* did not affect results, therefore signals have been considered as equally spaced time series with time sample period equal to 0.7 and 0.8 seconds respectively for intestine and liver.
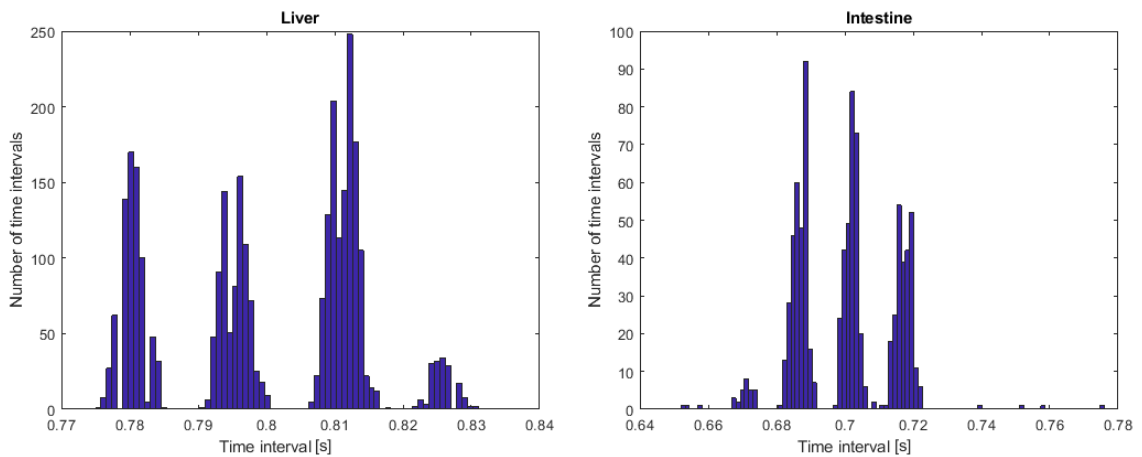
Figure 4.3: Histograms of time intervals between frames of liver (left, measured on dataset 182315, 131117, 140137, total samples 3000) and intestine (right, measured on dataset 165342, 174212, 173527, total samples 900).

As for any other imaging system, after acquisition raw data are characterised by superimposed noise, which has to be removed before doing image and signal processing, otherwise the results are corrupted and falsified.

By looking at the described datasets, noise is easily recognisable. It mainly consists in movement artifacts due to physiological motion of the organ, which is a type of noise usually present in *in vivo* biomedical imaging, and it is visible in all the three dimensions:

1. fast variations of videointensity along z axis (i.e. along a single pixel in time) due to organ movement close to the probe causing an increase of amplitude of the returning echo (Figure 4.4);

47

2. anatomical motion among frames: organ movements on the *x-y* plane cause non-correspondence between pixels and anatomical region on different frames (i.e., a pixel in a given position should represent always the same anatomical part of a structure).
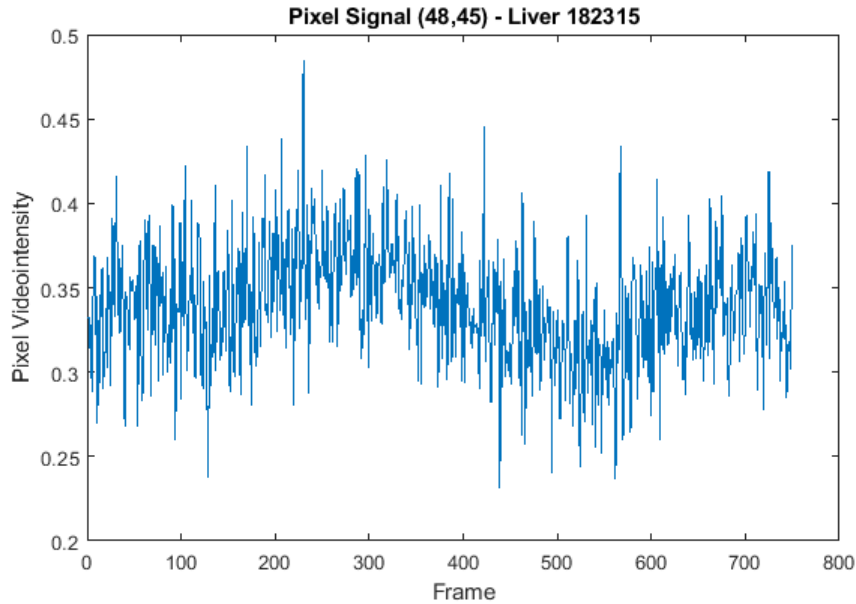
Figure 4.4: Example of noise due to motion along z axis: the fast oscillations are due to organ movements close and far away the ultrasound probe and to electronic and digital noise.

In order to remove this kind of noise, some solutions have been implemented based on filtering operation.

4.1.1 Kalman Filter

The Kalman filter estimates a signal in time by using a feedback control: the filtered signal is a weighted sum of the original signal corrupted by noise and the estimate computed observing past values. Kalman filter is suitable for signals that change in time, because it follows original signal trend by assigning a higher weight to recent measurement with respect to older ones and it is effective with noise that causes sudden unexpected signal variation (e.g.: movement artefacts).

The user can choose the strength of the filter (i.e., the gain): the higher the gain, the more aggressive the filtering operation (Figure 4.5). In other words, with a gain higher than 0.5, the filter weights predicted value more than the observed one.

By applying Kalman filter, artefacts due to motion are reduced: during the dataset visualization, sparkles are less pronounced because of the filter smoothing effect.
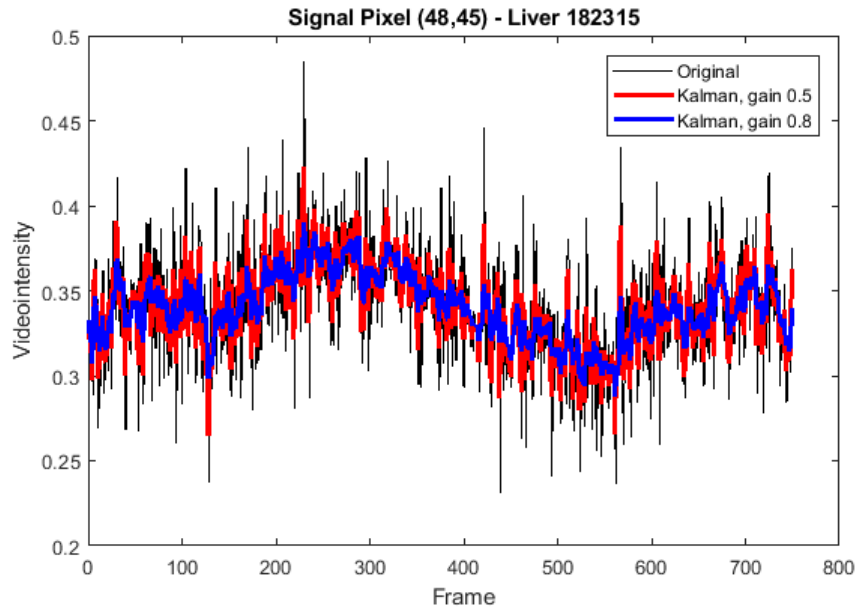
Figure 4.5: Kalman Filter and its effect on pixel signal: black line represents the original signal of the pixel, red line is the signal after having applied to the image Kalman filter with gain 0.5 and blue line is the result of Kalman filtering operation with gain 0.8: the blue signal is the smoothest one because of the higher strength of the filter.

4.1.2 Moving Average Filter

Another kind of filter which can be used to delete oscillations due to organ motion is the moving average (MA) filter. As opposed of Kalman filter, MA filter works directly on pixels signal without any feedback loops.

As the name suggested, this method is based on averaging N values of the same pixel by moving a window along frames on the signal itself. In the implemented filter, consecutive windows overlap, in order to increase continuity between samples. The filter coefficients are all equal in order to give to all the samples the same weight - characteristic of MA filter - and computed from the length of the window L_{window} chosen by the user:

$$coef = \frac{1}{L_{window}} \qquad (4.1)$$

An example of this operation is shown in Figure 4.6. The pixel selected is the same of Figure 4.5 (same dataset), the filter has been applied to the original signal and the length of the window has been changed from 10 to 20.

A more smoothing effect is visible in the second case (green line) because of the higher dimension of the window; indeed, moving average filter acts as a low pass filter, which attenuates all the frequencies higher than the cut-off frequency: the higher is the window size, the lower
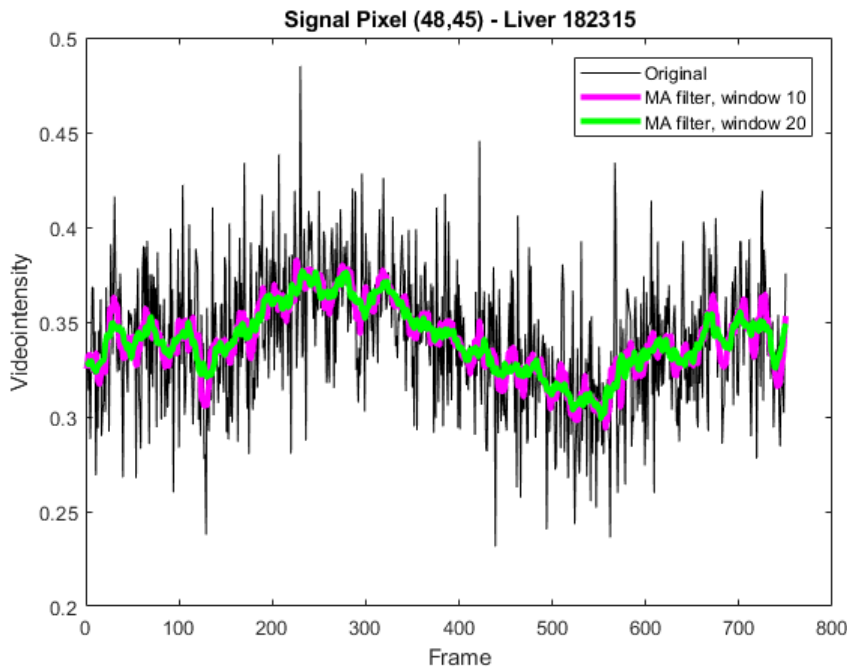
Figure 4.6: Example of MA filter application: pink line is the signal obtained by moving a window of 10 samples, while green line window is made of 20 samples.

is the cut-off frequency, leading to a final signal characterized only by slow dynamics.

For this reason, MA filter can be used to delete fast dynamics given by motion artefacts, but taking into account that also interesting fast dynamics could be left out by the filter: consequently, a too high window size is not recommended.

Cut-off frequency can be calculated as the frequency where filter magnitude is -3 dB, which corresponds to the point at which amplitude is reduced of 30% with respect to original signal. Filter responses with different window sizes are shown in Figure 4.7, highlighting the shrinking of the pass band with the increase of window length.

The main difference between these two described filters is the weight assigned to measurements: as mentioned above, MA filter is characterized by all equal weights, while Kalman filter gives higher weight to recent measurements.

Of course, a correct use of both filters depends on an experience and data-driven choice of window length in MA filter (Figure 4.8) and gain in Kalman filter (Figure 4.9).
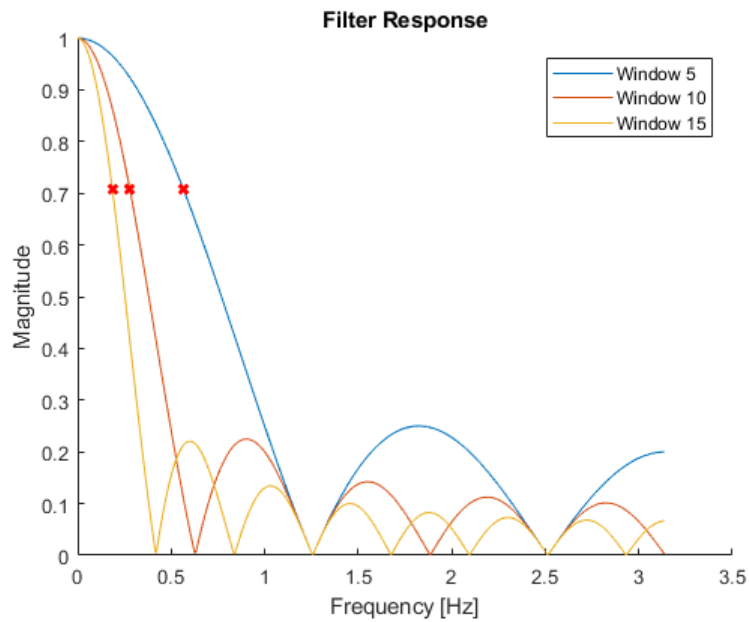
Figure 4.7: Moving Average filter response for window size 5, 10, 15: the red points indicate the cut-off frequency (x axis).
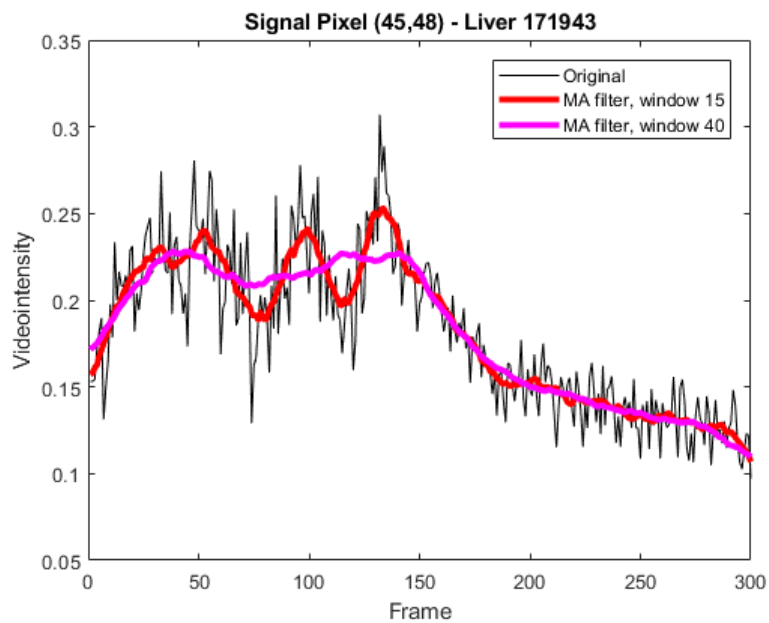
Figure 4.8: Moving Average filter applied with different window sizes: 15 (red line) and 40 (pink line). The former choice is a good compromise between smoothing effect and noise removal, while in the latter case the signal dynamics is lost.
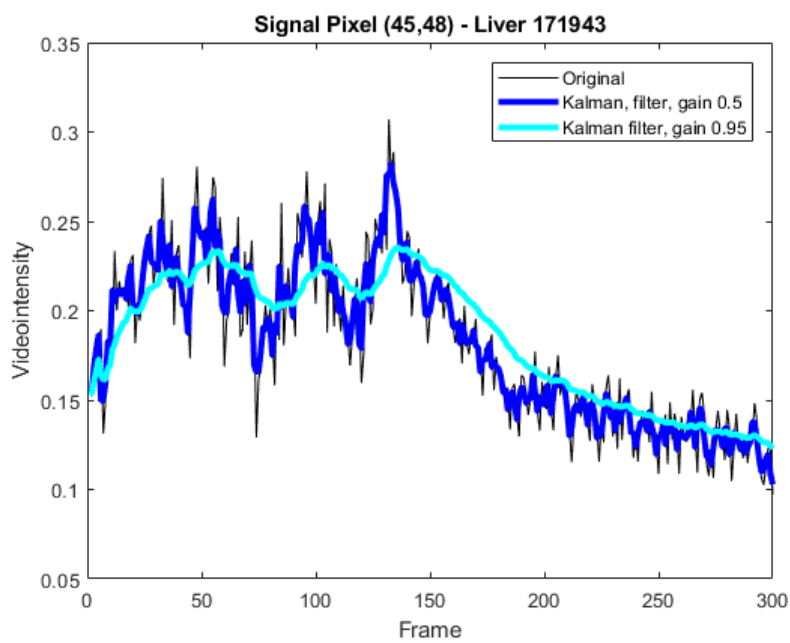
Figure 4.9: Kalman filter application: blue line is referred to filter gain 0.5, light blue to filter gain 0.95. In the second case filtered signal does not follow properly the original one.

4.1.3   Registration

In biomedical imaging, registration is the process of aligning image dataset representing the same structure of interest acquired in a subject at different times or with different modalities, in order to map each point in one image into the corresponding point in the other image. Registration is therefore required if the structure is moving, but it is not a simple task, especially when working with noisy biological images. If motion is visible on dataset and registration is not performed, analysis along frames of pixel signal is not reliable anymore, because a single pixel does not represent exactly the same anatomical point of the structure along frames (e.g., a vessel pixel moves on background creating discontinuity in temporal signal). On the other hand, if movement is due to organ shape modification (for example, organ shrinkage or relaxation), registration could cause some problems by trying to align images which represent the same thing, but with different shape.

In the current fUS imaging procedure we developed, registration process is divided into two parts: transformation matrix T calculation and application of it to dataset.

It has been decided to split them into two different operations (Figure 4.10) in order to allow the user to calculate the matrix not directly on the dataset to be registered, but to a modified one.
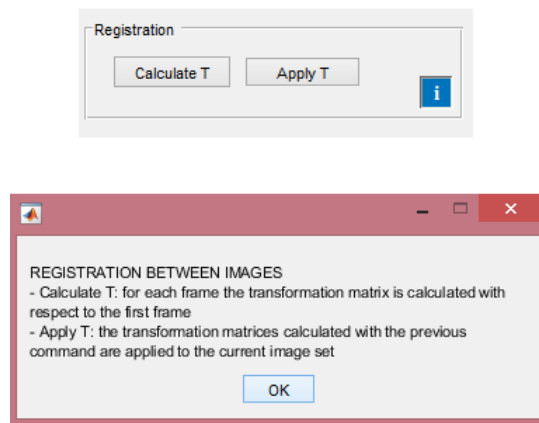

Figure 4.10: GUI detail: registration process buttons with information on their function.

This separation can be very useful when images are corrupted by noise which would cause problem in the process of calculation of the more suitable matrix T, because registration process is performed based on pixel intensity-value: indeed, continuous changes in the videointensity values of pixels do not allow good registration process. An example of registration schema followed with μDoppler dataset is shown in Figure 4.11.
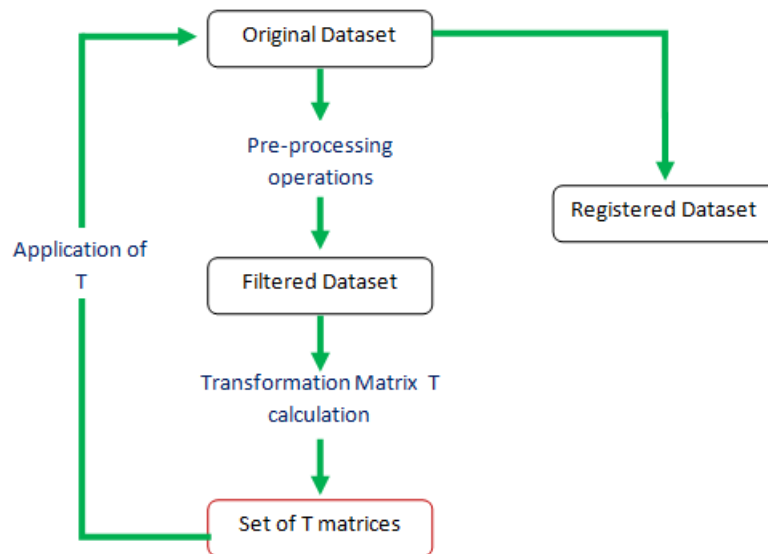
Figure 4.11: Registration process workflow: the user can choose how to filter data and to which dataset apply matrices T.

Calculation of matrix T and registration are performed on each frame with respect to the first frame. Therefore, correlation between i^{th} frame and the first one of dataset can be computed to verify if registration has been done in a worthwhile way.

For example, Figure 4.12 shows correlation along frames in the original dataset (red line) and in the registered dataset (blue line). Matrices T have been calculated on filtered dataset - Kalman filter applied with gain 0.6 and moving average applied with window size 5 - and then they have been applied to original dataset: correlation is high in both cases (liver is moving of few pixels, movements are small), but in the second case correlation is increased. The type of transformation is chosen by the user - translation, rigid, affine - depending on the movements: considering analysed datasets, the best one is the rigid transformation, since movements are mainly of rotation and translation on $x - y$ plane. The affine transformation works well too, including also shearing, which is almost null in the current images, so the final result is equal to the rigid transformation, with a higher calculation time: consequently, it is preferable to use rigid transformation.

Computational time for registration process is high (around 4 minutes, depending on the number of dataset frames and on the computational power of device), because of the high number of matrices to be computed: this fact makes this method inappropriate for real-time analysis.
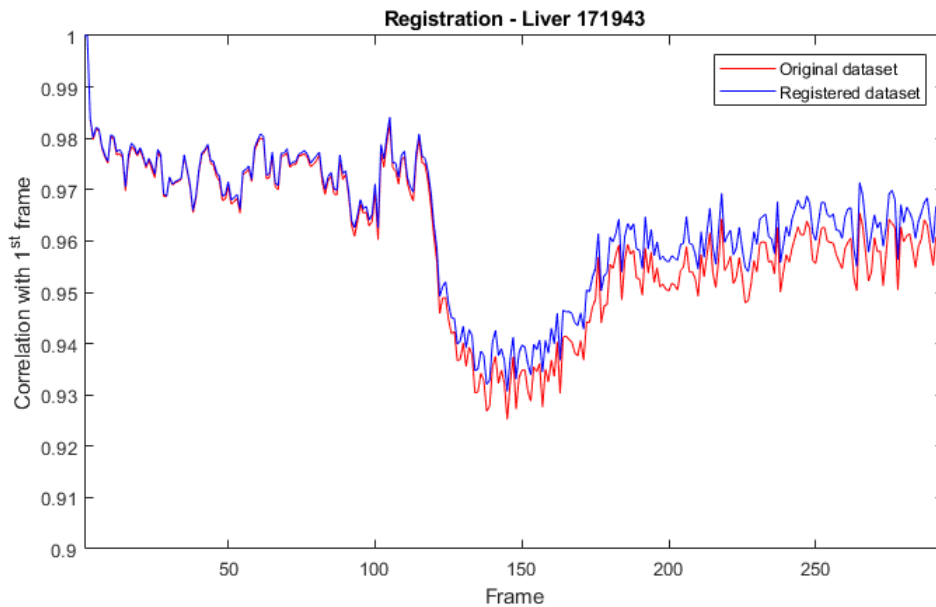
Figure 4.12: Comparison of correlation values between original dataset and registered dataset.

4.1.4 Dataset Operations

This button group has been implemented after a first preliminary analysis on datasets. With the following commands, it is possible to clean dataset from little impurities which could lead to undesired effects in the processing phase.

Currently, these functions are available:

- Crop: it executes a rectangular crop on the entire dataset, particularly useful if a physical disturbance object is present (Figure 4.13);

- Crop free-hand: crop manually designed by the user applied to all frames;

- Plot Z-axis: by selecting an arbitrary number of pixels on the image, their trend along frames is plotted (i.e., pixel videointesity), allowing for example the user to see if there are some anomalies (Figure 4.14);

- Delete Frame: it enables the elimination of one or more frames (Figure 4.14);

- Set Frame Interval: the user selects a frame interval; this operation is useful for analyse only frames of interest reducing computational time required for each successive operation;

- Maximum Intensity Projection (MIP): it creates a new image by selecting the maximum value for each pixel along a certain number of frames - selected by the user - giving as output maximum intensity projection.
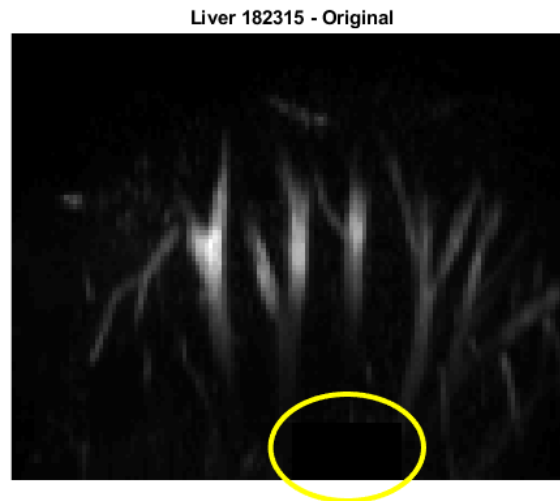
Figure 4.13: In the yellow circle is visible a geometric shape which is not part of liver structure: with the crop function it can be deleted.
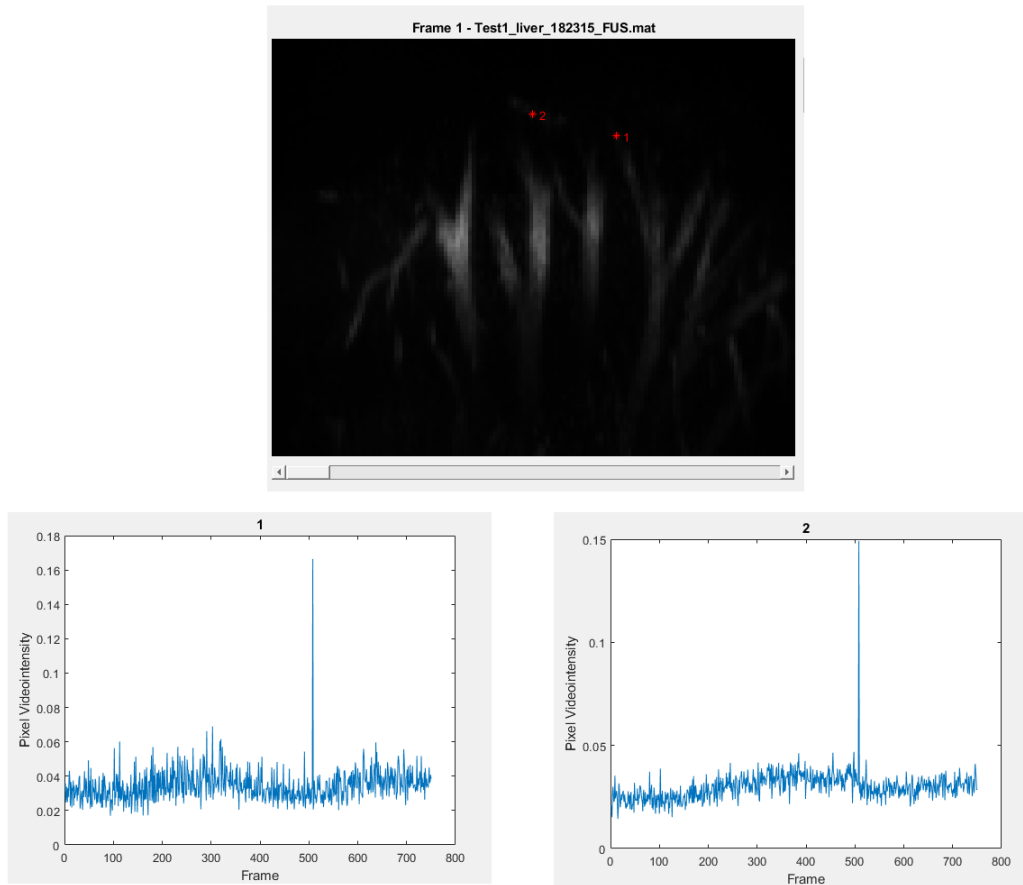
Figure 4.14: Example of Plot Z-axis function: the user has selected two pixels (highlighting with red stars) and their videointensity along all frames is plotted in separated figures. As can be seen from their trend, there is a peak at frame 508 which is probably due to liver movement: this frame can be deleted with the button Delete Frame.

57

4.1.5 Contrast and Brightness Enhancement

Finally, to better visualize structures of interest, two operations can be executed on image set: histogram adjustment and homomorphic filtering.

The former is performed by automatically calculating, for each frame, two levels, respectively low and high videointensity value, and from them adjusting the histogram: pixel values are then remapped within low and high level, saturating to 0 values under the inferior level and to 1 values upper the superior level. Type of function for remapping process is chosen by the user who specifies γ parameter (Figure 4.15).
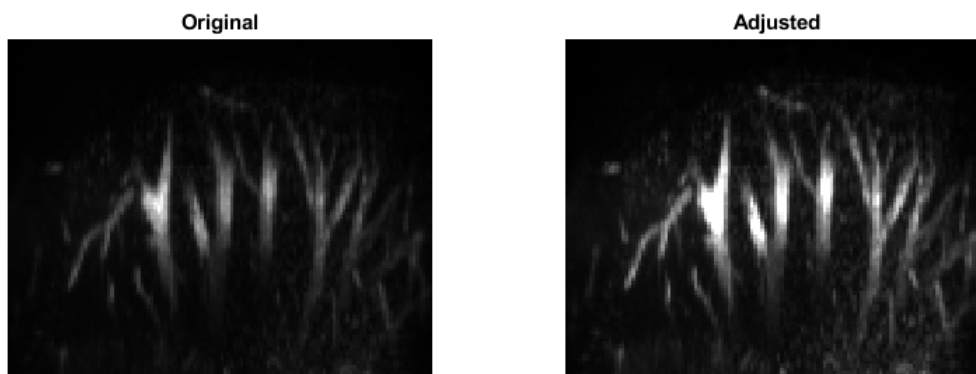
Figure 4.15: Example of histogram adjustment: original image (left) and adjusted image (right). The adjusted image better shows vessels of interest with a higher videointensity with respect to the background.

The latter function is a specific filter designed to delete variable brightness values on image plane with the assumption that it is low frequencies noise. Image $f(x, y)$ is formed by two distinct components: illumination $I(x, y)$, described by slow spatial variations - low frequencies - and reflectance $R(x, y)$, characterized by fast changes - high frequencies.

The aim of homomorphic filter is enhancement of reflectance component (i.e., objects of interest) and suppression of illumination one (i.e., low frequencies associated with noise).

To perform homomorphic filter specific operations are required. Because of the non linearity of noise a logarithmic transformation is needed, through which components that are originally multiplied are transformed into added component:

$$log(f(x, y)) = log(I(x, y) \times R(x, y)) = log(I(x, y)) + log(R(x, y)) \tag{4.2}$$

After this step, the filter can be applied in the frequency domain and it acts as a linear filter.

A schema of homomorphic filtering is shown in Figure 4.16, while its frequency response is visible in Figure 4.17:

$f(x, y) \Rightarrow \boxed{\ln} \Rightarrow \boxed{\text{DFT}} \Rightarrow \boxed{H(u, v)} \Rightarrow \boxed{(\text{DFT})^{-1}} \Rightarrow \boxed{\exp} \Rightarrow g(x, y)$
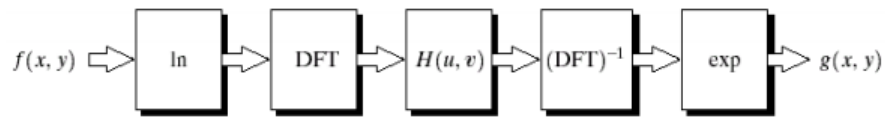
Figure 4.16: Block diagram of homomorphic filter: after logarithmic transformation, the Fourier transform of image is multiplied with filter in frequency domain. To obtain the final image, inverse Fourier transform is applied to filtered image, followed by inverse logarithmic transformation.
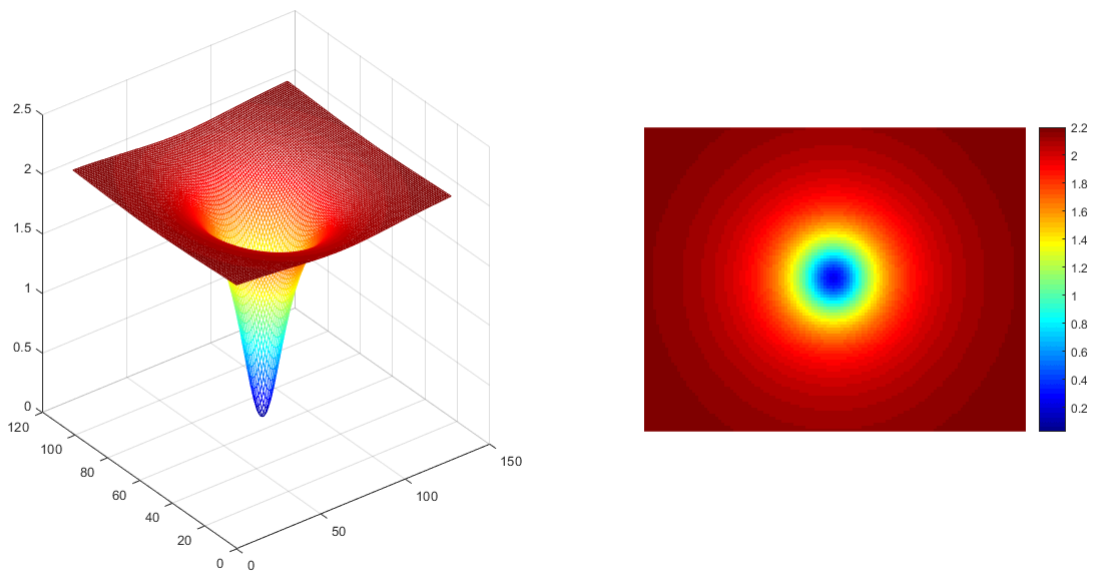
Figure 4.17: Spectrum of the implemented homomorphic filter: 3D (left) and 2D (right) visualitazion.

After severals trials, the best option to visualize vessels inside datasets with a good contrast is the following:

1. noise removal with Kalman Filter and, if necessary, application of moving average filter too;

2. homomorphic filtering;

3. histogram adjustment.

The use of homomorphic filter before histogram adjustment is preferable because it compresses image dynamics and it increases contrast. Histogram adjustment without homomor-

phic filtering does not delete the multiplicative noise between vessels, visible in Figure 4.18.
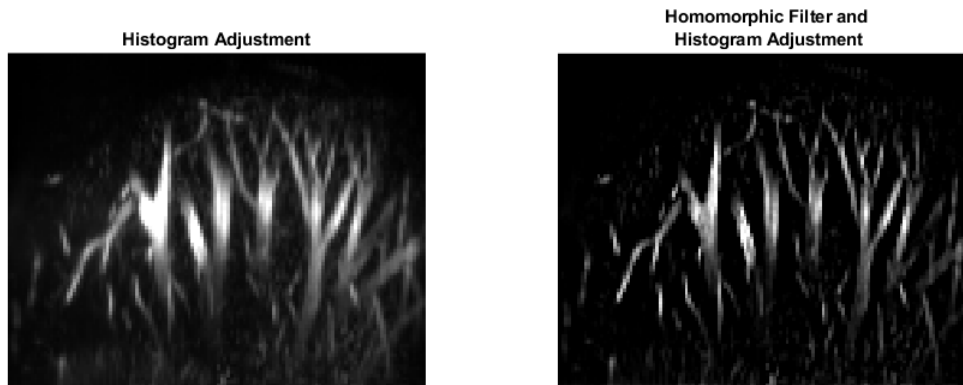
Figure 4.18: Importance of homomorphic filtering: left image is obtained just by adjusting the histogram, right image is the result of homomorphic filter and then histogram adjustment. In the right image vessels are more in contrast with respect to the background than in the left image.

4.2 Processing Phase

After images have been cleaned from noise and structures of interest have been recognised, dataset can be processed and analysed.

4.2.1 Parameters Calculation

In order to provide an informative tool to physicians, one of the main goals of fUS imaging is to allow clinical evaluations through some standard parameters which can be extracted from image sequences. The parameters considered herein are perfusion maps and vessels diameter automatised extraction.

4.2.1.1 Perfusion Maps

Perfusion Maps have been developed in order to help the user to visualize which zones are more perfused in images, allowing comparison between different vessels.
Basically, a dataset map is built following these steps:

1. Dataset is divided into voxels, user selects voxel size - height H, width W, thickness T;

2. Possibility of selecting a manual region of interest (ROI) on the entire dataset is given: if the user selects this option, he draws directly the ROI on the image;

3. Selection of the perfusion map type between *Mean Intensity Map*, *Max Intensity Map* (explained below)

4. Map visualization

The map so obtained has a smaller number of frames than the original dataset, depending on chosen voxel thickness. Consequently, visualization is quicker and it is easier to visually capture perfusion variations in time, because of the augmented time interval between two consecutive frames (e.g., time interval between frames in original dataset is 0.8 seconds, for a voxel thickness equal to 5, time between map frames is 4 seconds).

Maps Types   Methods for generating perfusion map are two: *Mean Intensity Map*, *Max Intensity Map*.
The *Mean Intensity Map* algorithm calculates for each pixel its mean videointensity value along all voxel thickness, obtaining a matrix of dimension [HxW]; then, as final value of single voxel, the maximum value of the matrix is taken (Figure 4.19).

For *Max Intensity Map*, the process is different: instead of mean value, for each pixel is considered its maximum value along voxel third dimension, with a partial result of a matrix [HxW] again. Then, new image set is converted into binary image set and, for each voxel, number of white pixel (i.e., pixels equal to 1) is counted (e.g., if $H = 3$ and $W = 3$, maximum possible voxel value is 9). Finally, the images are divided by voxel area, to normalize perfusion values between 0 and 1 (Figure 4.20).

Figure 4.19: Example of perfusion map obtained with Mean Intensity Map algorithm - voxel dimension 3x3x5. Left map is taken from baseline frame, right map just after Nitroglycerin injection: the second image shows a higher perfusion. Both map are created after the manual selection of a ROI. Anatomical structures are not well defined because of the high dimension of the voxels.

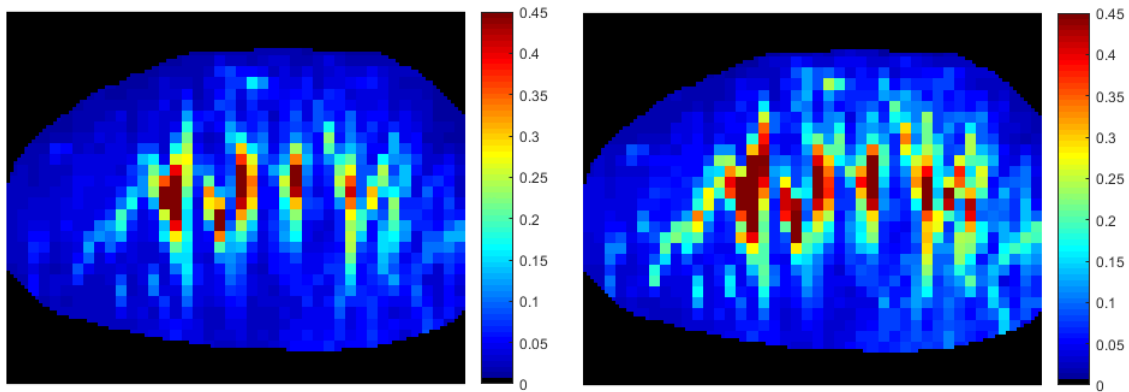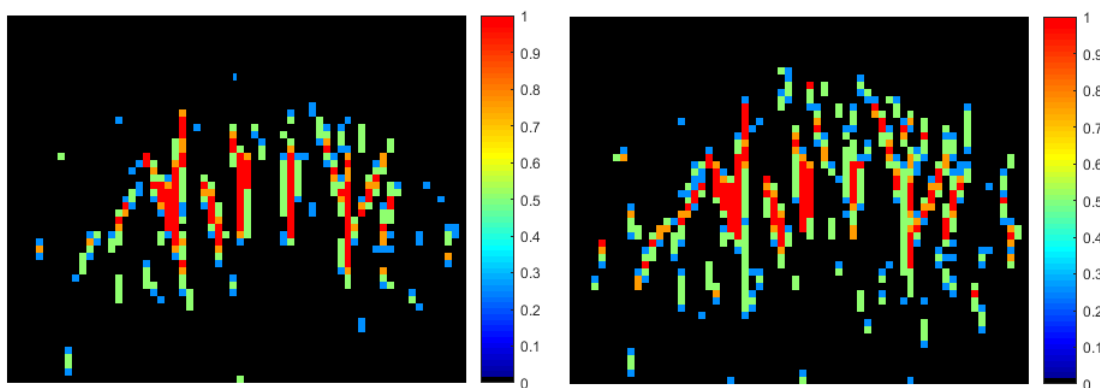*Figure 4.20: Example of perfusion map obtained with Max Intensity Map algorithm - voxel dimension 2x2x4. Left map is taken from baseline frame, right map just after Nitroglycerin injection: small vessels are visible in the second image. In this case anatomical structures are defined more clearly because the voxel dimensions are smaller.*

4.2.1.2   Vessel Diameter Calculation

An algorithm for vessels diameter computation has been implemented and the corresponding button is present in the GUI. The aim of the developed method is the automatic diameter calculation, starting from black and white image of vascular tree. As already mentioned in 2.2, software such as CapImage are able to compute vessel diameter on OPS images. The algorithm herein described has been written to fit binary images from fUS imaging system. The development has been performed on a phantom image specially designed (Figure 4.21).
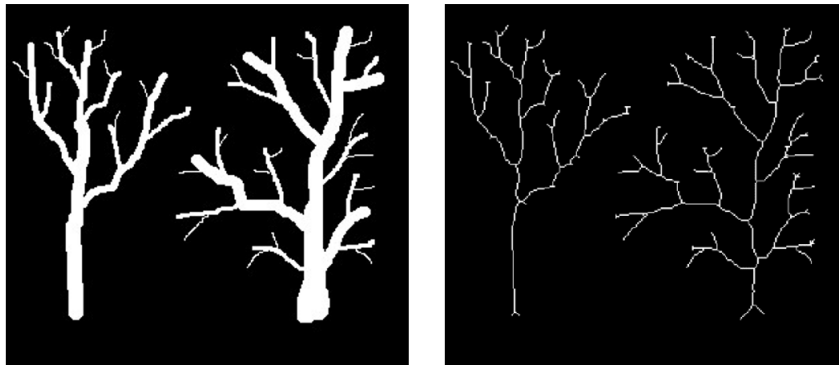
Figure 4.21: Phantom designed for algorithm implementation (left) and its skeleton (right).

The algorithm works as follow:

1. Skeleton of the binary image is computed, resulting in an image similar to Figure 4.21 (right);

2. All the intersection points in the skeleton are extracted, then every single branch is divided into separated objects;

3. One by one, these elements are isolated and taken apart into sub-elements (each of them with a axis length of 5 pixels), as shown in Figure 4.22;

Figure 4.22: Object of a branch (left) and its decomposition into sub-elements (right).

4. Diameter is computed for each sub-element, by calculating the width. The final diameter of the entire segment is obtained as the average value of all its sub-elements diameters: this way of proceeding makes the algorithm more robust especially when dealing with curve segments;

5. Once the average diameter is known, the tree is recompose by summing up all the single elements. Before putting back together segments, they are multiplied by their diameter value (i.e., a binary element composed by pixels equal to 1 is multiplied by its diameter D, resulting in an element made of pixels with value D);

6. At this point the binary image has been transformed into a two-dimensional map in which each pixel value reflects the diameter of the segment that contains it.

The algorithm applied to phantom of Figure 4.21 gives the map depicted in Figure 4.23.
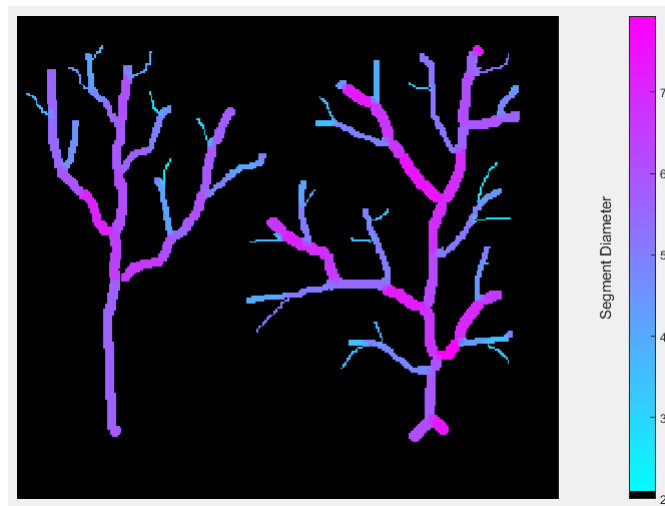
Figure 4.23: Diameter Map for the designed phantom (colorbar is expressed in pixel here).

Main issues of this method are:

- Curve elements: they result in a slightly higher diameter than the real one;

- Terminal part of branches: the vessel is divided into two tails which are not present in original image or may not have a correct value;

- Timing: time needed to compute a single frame map is of the order of 10^{-1} seconds, while time interval between each frame is on average equal to 0.7 seconds.

This algorithm can obviously be applied to real fUS binary images. A correct pre-processing

is mandatory in order to obtain an image which is moderately affected by noise such the one in Figure 4.24. Its diameter map is shown in Figure 4.25.
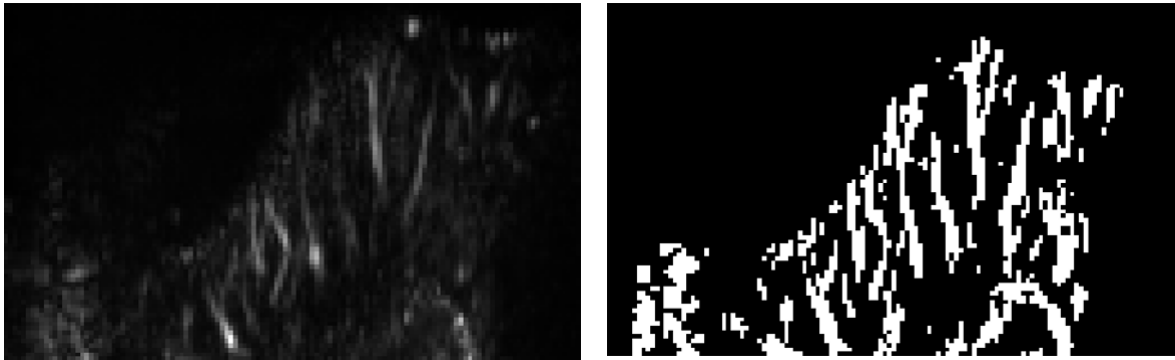
Figure 4.24: Example of original liver image (left) and the corresponding binary image (right).
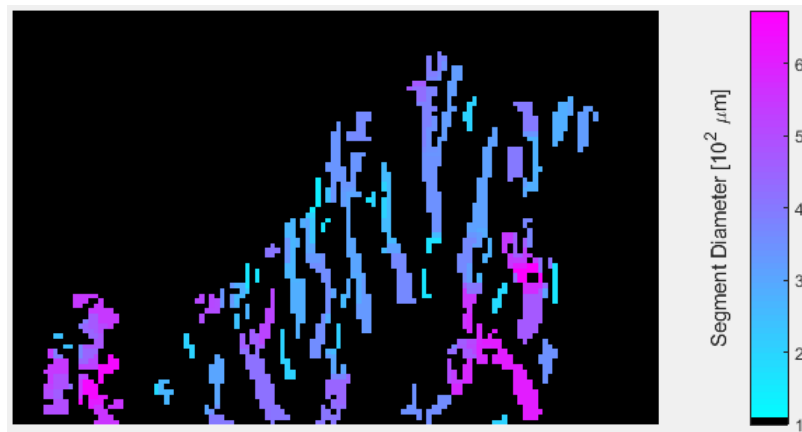
Figure 4.25: Diameter Map for liver image of Figure 4.24.

Figure 4.26 shows diameter map for Nitroglycerin (NG) before and after drug injection. Small vessels are visible in the map after the injection, while before NG injection they are not (i.e., in the binary images they are not marked with 1 because of the low videointensity compared to big vessels). It can be noticed that the diameter of big vessels increase, probably due to vasodilation caused by NG, effect which will be explained in next sections (the diameter increment is just around 1 pixel, but it corresponds to 100 μm).
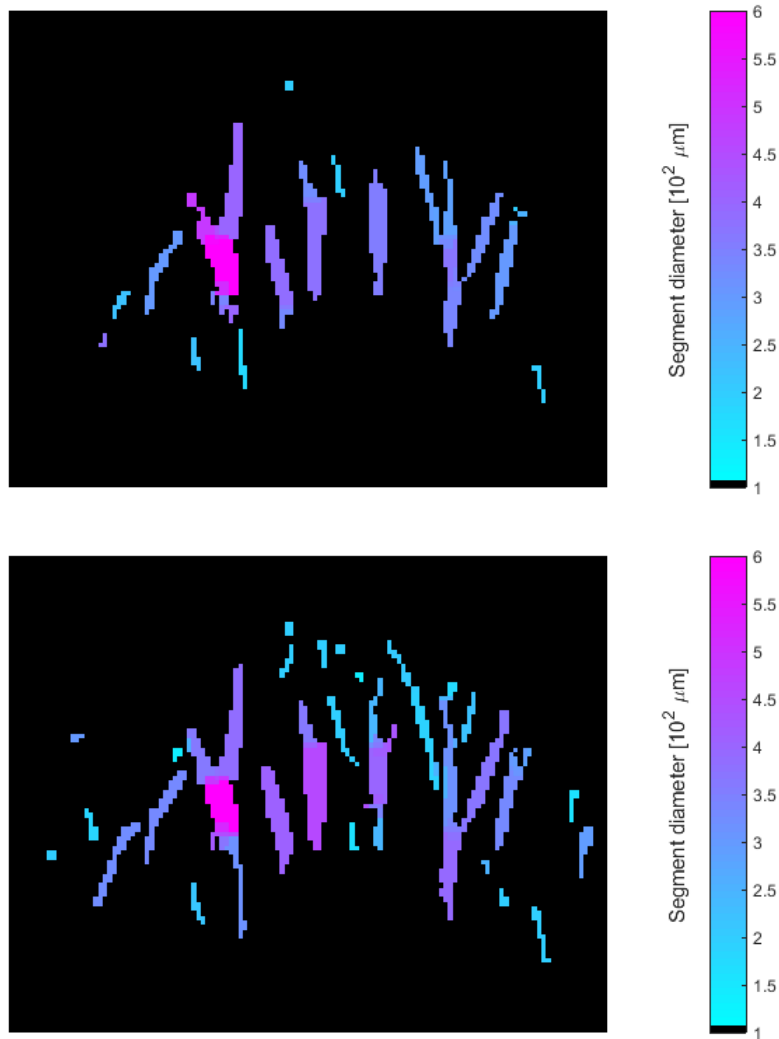
Figure 4.26: Diameter Map of the liver before (left) and after (right) NG injection.

4.2.2 Variation Images Calculation

As mentioned in 2.3.2, pixel signal is proportional to blood flow rate: therefore, it has been decided to compute images of variation from a chosen baseline to better investigate the effect of drugs on microvasculature. From now on these type of images will be called *Variation images.*

Procedure to compute them is the following (all included in a GUI button):

1. User selects an arbitrary baseline frames number;

2. Mean baseline image $baseline_{mean}$ is calculated as the mean of pixel values of baseline frames just selected along the third axis ($z\ axis$);

3. Variation images are obtained as relative variation with respect to mean baseline image:

$$VariationImage\,(i) = \frac{frame\,(i) - baseline_{mean}}{baseline_{mean}} \tag{4.3}$$

Variation images so computed exhibit changes with respect to baseline values independently on intensity values: it does not matter if signal is small or high in amplitude, if significant deviation from baseline occurs, a noticeable relative variation will be present. Therefore, they are particularly useful in case of drug injection, in order to study its effect on the organ.

4.2.2.1 T-Test Mask generation

In order to analyse only the pixels with a variation higher than a set threshold, generation of a binary mask is required, for example to switch off background pixels.

The implemented mask is basically a T-test working in the following way:

1. Selection of frames where pixel signals are visually different from baseline signals;

2. Calculation of *VariationImage* for these frames of interest using (4.3), called Var_{HIGH};

3. Calculation of *VariationImage* for baseline frames using (4.3): called Var_{BASE};

4. Calculation of standard deviation σ for each pixel along frames from Var_{BASE} images;

5. Mask creation: a pixel (i, j) is masked with 1 if

$$max\{Var_{HIGH}(i, j, :)\} > 3\sigma \tag{4.4}$$

In other words, a pixel is marked with 1 if its maximum variation value with respect to baseline is higher than 3 times its standard deviation calculated on baseline frames.

By using condition 4.4, only pixels which are characterized by positive variations are masked with 1 (i.e., pixels with a higher signals after baseline frames). It is possible also to include pixels with a negative variations, simply considering the absolute value of the maximum variation value.

4.2.3 Drugs Effect: Nytroglicerin and Dobutamine

4.2.3.1 Qualitative Comparison

VariationImages are particularly useful to study datasets which are characterized by the use of specific drugs, in order to qualitatively visualize if a change in microvascular perfusion is present: indeed, they allow to observe the effect caused by given drug.

Drugs used in the available datasets are Dobutamine (DB) and Nitroglycerin (NG). Their effect on cardiovascular system is known - DB is a cardiac stimulant [44], NG is mainly a vasodilator ([45], [46]) -, but their action on microcirculation has never been investigated.

A qualitative assessment can be done calculating *VariationImages* for dataset with DB injection and NG injection and observing along frames how images change (i.e., if microvascular structures are more or less visible along frames).

Figure 4.27 and Figure 4.28 provide a qualitative investigation about the effect of the drugs: first figure is taken from NG, while the second one from DB. By looking at them, these two drugs seem to act differently: NG causes vasodilation, leading to a better visualization of microvascular branches because of the augmented amount of blood flowing within, while in DB image vessels are not clearly shown. In this last figure, it should be noted that even if vessels are not distinguishable, there is an area with a relative increase compared to baseline higher than 90%. This phenomenon suggests that DB increases blood flow: DB could cause extravasation, which would explain the lack of differentiability between microvessels and surrounding tissue.

In both images, pixels with a negative relative variation are saturated to black color, while pixels with a positive variation higher than 100% to red.
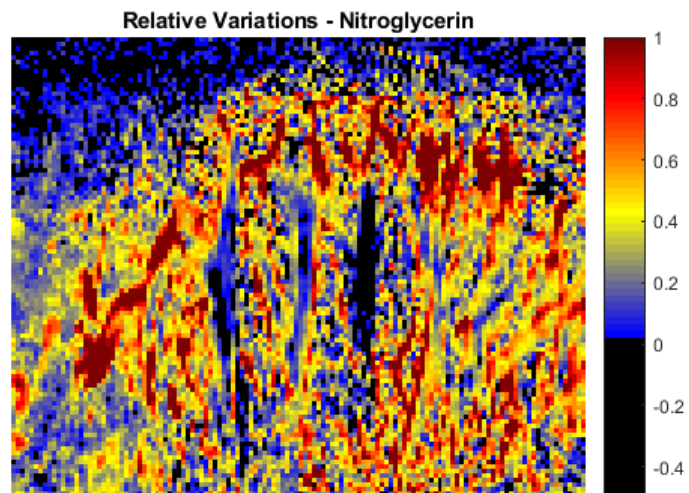
Figure 4.27: Nitroglycerin Variation Image (frame 150, injection at frame 100), image is color-coded according to the percentage change in pixel signal with respect to baseline.
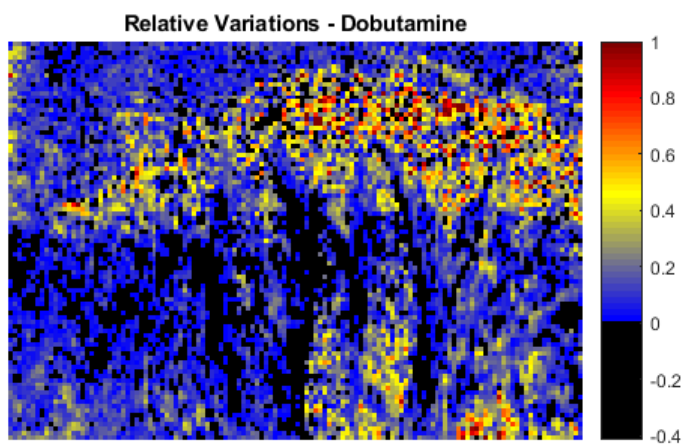
Figure 4.28: Dobutamine Variation Image (frame 670, injection at frame 100), image is color-coded according to the percentage change in pixel signal with respect to baseline.

Big vessels in figure 4.27 and 4.28 are colored in black, meaning that signals inside them are lower after drug administration.

It is important to note that selected frames in the two images are not the same: frames with a high relative variation have been chosen. After injection at frame 100, NG effect is well visible after few frames, while for DB effect the response is slower, therefore it has been shown frame 670. This fact suggests that DB provokes a less prompt increase of blood flow than NG.

By calculating the image difference between baseline frames and drug-effect frames (i.e., chosen interval of frames after drug injection), it is possible to find out the magnitude of pixels change (Figure 4.29 and 4.30), instead of their percentage change.

The colormap used for these images is the same in order to allow a better comparison between them. As can be easily seen, in NG image pixels belonging to vessels are almost all saturated to maximum value, meaning that signals increase a lot (percentage variation of Figure 4.27 around 200%), while in DB image pixels values are lower: the increase caused by NG is sharper than the one of DB.
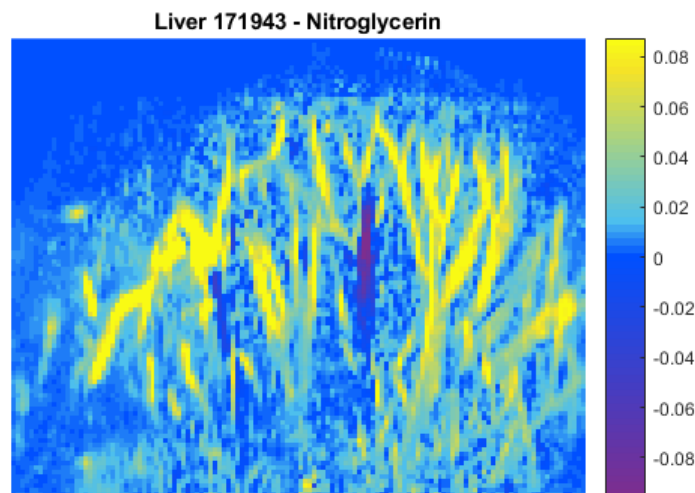
Figure 4.29: Nitroglycerin Difference Image.
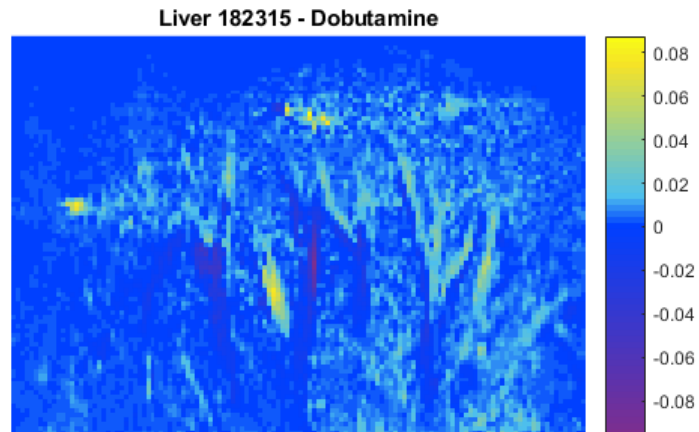
Figure 4.30: Dobutamine Difference Image.

4.2.3.2 Quantitative Comparison

In order to better described effect of Nitroglycerin and Dobutamine, the relative variation trend of the area of interest - the parenchyma - can be plotted over time.

The number of frames of NG dataset is 294 (6 frames have been deleted because of noise presence), while frames of DB dataset are 748 (with 2 frames cut off): comparison can be done between the two drugs but knowing that after 294 frames NG information is not available.

Trends of percentage variation compared to baseline are displayed in Figure 4.31: NG effect is promptly visible after drug injection - frame 100 -, instead DB effect is less evident in frames following injection, but it increases in time continuously.
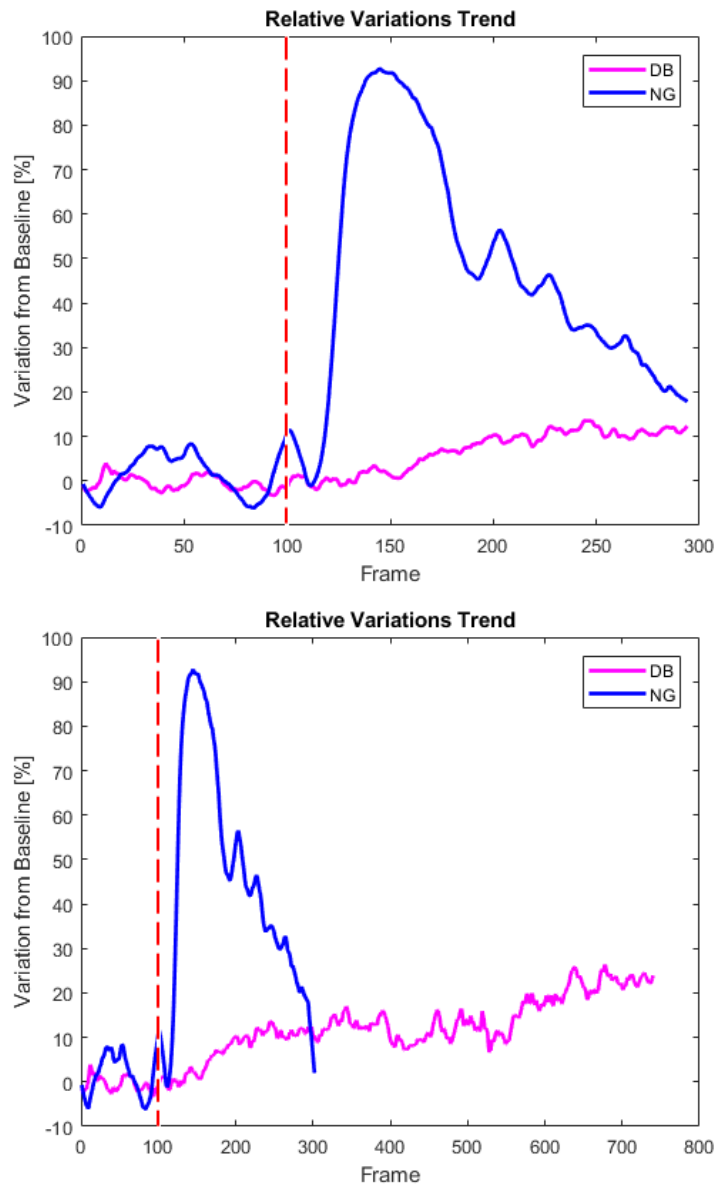
Figure 4.31: Trend of percentage variation with respect to baseline of NG (blue line) and DB (pink line), considering frame number of NG dataset (top) and frame number of DB dataset (bottom). Red line indicates the time of drug injection.

4.2.3.3 Liver Skeletonization

In order to further characterize microvasculature response to DB and NG, we used skele-
tonization (i.e., skeletons of the image structure are computed).

The main idea is the following:

- NG causes vasodilation: vessels are well visible in frames after injection (Figure 4.27) and therefore the skeleton dimension of the structure should increase;

- DB causes extravasation: an area where blood flow increases is present, but the microvascular branches are not noticeable, consequently skeleton should not grow (even if the relative variation percentage increases) because blood exiting vessels prevents detection of microvascular structures.

Skeletons are computed from binary images, which are obtained through a Matlab algorithm that locally adapts threshold gray-level, an example of them is visible in Figure 4.32. Figure 4.33 shows the trend of skeletons dimension: as expected, skeleton of NG dataset follows the shape of relative variation signal of Figure 4.31, while skeleton related to DB dataset is almost the same along frames.

This result confirms the hypothesis made on NG and DB effect.

Figure 4.32: Example of NG image skeletons: left skeleton is taken from a baseline frame, while right one from a frame after NG injection.

Figure 4.33: Skeleton Dimension along frames for Nitroglycerin (top) and Dobutamine (bottom).

4.2.4 Clustering

The aim of this section of the processing procedure is the analysis of foreseen datasets in order to extract useful information about physiological and altered - under effect of different drugs - functioning of the organ.
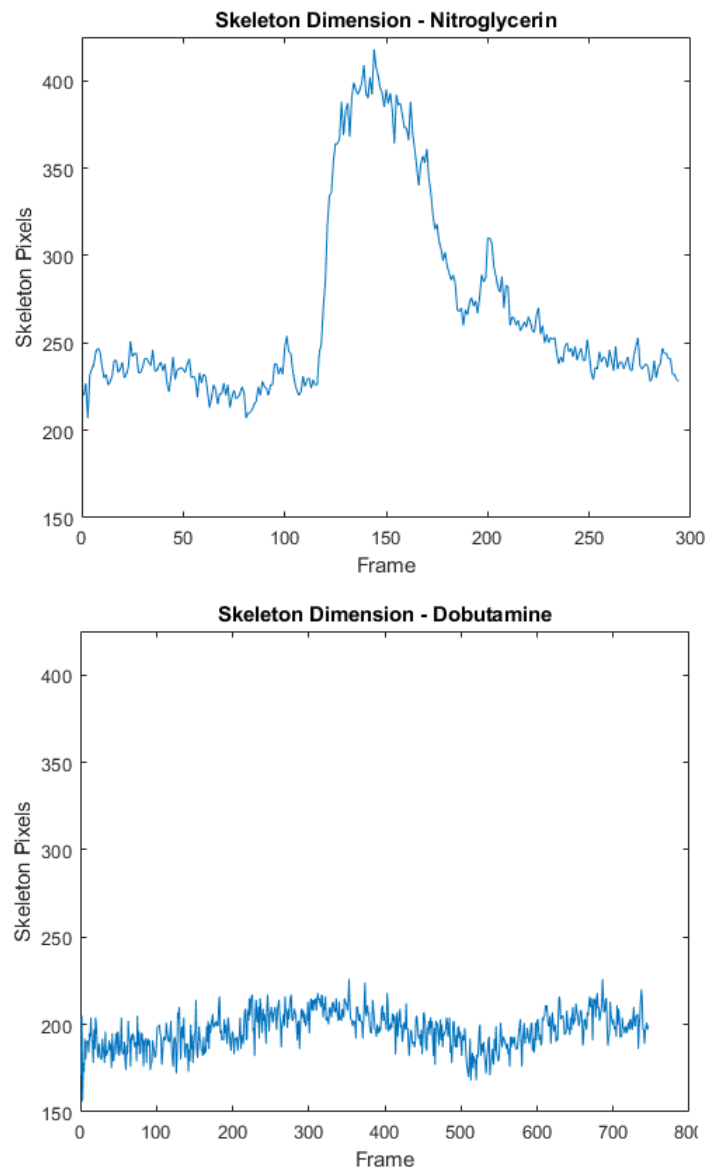
Images data are unlabelled, without any sort of informative element (e.g., vessel type of a certain pixel). The machine learning branch that deals with this class of problems is the unsupervised learning which encompasses clustering.

Clustering is one of the most important unsupervised learning method: it deals with finding a structure in a collection of unlabelled data and identifying homogeneous groups of records called clusters. A cluster is therefore a collection of objects which are similar between them and dissimilar to objects belonging to other clusters.

This method requires the definition of a measure of similarity, usually the Euclidean distance is used for numerical data:

$$d(\mathbf{q}, \mathbf{p}) = \sqrt{(q_1 - p_1)^2 + (q_2 - p_2)^2 + ... + (q_n - p_n)^2} = \sqrt{\sum_{i=1}^{n}(q_i - p_i)^2} \qquad (4.5)$$

where $\mathbf{q}$ and $\mathbf{p}$ are two observations.

4.2.4.1 K-Means Clustering

K-means method is among the most widespread unsupervised learning algorithms: given a certain number of clusters fixed a-priori, it defines k centroids corresponding to the k different clusters. Firstly, each centroid is placed far away from the other, then each element of the dataset is associated to the nearest centroid (in term of Euclidean distance). After this initial step, centroids of new clusters are re-calculated and elements are re-assigned to the new nearest centroid: this step is repeated until points do not change cluster anymore and centroids remain fixed.

Final purpose of the algorithm is to minimize, for each element, its distance from cluster centroid. An important aspect of k-means clustering is that all clusters are mutually exclusive (i.e., an element belonging to cluster A cannot be found in any other cluster).

As mentioned above, K-means requires the a-priori definition of clusters number, in the GUI the user can choose between two options:

1. Selection of number k of clusters: fast and suitable for real-time application, but it requires a-priori user knowledge on data types to define a satisfactory cluster number;

2. Number of cluster automatically selected using *elbow* method [47] which determines the optimal number of clusters. The *elbow* method computes the percentage of variance explained as function of cluster number and it chooses as most convenient clusters number the value at which marginal gain of variance explained stops increasing (i.e., point on the plot that looks like an elbow, Figure 4.34). In this way, if another cluster is added, it does not give better modelling of data.
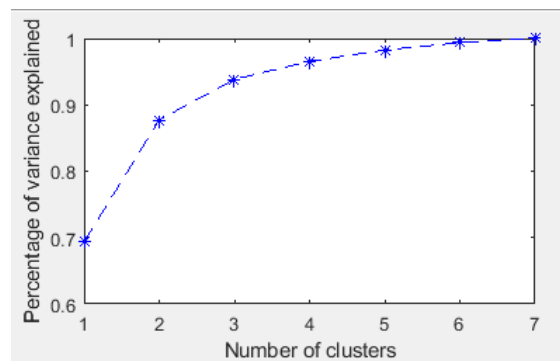
Figure 4.34: *Percentage variance explained as function of clusters number with the elbow shape.*

The implemented procedure also gives the possibility to normalize each pixel time series in [0,1] interval. In this way clustering is focused only on the shape of the single temporal evolution, neglecting the original intensity of image: this choice affects a lot the result.

Another significant analysis can be done by converting original images into the *Variation Images* (described in 4.2.2).

In the next section, analysis on liver microvascular dynamics with injection of Dobutamine and Nitroglycerin is discussed in detail.

4.2.4.2 Dobutamine and Nitroglycerin Clustering

In order to further investigate the effect of DB and NG on the microcirculation of the liver, clustering has been applied. Considering frames after drug injection, clustering is useful to identify different spatial areas which encompass pixels similar in their time evolution. Therefore, clustering could be a valuable tool to comprehend liver response to administration of different substances, allowing comparison between drugs.

Different methodologies have been used for analysing DB and NG. First, pixels time series of original images have been considered. As mentioned above, signals are analysed both non-normalized and normalized: dealing with original images, the former method enhances

intensity differences between signals, while the latter one favours signal shape (e.g.: a sinusoid of amplitude 0.1 matches perfectly a sinusoid of amplitude 100 in phase). In other words, clustering with non-normalized signals should group pixels depending on how much blood flow is contained within (i.e., videointensity value of the pixel), whereas using normalized signals the expected result should be based on the trend over time of the pixel, grouping together for example vessels which are emptying, without considering the amount of blood. Second, time series of pixels from *Variation Images* have been taken into account. In this case, clustering performed on non-normalized signals gather together pixels depending on how much their intensity change (i.e., how much is the percentage variation compared to baseline), instead with normalized signals clusters are constructed based on the trend of the variation with respect to baseline.

Dobutamine

1. Non-normalized intensity signal: using automatic cluster number selection, four distinct groupings are obtained. Big vessels are separated from background and microcirculation, which are blended because signals belonging to these areas are significantly smaller than the others). By manually increasing clusters number to have a more clear separation of different areas (e.g., 9), clusters shown in Figure 4.35 are obtained.

   In table 4.1, mean value of signals belonging to each cluster is available. It should be noted that these signals have very different video-intensity mean values: cluster 1 encloses background, cluster 6 comprehends areas around big vessels (i.e., the microvasculature) and the remaining clusters describe big high-flow vessels - mean value decreases moving from vessels center to vessels walls;

2. Normalized intensity signal: results shows that pixels from big vessels and hepatic cells close to them are grouped together, while in other clusters, except the one which encloses background pixels, signals coming from area above big vessels zone are assembled, as shown in Figure 4.36, which represents two over six clusters.

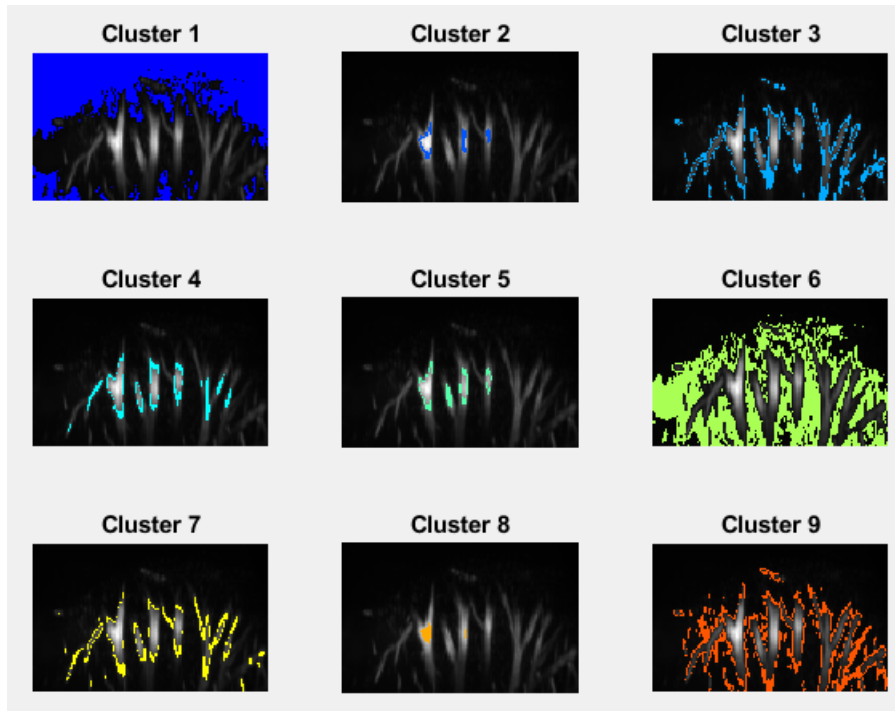*Figure 4.35: DB clusters without signal normalization.*

Table 4.1: Cluster number and mean intensity value of signals belonging to them (clusters of Figure 4.35);
maximum and minimum mean value are in bold.

Cluster	Mean Intensity
1	**0.0119**
2	0.5703
3	0.1124
4	0.2628
5	0.4006
6	0.0324
7	0.1763
8	**0.7426**
9	0.0651
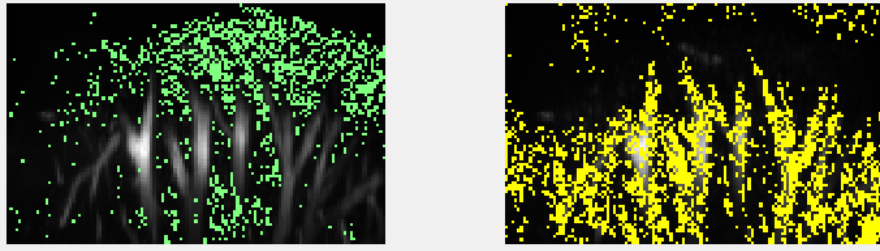
Figure 4.36: Clusters related to areas around main vessels (normalized signals).

3. Non-normalized relative variation signals: different trends have been identified, Figure 4.37 and Figure 4.38 show clustering result with k = 8.

   Cluster 3, 6, 7, 8 show a constant increase in time; by observing carefully the amount of relative variation, note that cluster 8 ends with a relative increase around 150% with respect to baseline, cluster 3 has an increase close to 100%, and 6 and 7 are very similar (under 50%). Cluster 2 is affected by background noise. Cluster 5 shows a constant decreasing trend (less than 25%). Cluster 4 is almost constant during first 200 seconds, then the signal decreases (lower than 10%) in the following 100 seconds and it grows up toward the baseline values in the remaining time. This last cluster probably identifies emptying of big vessels during extravasation caused by Dobutamine.
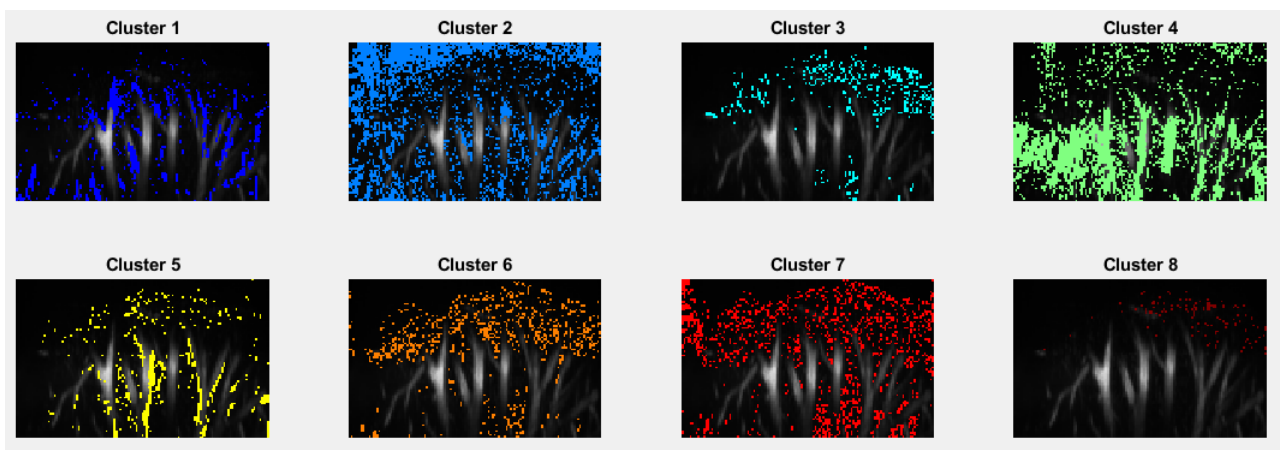
Figure 4.37: Clusters of DB (relative variation images, non-normalized signals).

79
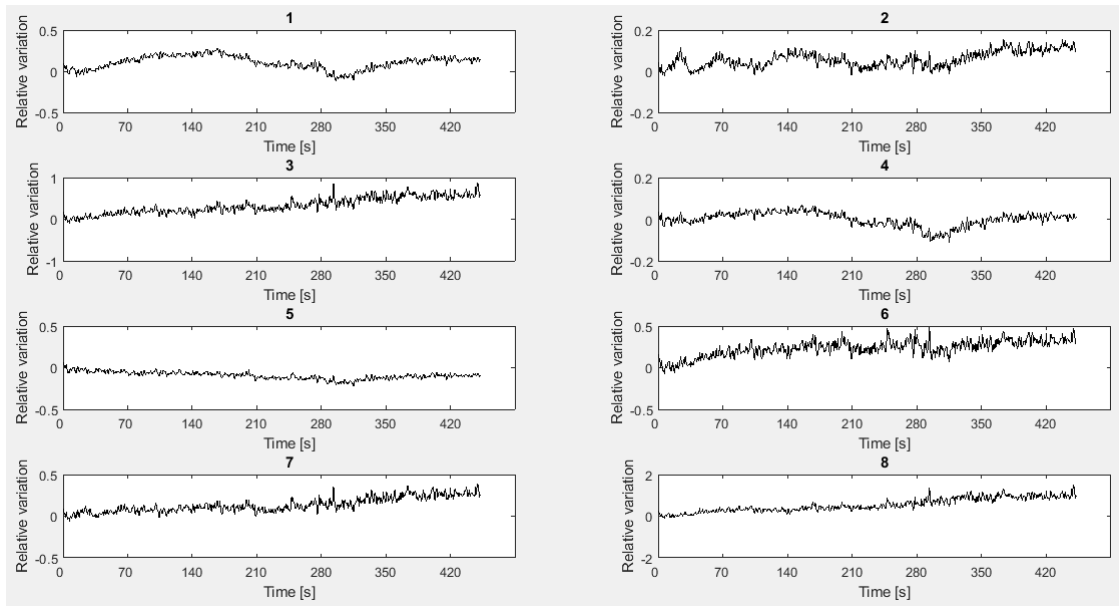
Figure 4.38: Mean videointensity values of clusters in Figure 4.37.

4. Normalized relative variation signals: Figure 4.39 and Figure 4.40 display the results. In this case with a very small number of clusters it is obtained a group containing most of the noise (cluster 1), a group which comprehends large vessels (cluster 4) and two group containing liver parenchyma (cluster 2, 3). By observing signals evolution in time, blood flow in big vessels increases immediately after the injection, then it decreases reaching a value lower than the baseline one and finally it increases again, stabilizing in the baseline. In the meanwhile, microvascular blood flow increases with different timings. These phenomena explain again extravasation caused by Dobutamine on hepatic haemodynamics: blood accumulates in big vessels and in a second moment it is released in microvasculature.
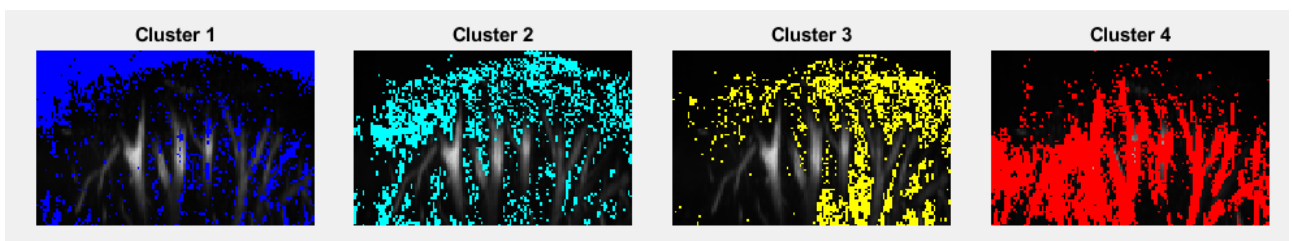
Figure 4.39: Clusters of DB dataset (relative variation images, normalized signals), considering frames after DB injection.
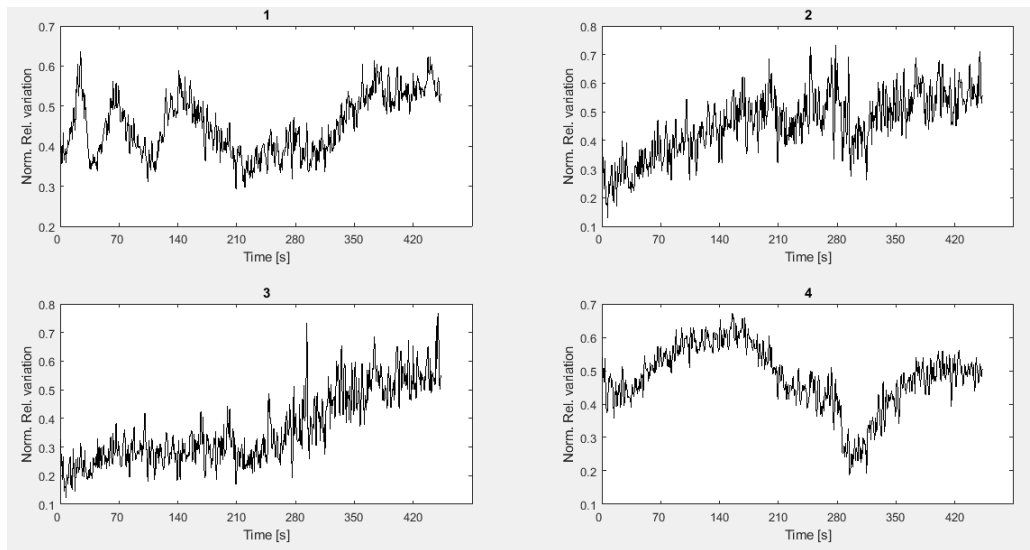
Figure 4.40: Mean Videointensity values of clusters in Figure 4.39.

Nitroglycerin

1. Non-normalized intensity signal: clusters group together almost the same pixels as DB clustering. An example with 6 clusters is represented in Figure 4.41.
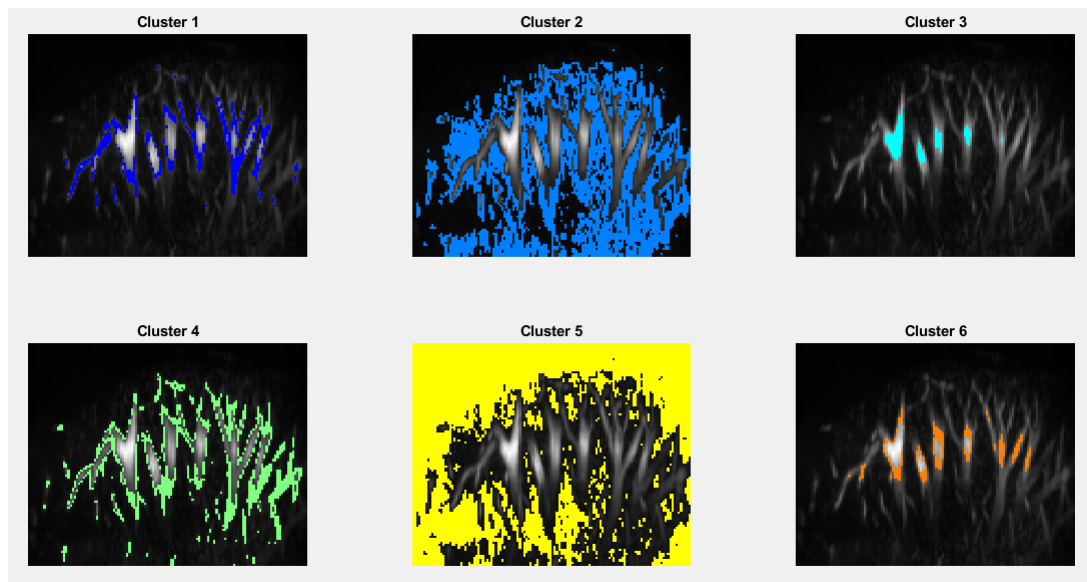
Figure 4.41: NG clusters obtained without signal normalization: clusters 1, 3, 6 are related to big vessels, while clusters 2 and 4 highlight parenchyma area.

2. Normalized intensity signal: the *elbow* method hints the use of 8 clusters (Figure 4.42). Most of the pixels grouped in cluster 3 are classifiable as noise, cluster 5, 7 and 8 gather pixels located around big vessels (also with some background noise) and cluster 1, 2, 4 and 6 collect a high number of signal coming from large vessels.
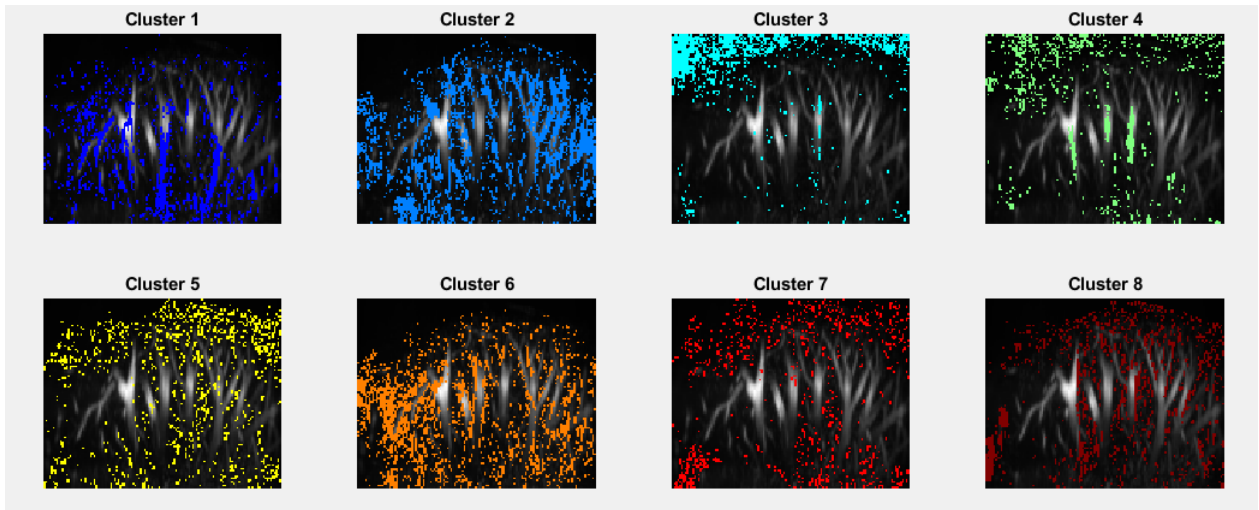
Figure 4.42: NG clusters obtained with signal normalization (frames after NG injection).

In this case, observation of time evolution of signals belonging to each cluster provides useful information (Figure 4.43). Cluster 1, 2, 5, 6 and 8 are characterized by an initial steady state, followed by a fast increase and then a variable decrease (very slow in cluster 1, rapid in cluster 8). Cluster 3 contains noise. Cluster 4 shows a slow constant increase in time. Cluster 7 seems to be affected by noise because does not show any particular behaviour.

3. Non-normalized relative variation signals: Figure 4.44 and Figure 4.45 display respectively clustering result and mean signal value for each cluster.
Cluster 2 contains part of big vessel and background: also increasing clusters number these two elements are not separated. All the elements belonging to the other clusters reveal an interesting trend: shortly after NG injection, all the signals raise rapidly, probably due to drug effect. Then, after a maximum value of relative variation (ranging from 10% to 200%), a drop occurs. It varies for each cluster and it is similar to an exponential decay with variable time constant: to group together pixel based on the time constants normalized signals are considered.
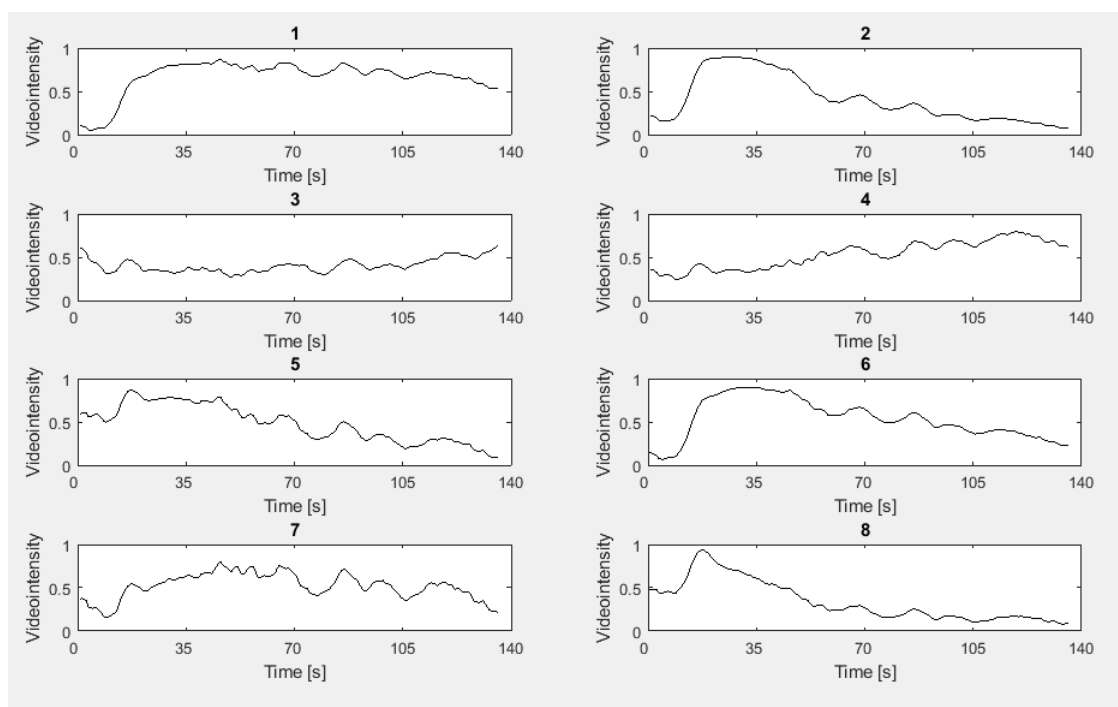
Figure 4.43: Mean videointensity values of pixels belonging to each cluster of Figure 4.42 (time 0 is the time of NG injection).
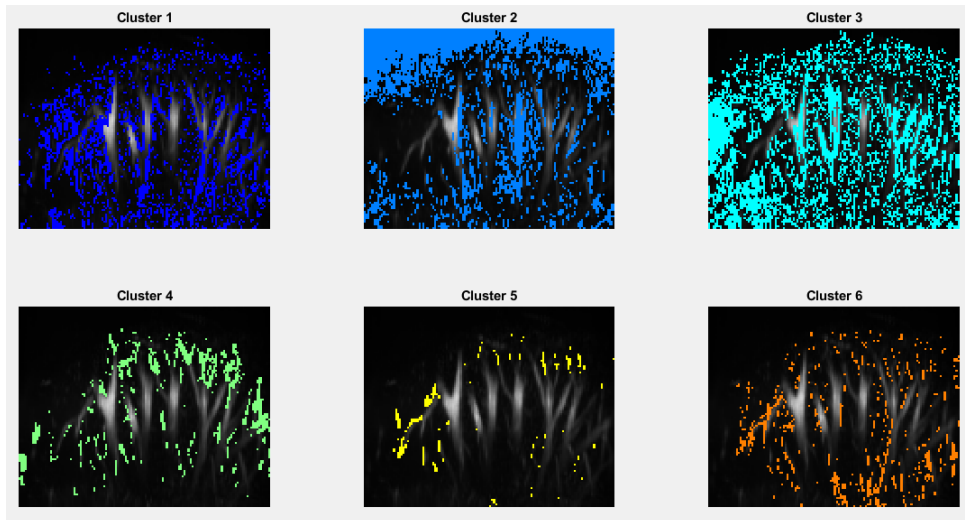
Figure 4.44: Clusters of NG dataset (relative variation images, non-normalized signals).
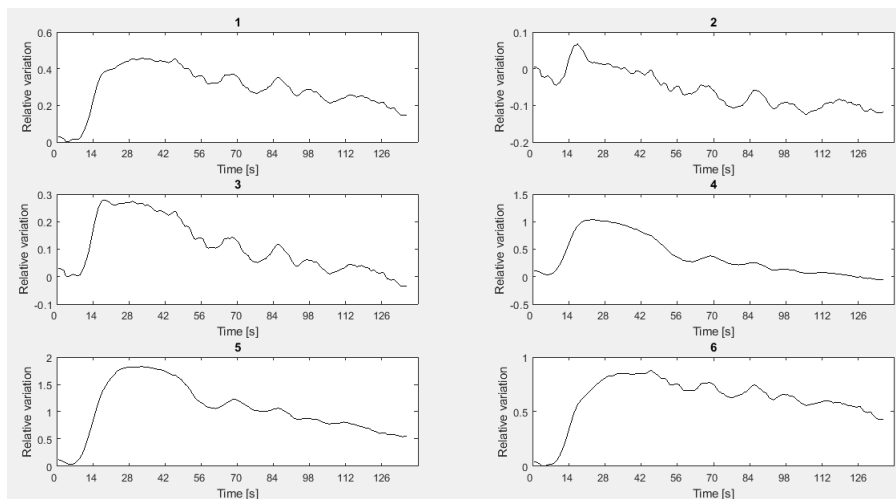
Figure 4.45: Mean Videointensity values of clusters in Figure 4.44.

4. Normalized relative variation signals: considering only positive relative variations (calculated through the T-mask method explained in 4.2.2.1), it is possible to subdivide signals characterized by different time decay after the peak caused by Nitroglycerin (Figure 4.46). Effects produced in different liver areas have different persistence in time, a map of how these areas are distributed is shown in Figure 4.47.
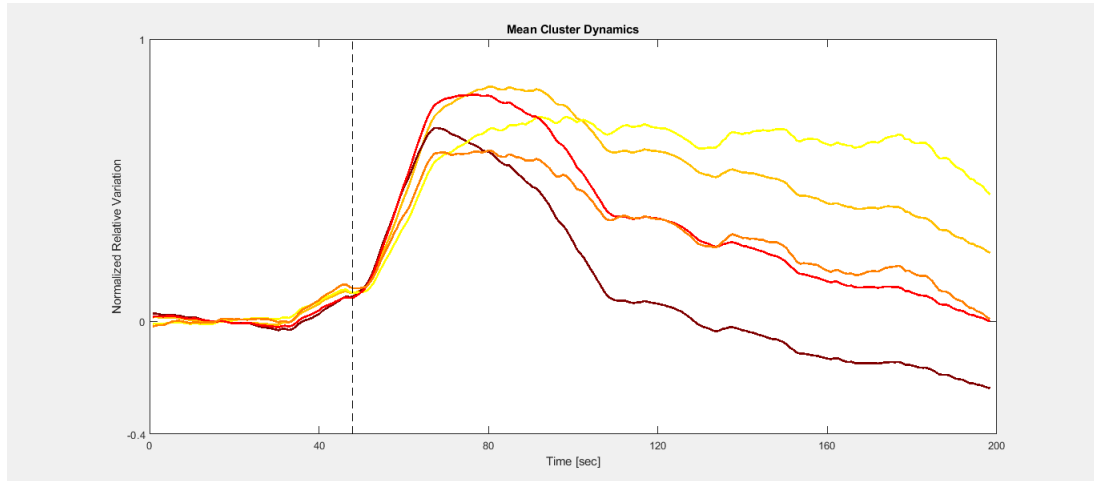
Figure 4.46: Mean trend of several liver areas with different decay.
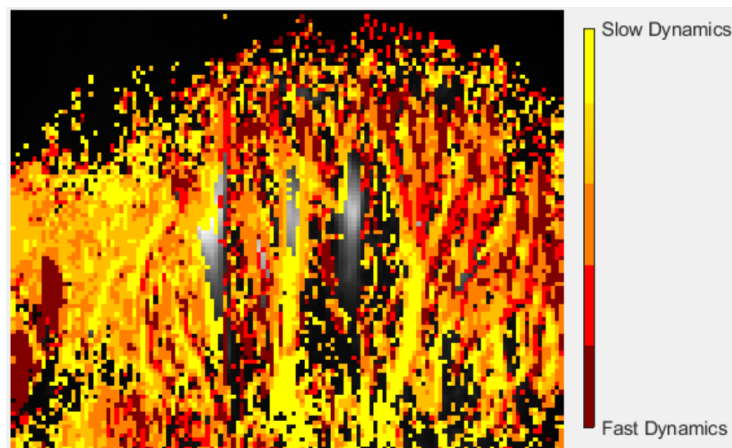
Figure 4.47: Persistence Map of liver: different colors highlight different time decay after NG injection.

Deciding which is the most suitable clustering methodology to be applied and interpreting the results are difficult tasks. This is due to the anatomical complexity of the organ: consequently, future validations are needed in order to investigate the correspondence between functional clusters and anatomical areas of the organ.

4.3 Intestine Analysis

Also intestine datasets have been analysed, even if partially.

By looking at images, both coronal and longitudinal, it has been noticed the presence of areas darker than other organ parts. Looking at the video (i.e., sequence of frames of a dataset) these areas move, giving the perception of different waves with variable frequency and propagation versus along the direction indicated in Figure 4.48.
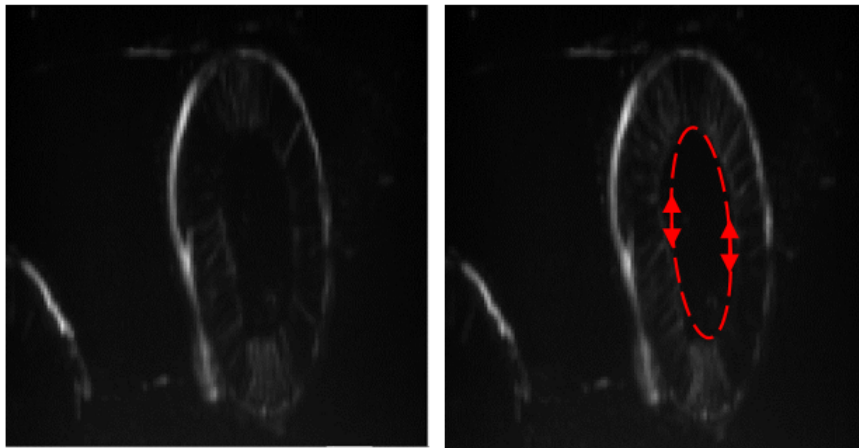
Figure 4.48: Intestine images: frame 237 (left) and frame 253 (right). In the right figure, the red ellipse indicates the direction of waves propagation.

In Figure 4.49, the temporal evolution of two randomly selected pixels belonging to villi is shown: both have a clear sinusoidal behaviour, characterized by two slightly different frequencies.

Comparable results are obtained with most of the pixels belonging to intestine. Each time series has a sinusoidal behaviour, with different main frequency.

It could be interesting quantifying sinewaves frequency to search for specific patterns or characteristic behaviours. Spectral analysis considers the problem of determining spectral content (i.e., the distribution of power in frequencies domain) of a time series from a finite set of measurements. In this case each pixel is a discrete temporal sequence and therefore it can be analysed through this technique.

With digital series, the Discrete Fourier Transform (DFT) allows signal decomposition into its different frequencies. As mentioned in 4.1, signals are considered equally spaced time series.
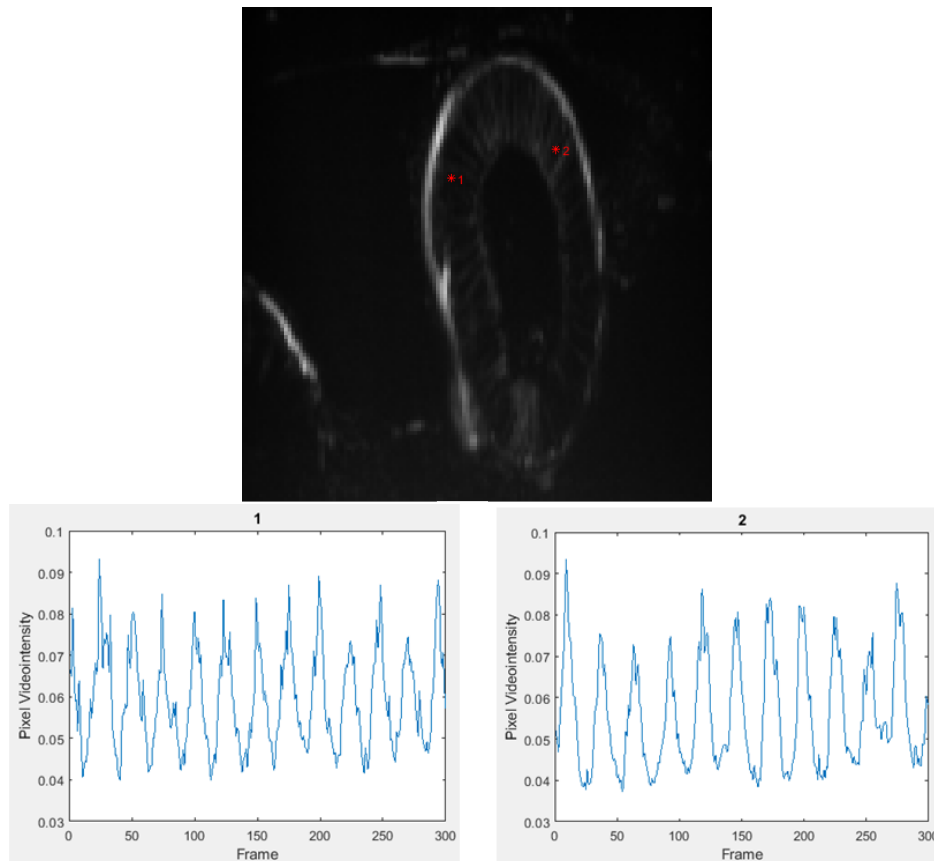
Figure 4.49: Time series of two intestine pixels (red stars in top figure).

Figure 4.50 shows the DFT of one signal of Figure 4.49 taken as example. The DFT is computed on Matlab through Fast Fourier Transform algorithm: the peak identifies the predominant frequency.
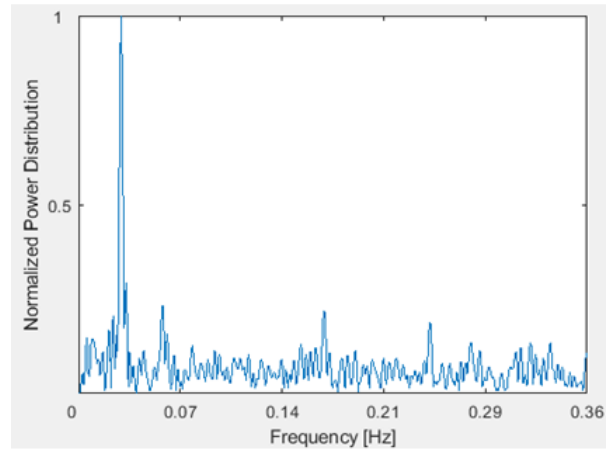
Figure 4.50: Example of Frequency Spectrum of a pixel time series.

By repeating this procedure for each image pixel, the result is a two-dimensional map representing the predominant frequency for each time series. Setting properly image contrast, for a single dataset is obtained a map such Figure 4.51.
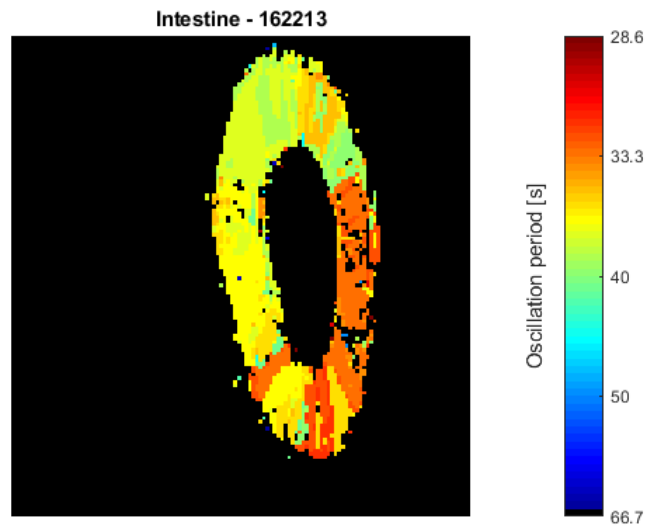
Figure 4.51: Frequency Map for dataset 162213, different colors are associated to different oscillation periods (i.e., different signal main frequency). All frequencies under 0.015 Hz are saturated to black, while those over 0.04 Hz to red (these values are chosen by arbitrary observing histogram of frequency map).

Results of the application of frequency analysis on several intestine datasets are listed in Table 4.2, where it is reported maximum, minimum and mean frequency of pixels belonging to intestine.

Table 4.2: Frequency range and mean frequency for intestine.

Dataset	Minimum Freq. [Hz]	Maximum Freq. [Hz]	Mean Freq. [Hz]
165342	0.015	0.04	0.0292
163144	0.015	0.04	0.0278
162213	0.015	0.04	0.029
171314	0.01	0.05	0.0325
174212	0.01	0.05	0.0312

In order to asses the constancy of the oscillatory period over time, Wavelet Transform (WT) has been applied to image pixels.

WT is a specific technique based on signal decomposition into blocks defined in time and frequency. Through WT, it is possible to detect which frequencies characterise the signal during its evolution in time: this is the main advantage with respect Fourier Transform, which gives information about frequency contents, but without time localization.

For intestine dataset, main frequency of villi signals remain constant, as shown in Figure 4.52, in which is displayed the scalogram (i.e., time-frequency representation) of a pixel and its original trend over time.

WT has been applied also to dataset in which glucose is injected (injection at frame 300). The results are the same: main frequency of pixels does not change, while it is visible a small modification of signal amplitude (Figure 4.53). This fact is probably due to a modulation of microvascular resistance during the absorption of the nutrient.

Figure 4.52: Time-Frequency representation of a pixel signal (top) and its trend along frames (bottom) - no drug injection.
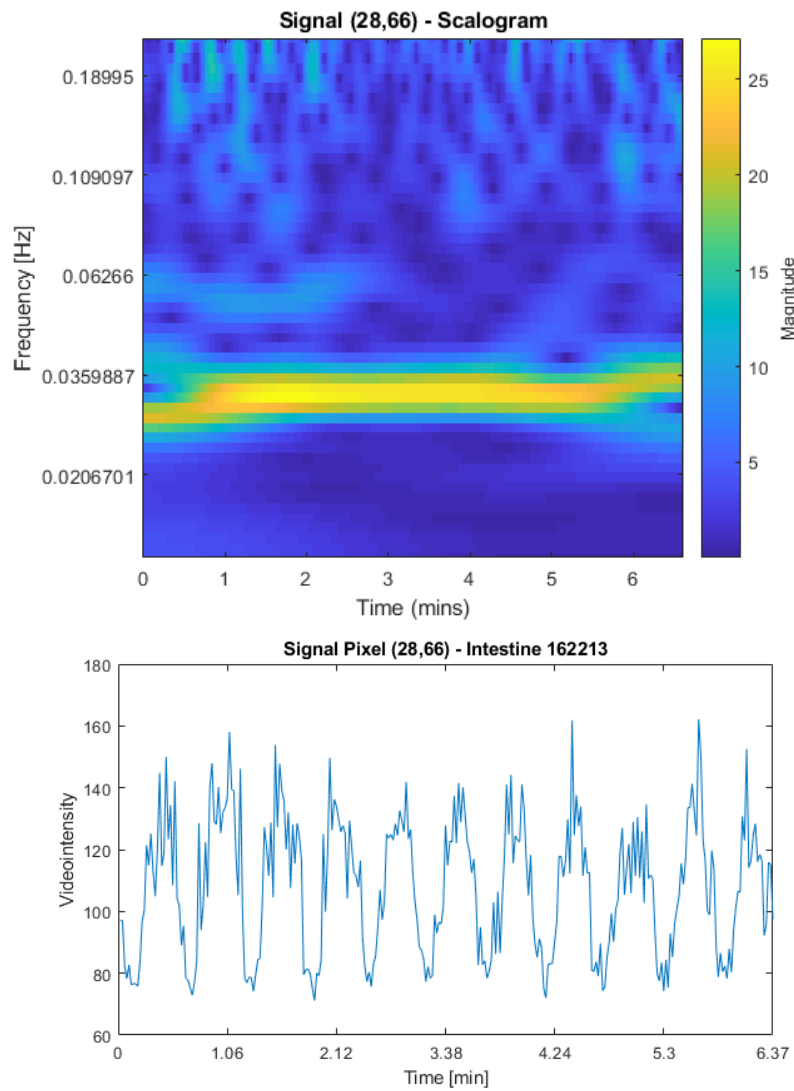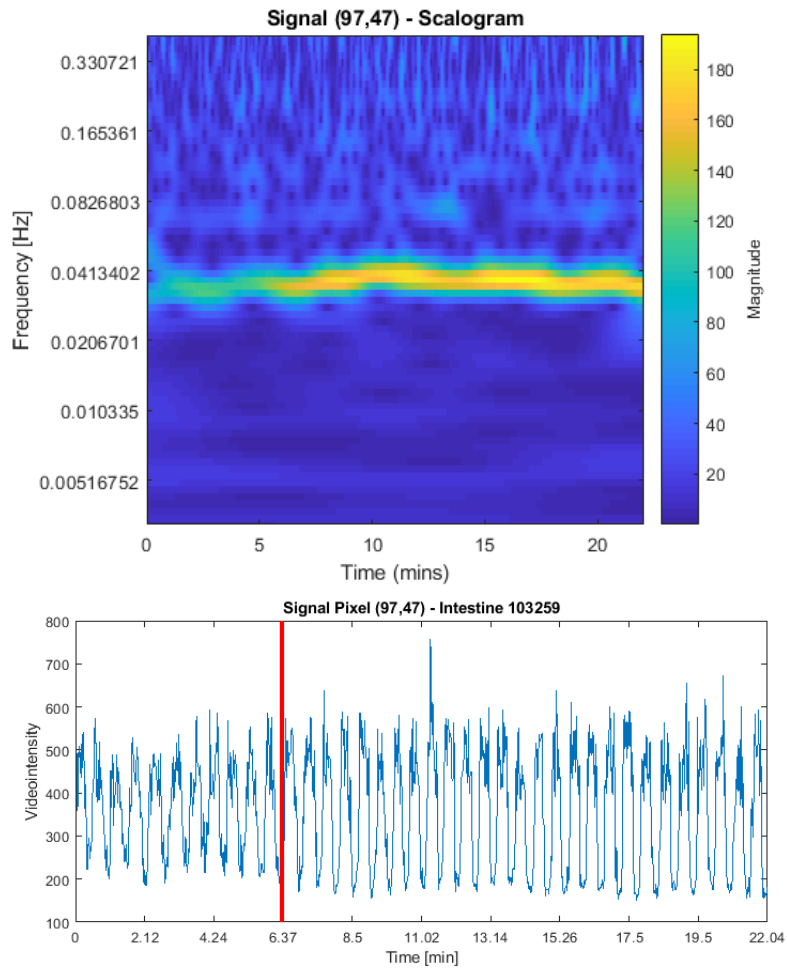
Figure 4.53: Time-Frequency representation of a pixel signal (top) and its trend along frames (bottom) - the red line indicates the time of glucose injection.

Chapter 5

Conclusions

Microvasculature has a well-assessed pivotal role in several pathophysiological processes. Nevertheless, only few existing techniques allow functional evaluation of microvasculature *in vivo* and none of them is suitable for a clinical environment.

Since functional ultrasound imaging represents an innovative technique, a considerable effort has been spent by the authors, developing the first image and signal processing approaches to investigate these recordings. As a result of the current thesis work, a graphic user interface for the investigation of hepatic microvascular dynamics has been developed in Matlab environment.

The tool set a first method for fUS liver images examination and it aims to be an efficient instrument dedicated to people, such physicians, which do not have specific knowledge in image analysis. The GUI enables an easy visualization of image sequences and it gives the possibility to perform simple operations on acquired images. Tool functionalities are grouped in specific boxes, each box is provided with *Information button* which gives to the user details on button operation, in order to provide a user-friendly environment.

Images derived from functional ultrasound of the liver, as seen in previous chapters, need an accurate pre-processing: noise attenuation through filters, deletion of frames corrupted during acquisition by drug administration and other external interferences, elimination of disturbing elements as bubbles, registration (mandatory for analysing pixels as temporal series). Once datasets have been pre-processed, it is possible to extract indexes of interest in a semi-automatic way (i.e., for some operations the user has to manually enter specific data).

Nowadays, physicians do not have a valuable device to evaluate microvascular performances, for example during and after transplantation procedures: they base their decisions simply

observing organ colouration and touching its surface. The final aim of the software is to provide the possibility to extrapolate useful parameters with null or minimum user interaction. A key element to be considered in future developments is the reliability of real-time analysis. fUS can be an extremely precious tool for basic research, too. First, it allows investigating *in vivo* organ microcirculation as no other technique can do: therefore, fUS should be exploited to achieve a more detailed knowledge of the complex interactions occurring in microvasculature both in physiological and pathological states. Second, it is useful to determine local effects produced at microvascular level by different drugs (e.g., Dobutamine and Nitroglycerine). Understanding how each substance acts is fundamental to provide physicians with useful information during decision-making processes, leading to better patient care.

Finally, fUS has a high scalable penetration depth (up to 20 cm) which can be used to perform percutaneous measurements. In this way, it is possible to observe microcirculation not only intra-operatively, for example allowing monitoring of parameters in post-operative evaluations. This aspect has not been treated in the current work because the procedure is still under development in the Esposti Lab., nonetheless it represents an interesting future development for which it will be required a specific pre-processing procedure.

Some clinical trials with fUS imaging system are already in progress at the Esposti Lab. with several partners:

- Liver transplantation support: as mentioned above, currently there are no diagnostic methods for physicians to assess microvascular dynamics during and after surgical intervention. The trial includes analysis before donor's liver resection, during organ implantation and in first five postoperative days;

- Detection of local microvascular inhomogeneities and abnormalities in sepsis: due to the large incidence of sepsis and the assessed crucial role of microcirculation in this pathology, investigation of its functionalities during patient hospitalization is becoming increasingly important;

- Non-invasive pre-surgical assessment of microvascular invasion in hepatocellular carcinoma (HCC): development of a system for testing of drugs for HCC.

Furthermore, fUS imaging can be used also for investigating other organs, making this technique ductile. Possible clinical applications concern kidney (transplantation support, chronic and acute diseases evaluation), gastrointestinal tract (malabsorption, inflammatory bowel diseases, Lynch syndrome), reproductive system (erectile dysfunctions, hypofertility).

In particular, in addition to liver analysis to which most of the time was dedicated, current work also deals with intestine datasets. Frequency analysis of villi shows the presence of spatial areas which are characterized by a specific frequency; furthermore, phase delays in each area result in a moving spatial wave along the structure. As future development, analysis of drug effect on intestine is recommended, followed by a model which characterized villi dynamics in frequency domain with the aim also of understanding which mechanisms regulate pathophysiology of this organ.

Bibliography

[1]   E Okabe, K Todoki, and H Ito. "Microcirculation: function and regulation in microvasculature". In: *Dynamic Aspects of Dental Pulp*. Springer, 1990, pp. 151–166.

[2]   Christopher G Ellis, Justin Jagger, and Michael Sharpe. "The microcirculation as a functional system". In: *Critical Care* 9.4 (2005), S3.

[3]   Daniel De Backer et al. "Microcirculatory alterations: potential mechanisms and implications for therapy". In: *Annals of intensive care* 1.1 (2011), p. 27.

[4]   Daniel De Backer et al. "Pathophysiology of microcirculatory dysfunction and the pathogenesis of septic shock". In: *Virulence* 5.1 (2014), pp. 73–79.

[5]   E Christiaan Boerma et al. "Quantifying bedside-derived imaging of microcirculatory abnormalities in septic patients: a prospective validation study". In: *Critical Care* 9.6 (2005), R601.

[6]   Colin Verdant and Daniel De Backer. "How monitoring of the microcirculation may help us at the bedside". In: *Current opinion in critical care* 11.3 (2005), pp. 240–244.

[7]   Asha Tyagi et al. "The microcirculation in sepsis". In: *Indian journal of anaesthesia* 53.3 (2009), p. 281.

[8]   Walter F Boron and Emile L Boulpaep. *Medical Physiology, 2e Updated Edition E-Book: with STUDENT CONSULT Online Access*. Elsevier Health Sciences, 2012.

[9]   Stephen Trzeciak et al. "Early microcirculatory perfusion derangements in patients with severe sepsis and septic shock: relationship to hemodynamics, oxygen transport, and survival". In: *Annals of emergency medicine* 49.1 (2007), pp. 88–98.

[10] Andrew M Smith, Michael C Mancini, and Shuming Nie. "Bioimaging: second window for in vivo imaging". In: *Nature nanotechnology* 4.11 (2009), pp. 710–711.

[11]   Gero Puhl et al. "Noninvasive in vivo analysis of the human hepatic microcircula-
       tion using orthogonal polorization spectral imaging". In: *Transplantation* 75.6 (2003),
       pp. 756–761.

[12]   Warren Groner et al. "Orthogonal polarization spectral imaging: a new method for
       study of the microcirculation". In: *Nature medicine* 5.10 (1999), pp. 1209–1212.

[13]   PT Goedhart et al. "Sidestream Dark Field (SDF) imaging: a novel stroboscopic LED
       ring-based imaging modality for clinical assessment of the microcirculation." In: *Optics
       express* 15.23 (2007), pp. 15101–15114.

[14]   C Ince. "Sidestream dark field imaging: an improved technique to observe sublingual
       microcirculation". In: *Critical care* 9.1 (2005), P72.

[15]   Emilie Mace et al. "Functional ultrasound imaging of the brain: theory and basic prin-
       ciples". In: *IEEE transactions on ultrasonics, ferroelectrics, and frequency control* 60.3
       (2013), pp. 492–506.

[16]   Jeremy Bercoff et al. "Ultrafast compound Doppler imaging: Providing full blood flow
       characterization". In: *IEEE transactions on ultrasonics, ferroelectrics, and frequency
       control* 58.1 (2011).

[17]   Andrew Webb. *Introduction to biomedical imaging.* Wiley-Interscience, 2003.

[18]   Atam P Dhawan. *Medical image analysis.* Vol. 31. John Wiley & Sons, 2011.

[19]   Giuseppe Coppini, Stefano Diciotti, and Guido Valli. *Bioimmagini.* Pàtron, 2012.

[20]   GR Bergfeld and T Forrester. "Release of ATP from human erythrocytes in response
       to a brief period of hypoxia and hypercapnia". In: *Cardiovascular research* 26.1 (1992),
       pp. 40–47.

[21]   Brigitte Vollmar and Michael D Menger. "The hepatic microcirculation: mechanistic
       contributions and therapeutic targets in liver injury and repair". In: *Physiological re-
       views* 89.4 (2009), pp. 1269–1339.

[22]   Christian Eipel, Kerstin Abshagen, and Brigitte Vollmar. "Regulation of hepatic blood
       flow: the hepatic arterial buffer response revisited". In: *World journal of gastroenterol-
       ogy: WJG* 16.48 (2010), p. 6046.

[23]   Shin Hwang. "Microcirculation of the Liver". In: *Venous Embolization of the Liver.*
       Springer, 2011, pp. 9–13.

[24] Simon C Satchell and Filip Braet. "Glomerular endothelial cell fenestrations: an integral component of the glomerular filtration barrier". In: *American Journal of Physiology-Renal Physiology* 296.5 (2009), F947–F956.

[25] H Reynaert et al. "Hepatic stellate cells: role in microcirculation and pathophysiology of portal hypertension". In: *Gut* 50.4 (2002), pp. 571–581.

[26] Robert F Furchgott. "The discovery of endothelium-derived relaxing factor and its importance in the identification of nitric oxide". In: *Jama* 276.14 (1996), pp. 1186–1188.

[27] Makoto Suematsu et al. "Carbon monoxide: an endogenous modulator of sinusoidal tone in the perfused rat liver." In: *Journal of Clinical Investigation* 96.5 (1995), p. 2431.

[28] Baimeng Zhang et al. "NO-mediated vasodilation in the rat liver: role of hepatocytes and liver endothelial cells". In: *Journal of hepatology* 26.6 (1997), pp. 1348–1355.

[29] Alan BR Thomson and Eldon Shaffer. *Modern Concepts in Gastroenterology.* Springer Science & Business Media, 2012.

[30] Stefan Langer et al. "Orthogonal polarization spectral imaging as a tool for the assessment of hepatic microcirculation: a validation study". In: *Transplantation* 71.9 (2001), pp. 1249–1256.

[31] Gero Puhl et al. "Initial hepatic microcirculation correlates with early graft function in human orthotopic liver transplantation". In: *Liver transplantation* 11.5 (2005), pp. 555–563.

[32] Curt M Treu et al. "Sidestream dark field imaging: the evolution of real-time visualization of cutaneous microcirculation and its potential application in dermatology". In: *Archives of dermatological research* 303.2 (2011), pp. 69–78.

[33] Gabriele Reich. "Near-infrared spectroscopy and imaging: basic principles and pharmaceutical applications". In: *Advanced drug delivery reviews* 57.8 (2005), pp. 1109–1143.

[34] Marketa Stanclova, Zdenek Kokstein, and Vladimir Cerny. "Orthogonal polarization spectral (OPS)/sidestream dark field (SDF) imaging: a new method for the observation of the microcirculation in pediatrics". In: *Appl Cardiopulm Pathophysiol* 16 (2012), pp. 249–253.

[35] Vladimir Cerny. "Sublingual microcirculation". In: *Appl Cardiopulm Pathophysiol* 16 (2012), pp. 229–48.

[36] Daniel De Backer et al. "How to evaluate the microcirculation: report of a round table conference". In: *Critical care* 11.5 (2007), R101.

[37] Sumeyra U Demir et al. "An automated method for analysis of microcirculation videos for accurate assessment of tissue perfusion". In: *BMC medical imaging* 12.1 (2012), p. 37.

[38] T Klyscz et al. "Cap image–a new kind of computer-assisted video image analysis system for dynamic capillary microscopy". In: *Biomedizinische Technik. Biomedical engineering* 42.6 (1997), pp. 168–175.

[39] Daniel De Backer et al. "Microvascular blood flow is altered in patients with sepsis". In: *American journal of respiratory and critical care medicine* 166.1 (2002), pp. 98–104.

[40] Yasser Sakr et al. "Persistent microcirculatory alterations are associated with organ failure and death in patients with septic shock". In: *Critical care medicine* 32.9 (2004), pp. 1825–1831.

[41] D De Backer et al. "Microcirculatory alterations are an independent outcome predictor in patients with severe sepsis and septic shock". In: *CRITICAL CARE MEDICINE*. Vol. 31. 12. LIPPINCOTT WILLIAMS & WILKINS 530 WALNUT ST, PHILADELPHIA, PA 19106-3621 USA. 2003, A117–A117.

[42] Gabriel Montaldo et al. "Coherent plane-wave compounding for very high frame rate ultrasonography and transient elastography". In: *IEEE transactions on ultrasonics, ferroelectrics, and frequency control* 56.3 (2009), pp. 489–506.

[43] Steinar Bjaerum, Hans Torp, and Kjell Kristoffersen. "Clutter filters adapted to tissue motion in ultrasound color flow imaging". In: *IEEE transactions on ultrasonics, ferroelectrics, and frequency control* 49.6 (2002), pp. 693–704.

[44] Steven L Meyer et al. "Influence of dobutamine on hemodynamics and coronary blood flow in patients with and without coronary artery disease". In: *The American journal of cardiology* 38.1 (1976), pp. 103–108.

[45] Fausto J Pinto et al. "Nitroglycerin-induced coronary vasodilation in cardiac transplant recipients. Evaluation with in vivo intracoronary ultrasound." In: *Circulation* 85.1 (1992), pp. 69–77.

[46]   Norman Brachfeld et al. "Action of nitroglycerin on the coronary circulation in normal and in mild cardiac subjects". In: *Circulation* 19.5 (1959), pp. 697–704.

[47]   Trupti M Kodinariya and Prashant R Makwana. "Review on determining number of Cluster in K-Means Clustering". In: *International Journal* 1.6 (2013), pp. 90–95.